

# **Borehole seismic monitoring of CO<sub>2</sub> storage within a saline aquifer at Ketzin, Germany**

vorgelegt von  
Dipl.-Ing. Geophysik  
Julia Götz  
aus Kronach

von der Fakultät VI - Planen / Bauen / Umwelt  
der Technischen Universität Berlin  
zur Erlangung des akademischen Grades

Doktor der Ingenieurwissenschaften  
- Dr.-Ing. -

genehmigte Dissertation

Promotionsausschuss:

Vorsitzender: Prof. Dr. W. Dominik  
Gutachterin: Prof. Dr. C. M. Krawczyk  
Gutachter: Prof. Dr. Ir. R. J. Arts  
Gutachter: Dr. St. Lüth

Tag der wissenschaftlichen Aussprache: 13. Dezember 2013

Berlin 2014  
D 83



---

## Abstract

This thesis is about borehole seismic monitoring of CO<sub>2</sub> storage within a saline aquifer at Ketzin, Germany. CO<sub>2</sub> storage is part of the process 'Carbon dioxide Capture and Storage (CCS)'. As a greenhouse gas, CO<sub>2</sub> contributes to the global warming, therefore efforts are made to slow down the increase of CO<sub>2</sub> concentration in the atmosphere. CCS is considered because "fossil fuels are the dominant form of energy utilised in the world (86 %) and account for 75 % of current anthropogenic CO<sub>2</sub> emissions" (IPCC (2005)). Deep saline aquifer storage is "the most promising and relevant CO<sub>2</sub> sequestration option for Europe" (Juhlin et al. (2007)). Saline aquifers are broadly distributed "and their storage capacity exceeds that of depleted oil and gas fields" (Juhlin et al. (2007)). "Techniques developed for the exploration of oil and gas reservoirs, natural gas storage sites and liquid waste disposal sites are suitable for characterising and monitoring geological storage sites for CO<sub>2</sub>" (IPCC (2005)). Although these methods include many of the tools "needed to predict both short-term and long-term performance of CO<sub>2</sub> storage, more experience is needed to establish confidence in their effectiveness in predicting long-term performance when adapted for CO<sub>2</sub> storage" (IPCC (2005)).

Operated by the German Research Centre for Geosciences (GFZ), the in situ laboratory for saline aquifer CO<sub>2</sub> storage near the town Ketzin (35 km west of Berlin) is the first European onshore storage pilot facility. It advances "the understanding of the science and practical processes involved in underground storage" (Förster et al. (2006)). Within 5 years of operation, between June 2008 and April 2013, 65 kt of supercritical, food-grade CO<sub>2</sub> have been injected.

As part of a comprehensive geophysical monitoring program at Ketzin, the research in this thesis focuses on the crosshole seismic, zero-offset and offset VSP measurements. While the baseline surveys provide the structural geometry and characterisation of the site, the repeat surveys aim at the observation of CO<sub>2</sub> propagation in the reservoir. Based on geological information and well cores, the reservoir is described as thin and heterogeneous at the research site (Yang (2012)). "The thickness of the reservoir is generally less than 20 m", what is "below the resolution of conventional surface seismic data" (Yang (2012)). Borehole seismic methods are expected to have a higher resolution than surface seismic and are therefore tested at the Ketzin site. Two questions should be answered: With these methods, is it possible (1) to map the CO<sub>2</sub> in the reservoir layer (2) to derive geometrical and petrophysical parameters describing the migration of CO<sub>2</sub> in a water saturated sandstone reservoir?

The crosshole seismic measurement was designed to follow the migration of CO<sub>2</sub> at small scale during the injection. "As CO<sub>2</sub> replaces saline water in saturated reservoir sandstones a seismic velocity reduction may occur. This velocity change can potentially be used to monitor CO<sub>2</sub> in sandstone aquifers using seismic tomography" (Zhang et al. (2012)). Based on a velocity model derived from the measured data, travel time tomography is tested on synthetic data having the same geometry as the real data. The shape of the CO<sub>2</sub> plume and an estimate of the velocity reduction in the reservoir is derived for different scenarios of CO<sub>2</sub> distribution.

The main objective of the zero-offset and offset VSP surveys was to generate high-resolution seismic images in the vicinity of the borehole. As CO<sub>2</sub> replaces saline water in saturated sandstones, the impedance contrast between the gas filled sandstone and the caprock is increased, what leads to stronger reflections from top of the reservoir. This increased reflectivity can be used to image the spreading of CO<sub>2</sub> in the reservoir. While the zero-offset VSP focuses on normal incidence reflectivity near the observation well, offset VSP has the potential to generate a lateral image of the reservoir at the injection

---

site. A near-well corridor stack of the zero-offset VSP is compared to 3D surface seismic data. Based on the CO<sub>2</sub> induced amplitude changes of the repeat measurement, the thickness of the CO<sub>2</sub> plume is derived by a wedge modelling study and the reduction of P-wave velocity is calculated with band limited impedance inversion. The offset VSP measurements are imaged by Kirchhoff and Fresnel migration. The application of two migration algorithms can help to differentiate between method-related and true time-lapse effects when interpreting the seismic images.

It is shown that borehole seismic methods can image the distribution of CO<sub>2</sub> in the reservoir and contribute to the quantification of geometrical and petrophysical parameters of the plume. In the framework of monitoring CO<sub>2</sub> injection, borehole seismic methods should be used as an add-on to surface seismic, in case more detailed information is needed about the structure in the vicinity of boreholes. In addition, borehole seismic monitoring can be applied to the observation of layers above the reservoir, for the detection of leakage paths or the inspection of well integrity.

## **Zusammenfassung**

Die vorliegende Dissertation befasst sich mit der Überwachung von CO<sub>2</sub>-Speicherung in einem salinen Aquifer bei Ketzin, Deutschland, mittels bohrlochseismischer Methoden. CO<sub>2</sub>-Speicherung ist Teil des Prozesses 'CO<sub>2</sub>-Abscheidung, Transport und Speicherung' (englisch CCS - Carbon Dioxide Capture and Storage). Als Treibhausgas trägt CO<sub>2</sub> zur globalen Erwärmung bei, weshalb es notwendig ist, den Anstieg der CO<sub>2</sub>-Konzentration in der Atmosphäre zu verlangsamen. CCS wird erforscht, da fossile Energieträger weltweit am häufigsten genutzt werden (86 %) und 75 % der derzeitigen, anthropogenen CO<sub>2</sub>-Emissionen ausmachen (IPCC (2005)). Die Speicherung in tiefen, salzwasserführenden Aquiferen ist für Europa die vielversprechendste Speichermöglichkeit. Saline Aquifere sind weit verbreitet und ihre Speicherkapazität liegt über der von leergeförderten Öl- oder Gasfeldern (Juhlin et al. (2007)). Methoden, die für die Untersuchung von Öl- und Gasreservoirs, natürlichen Speicherstätten sowie zur Überwachung flüssiger Abfälle entwickelt wurden, können auch zur Charakterisierung und Überwachung geologischer CO<sub>2</sub>-Speicher eingesetzt werden (IPCC (2005)). Obwohl diese Methoden viele der Hilfsmittel bereitstellen, um das Verhalten eines CO<sub>2</sub>-Speichers zu beschreiben, muss noch gezeigt werden, dass sie auch auf die langen Zeiträume einer CO<sub>2</sub>-Speicherung anwendbar sind (IPCC (2005)).

In der Nähe der Stadt Ketzin (35 km westlich von Berlin), betreibt das Deutsche GeoForschungsZentrum (GFZ), das erste Europäische Feldlabor zur Speicherung von CO<sub>2</sub> in salinen Aquiferen. In diesem Pilotprojekt wird das wissenschaftliche und technische Verständnis der geologischen Speicherung von CO<sub>2</sub> weiterentwickelt (Förster et al. (2006)). Innerhalb der letzten 5 Jahre, zwischen Juni 2008 und April 2013, wurden 65 kt superkritisches, lebensmittelreines CO<sub>2</sub> verpresst.

Im Rahmen verschiedenster, geophysikalischer Überwachungsmethoden, konzentrieren sich die Untersuchungen in der vorliegenden Dissertation auf Crosshole Seismik, zero-offset und offset VSP Messungen. Während Referenzmessungen (Nullmessungen) Aussagen über die Strukturen und Eigenschaften des Standortes zulassen, ist die Aufgabe der Wiederholungsmessung die Beobachtung der Ausbreitung von CO<sub>2</sub> im Reservoir. Das Reservoir in Ketzin wird, basierend auf geologischen Informationen und untersuchten Bohrkernen, als dünn und heterogen beschrieben (Yang (2012)). Die Mächtigkeit des Reservoirs ist in der Regel geringer als 20 m, was unterhalb der Auflösung von oberflächenseismischen Methoden liegt (Yang (2012)). Da bohrlochseismische Methoden eine höhere Auflösung als oberflächenseismische Methoden haben, werden diese in Ketzin

---

getestet. Es sollen zwei Fragen beantwortet werden: Ist es mit diesen Methoden möglich (1) das CO<sub>2</sub> im Reservoir zu kartieren, (2) geometrische und petrophysikalische Parameter abzuleiten, die die Ausbreitung von CO<sub>2</sub> in wassergesättigten Reservoirsandsteinen beschreiben?

Die Crosshole Seismik wurde ausgelegt, um die Ausbreitung des CO<sub>2</sub> in kleinem Maßstab während der Verpressung zu beobachten. Wird salzhaltiges Wasser in einem gesättigten Sandsteinreservoir durch CO<sub>2</sub> verdrängt, kann dessen seismische Geschwindigkeit verringert werden. Diese Geschwindigkeitsänderung, kann dazu genutzt werden, das CO<sub>2</sub> in Sandsteinaquiferen mittels Laufzeitomographie zu überwachen (Zhang et al. (2012)). Aus gemessenen Daten wurde ein Geschwindigkeitsmodell errechnet. Dieses Modell dient als Grundlage für die Laufzeitomographie synthetischer Daten, basierend auf der selben Geometrie wie die gemessenen Daten. Für zwei verschiedene Ausbreitungsszenarios wurde die Form der CO<sub>2</sub>-Fahne und eine Abschätzung der Geschwindigkeiterniedrigung errechnet.

Mit den zero-offset und offset VSP Messungen wird ein hochaufgelöstes Abbild des Untergrundes im näheren Umfeld der Bohrung erzeugt. Wird das Salzwasser in gesättigten Sandsteinreservoirs durch CO<sub>2</sub> verdrängt, führt das zu einer Verstärkung des Impedanzkontrastes zwischen dem gasgefüllten Reservoir und der Deckschicht. Dies führt wiederum zu einer stärkeren Reflektion an der Oberkante des Reservoirs. Diese verstärkte Reflektion kann genutzt werden, um die Ausbreitung von CO<sub>2</sub> im Reservoir abzubilden. Der Schwerpunkt der zero-offset VSP liegt in der Aufzeichnung der Reflektivität bei senkrechtem Einfall unmittelbar an der Bohrung, mit der offset VSP können flächige Abbilder des Reservoirs am Speicherstandort erzeugt werden. Ein 'corridor stack' der zero-offset VSP aus der unmittelbaren Umgebung der Bohrung wird mit 3D-oberflächenseismischen Daten verglichen. Aus der CO<sub>2</sub> bedingten Verstärkung der Amplituden in der Wiederholungsmessung, wird die Mächtigkeit der CO<sub>2</sub>-Fahne in einer Modellstudie ('wedge model') abgeleitet, die Verringerung der P-Wellen Geschwindigkeit wird durch eine Inversionsrechnung bestimmt ('band limited impedance inversion'). Die offset VSP Messungen werden mittels Kirchhoff und Fresnel Migration abgebildet. Die Verwendung unterschiedlicher Migrationsalgorithmen kann dazu beitragen, bei der Interpretation seismischer Abbildungen, methodische von CO<sub>2</sub> bedingten Effekten zu unterscheiden.

Es kann gezeigt werden, dass bohrlochseismische Methoden die Ausbreitung von CO<sub>2</sub> im Reservoir abbilden können und einen Beitrag zur Quantifizierung geometrischer und petrophysikalischer Parameter der CO<sub>2</sub>-Fahne leisten. Im Rahmen der Überwachung einer CO<sub>2</sub> Speicherung, sollten bohrlochseismische Methoden neben einer Oberflächen-seismik zum Einsatz kommen, falls detailliertere Informationen über die Struktur in der näheren Umgebung einer Bohrung benötigt werden. Bohrlochseismische Überwachung kann zusätzlich zur Beobachtung von Schichten über dem Reservoir, der Detektion von Leckagepfaden oder zur Überprüfung der Bohrlochintegrität eingesetzt werden.

---

# Contents

<b>1</b>	<b>Introduction</b>	<b>1</b>
1.1	Geological storage of CO <sub>2</sub> . . . . .	1
1.2	CO <sub>2</sub> storage and scientific program at the Ketzin pilot site . . . . .	2
1.3	Crosshole seismic, zero-offset and offset VSP, motivation and published results . . . . .	5
1.3.1	Overview and motivation . . . . .	5
1.3.2	Crosshole seismic, published results . . . . .	6
1.3.3	Zero-offset VSP, published results . . . . .	7
1.4	Research objectives and structure of the thesis . . . . .	7
<b>2</b>	<b>Overview of the Ketzin site</b>	<b>9</b>
2.1	Geology . . . . .	9
2.2	Site development . . . . .	11
2.3	Reservoir characterisation . . . . .	12
2.3.1	Analysis of the cored section . . . . .	12
2.3.2	Pumping tests . . . . .	13
2.3.3	Petrophysical laboratory experiments (P-wave, S-wave, CO <sub>2</sub> saturation) . . . . .	13
2.4	Well cementing, well deviation, sonic and density logging . . . . .	14
2.4.1	Well cementing . . . . .	15
2.4.2	Well deviation . . . . .	15
2.4.3	Sonic and density logging . . . . .	16
<b>3</b>	<b>Theoretical Background</b>	<b>19</b>
3.1	The swept impact seismic technique (SIST) . . . . .	19
3.2	Principal Component Analysis (PCA) . . . . .	20
3.3	Tomography with FAST . . . . .	21
3.4	Band limited impedance inversion . . . . .	23
3.4.1	The algorithm . . . . .	23
3.4.2	Conversion of the acoustic impedance to P-wave velocity . . . . .	26
3.5	Fresnel zone based sensitivity kernels . . . . .	27
<b>4</b>	<b>Crosshole: baseline, 1st and 2nd repeat</b>	<b>29</b>
4.1	Motivation and research objectives . . . . .	29
4.2	Equipment and recording parameters . . . . .	29
4.3	Source-receiver configuration . . . . .	32
4.4	Data sets . . . . .	34
4.5	Frequency content . . . . .	37
4.6	Picking the first breaks . . . . .	38
4.7	Travel time tomography . . . . .	39
4.7.1	FAST: Input parameters and mode of operation . . . . .	39
4.7.2	Results of the travel time tomography . . . . .	43

4.8	Simulated CO <sub>2</sub> injection: Forward calculation and tomography of travel times . . . . .	47
4.9	Conclusions . . . . .	50
<b>5</b>	<b>Zero-offset VSP: baseline and repeat</b>	<b>53</b>
5.1	Motivation and research objectives . . . . .	53
5.2	Equipment and recording parameters of the zero-offset VSP . . . . .	53
5.3	Geometry of the zero-offset VSP . . . . .	55
5.4	Processing the zero-offset VSP data . . . . .	55
5.4.1	Influence of uncemented casing on data . . . . .	55
5.4.2	Processing . . . . .	56
5.5	Frequency before and after processing . . . . .	60
5.6	Comparison of zero-offset VSP with 3D surface seismic . . . . .	61
5.7	Modelling of zero-offset VSP data . . . . .	63
5.7.1	Petrophysical model parameters . . . . .	63
5.7.2	2D Finite Difference (FD) modelling . . . . .	65
5.7.3	Processing . . . . .	66
5.7.4	CO <sub>2</sub> signature of measured and modelled zero-offset VSP . . . . .	67
5.7.5	Estimation of CO <sub>2</sub> layer thickness from zero-offset VSP data . . . . .	69
5.8	Band limited impedance inversion of measured and modelled zero-offset VSP . . . . .	70
5.8.1	Depth-to-time conversion of sonic log Ktzi 202 . . . . .	70
5.8.2	Band limited impedance inversion . . . . .	72
5.9	Conclusions . . . . .	75
<b>6</b>	<b>Offset VSP: baseline and repeat</b>	<b>77</b>
6.1	Motivation and research objectives . . . . .	77
6.2	Equipment and recording parameters . . . . .	77
6.3	Measurement geometry . . . . .	78
6.4	Offset VSP processing . . . . .	80
6.5	Time-to-depth conversion of 3D surface seismic . . . . .	84
6.5.1	3D surface seismic rms-velocities to interval velocities . . . . .	84
6.5.2	Time-to-depth conversion of 3D surface seismic . . . . .	85
6.6	Kirchhoff and Fresnel depth migration . . . . .	86
6.6.1	Kirchhoff migration . . . . .	86
6.6.2	Fresnel migration . . . . .	88
6.6.3	Comparison of Kirchhoff and Fresnel migration results . . . . .	95
6.7	Modelling of offset VSP data . . . . .	100
6.8	Conclusions . . . . .	104
<b>7</b>	<b>Summary</b>	<b>107</b>
	<b>Acknowledgements</b>	<b>113</b>
<b>A</b>	<b>Offset VSP: comparison of Kirchhoff and Fresnel migration</b>	<b>123</b>

# 1

## Chapter 1

---

# Introduction

*In this chapter the general motivation for underground CO<sub>2</sub> storage is explained and the CO<sub>2</sub> storage site in Ketzin is introduced. An overview over the borehole seismic measurements is given. Finally the research objectives and the structure of the thesis are described.*

## 1.1 Geological storage of CO<sub>2</sub>

This thesis is about borehole seismic monitoring of CO<sub>2</sub> storage within a saline aquifer at Ketzin, Germany. CO<sub>2</sub> storage is part of the process 'Carbon dioxide Capture and Storage (CCS)'. CCS consists "of the separation of CO<sub>2</sub> from industrial and energy-related sources, the transport to a storage location, and a long-term isolation from the atmosphere" (IPCC (2005)).

As a greenhouse gas, CO<sub>2</sub> contributes to the global warming. Efforts to reduce global warming involve slowing down the increase of CO<sub>2</sub> concentration in the atmosphere. Since the industrial revolution, CO<sub>2</sub> concentration in the atmosphere has risen from 280 ppm to 380 ppm (IPCC (2005)). Most of the increase is attributed to the burning of carbon rich fossil fuels like coal, natural gas and oil. CCS is one of the options to reduce CO<sub>2</sub> emissions, the others "include energy efficiency improvements, the switch to less carbon intensive fuels, nuclear power, renewable energy sources, and the enhancement of biological sinks" (IPCC (2005); Kühn (2011)).

CCS is considered because "fossil fuels are the dominant form of energy utilised in the world (86%) and account for 75% of current anthropogenic CO<sub>2</sub> emissions. Most scenarios project that the supply of primary energy will continue to be dominated by fossil fuels until at least the middle of the century" (IPCC (2005)). In addition, "CCS has the potential to reduce overall mitigation costs and increase the flexibility in achieving greenhouse gas emission reduction" (IPCC (2005)).

Deep saline aquifer storage is "the most promising and relevant CO<sub>2</sub> sequestration option for Europe" (Juhlin et al. (2007)). Saline aquifers are broadly distributed "and their storage capacity exceeds that of depleted oil and gas fields" (Juhlin et al. (2007)). "Techniques developed for the exploration of oil and gas reservoirs, natural gas storage sites and liquid waste disposal sites are suitable for characterising and monitoring geological storage sites for CO<sub>2</sub>" (IPCC (2005)). Although these methods include many of the physical, chemical and geomechanical tools "needed to predict both short-term and long-term performance of CO<sub>2</sub> storage, more experience is needed to establish confidence in their effectiveness in predicting long-term performance when adapted

for CO<sub>2</sub> storage” (IPCC (2005)). The main questions to a scientific program for CO<sub>2</sub> storage are (IPCC (2005)):

- Before selecting a site: What is the geological setting? How will be the performance of the site?
- Will the overlying cap rock provide an effective seal?
- Is there a sufficiently voluminous and permeable storage formation?
- Will any abandoned or active wells compromise the integrity of the seal?
- Are there any leakage routes?
- Is it possible to track the underground migration of CO<sub>2</sub>?
- Is it possible to monitor the amount of CO<sub>2</sub> stored in the underground? ”Given the long-term nature of CO<sub>2</sub> storage, site monitoring may be required for very long periods” (IPCC (2005)).

### 1.2 CO<sub>2</sub> storage and scientific program at the Ketzin pilot site

Operated by the German Research Centre for Geosciences (GFZ), the in situ laboratory for saline aquifer CO<sub>2</sub> storage near the town Ketzin (35 km west of Berlin) is the first European onshore storage pilot facility. It advances ”the understanding of the science and practical processes involved in underground storage” (Förster et al. (2006)). As a demonstration project for CO<sub>2</sub> storage, it fills ”the gap between numerous conceptual engineering and scientific studies on geological storage and a fully-fledged onshore storage demonstration” (Juhlin et al. (2007)). Within 5 years of operation, between June 2008 and April 2013, 65 kt of supercritical, food-grade CO<sub>2</sub> have been injected (Borm and Förster (2005); Schilling et al. (2009); Würdemann et al. (2010); Martens et al. (2011, 2012)).

The CO<sub>2</sub> storage site at Ketzin is part of an anticlinal structure in the northeast German Basin (Fig. 1.1). The site selected for the CO<sub>2</sub> injection is ”an example for physical trapping of CO<sub>2</sub> in closed geological structures (anticlines) below low-permeability seals (cap rocks). This type of trapping mechanism is typical for many potential storage sites in the mid-European basin system” (Förster et al. (2006)). Close to the injection site the reservoir sandstone in the upper part of the Triassic Stuttgart Formation is located at a depth of 630-650 m below ground level. The anticline at Ketzin was used for natural gas storage until the year 2000 in a shallower depth interval of 250-400 m below ground level in Jurassic sandstones by Verbundnetz Gas AG (Fig. 1.1). ”The mining permit granted to Verbundnetz Gas AG by the mining authority of the state of Brandenburg to operate at Ketzin, on the one hand, and the favourable geological conditions for CO<sub>2</sub> storage at greater depth, on the other, were the driving forces for selecting the Ketzin anticline as a test-injection and monitoring site” (Förster et al. (2006)).

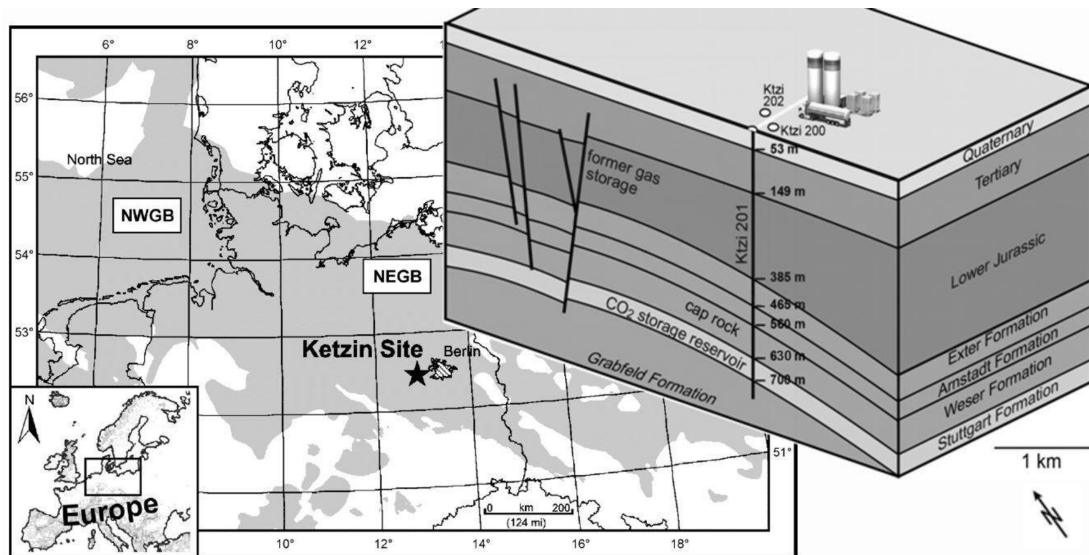


Figure 1.1: Location and structure of the Ketzin storage site. Left (background, after Förster et al. (2006)): "Map of the mid-European Permian basin (grey shaded). The Ketzin site is marked as a star. NEGB denotes the northeast German Basin and NWGB denotes the northwest German Basin" (Förster et al. (2006)). Right (foreground): Schematic and vertically exaggerated block diagram of the Ketzin storage site (not to scale, modified after Liebscher et al. (2012a)) illustrating the structure and stratigraphy of the Ketzin anticline. The target CO<sub>2</sub> storage zone in the upper part of the Stuttgart Formation covers the range of 630 - 650 m below ground level.

The CO<sub>2</sub> storage at Ketzin is accompanied by a comprehensive scientific program (Giese et al. (2009)). Central to this program is not only a combination of techniques such as geoelectric, seismic, temperature and pressure monitoring as well as fluid and gas sampling, but also different methods with variable temporal and spatial resolution within the respective technique. The following list gives an overview over the Ketzin scientific program:

- Well design, drilling and completion of three smart wells, containing a variety of permanently installed downhole sensors for the continuous monitoring of the CO<sub>2</sub> in the reservoir (Prevedel et al. (2008, 2009); Möller et al. (2012)).
- Monitoring and modelling of injection rates, well pressure and temperature (Freifeld et al. (2009); Wiese et al. (2010b); Henniges et al. (2011)).
- Various borehole logging techniques (sonic, density, cement bond, pulsed neutron gamma...) and the interpretation of cores (Prevedel et al. (2008, 2009); Norden et al. (2010); Ivanova et al. (2012)).
- Pumping tests for hydraulic characterisation of the storage formation (Wiese et al. (2010a)).
- Microbiological analyses in the wells (Morozova et al. (2010, 2011); Wandrey et al. (2010, 2011a,b); Zettlitzer et al. (2010)).
- Analyses of rock samples, gases and fluids from the subsurface (Muller et al. (2009); Fischer et al. (2010, 2011); Myrntinen et al. (2010); Zemke et al. (2010); Kummerow and Spangenberg (2011); Rempel et al. (2011); Scherf et al. (2011); Zimmer et al. (2009, 2011a)).

- Geological description of the site, the reservoir and the cap rocks (Förster et al. (2006, 2009, 2010)).
- Geotechnical investigations of the reservoir and the cap rocks (Mutschler et al. (2009); Ouellet et al. (2011)).
- Long-term surface carbon dioxide flux monitoring (Zimmer et al. (2011b)).
- Numerical modelling to evaluate the subsurface migration of the CO<sub>2</sub> and to assess the integrity and safety of the reservoir (Frykman et al. (2009); Kopp et al. (2009); Pamukcu and Hurter (2009); Kempka et al. (2010); Lengler et al. (2010); Lengler (2012); Liebscher et al. (2012b)).
- Groundwater flow modelling (Norden (2011)).

An important part of the scientific program is the geophysical site characterisation and the monitoring of the subsurface migration of CO<sub>2</sub> by several surface and surface-to-borehole methods (Liebscher et al. (2012b)).

- Active seismic: Juhlin et al. (2007); Yordkayhun et al. (2007, 2009a,b,c); Kazemeini et al. (2009, 2010a,b); Yang et al. (2010); Arts et al. (2011); Bergmann et al. (2011); Götz et al. (2011); Lüth et al. (2011); Ivandic et al. (2012); Ivanova et al. (2012); Zhang et al. (2012); Liebscher et al. (2012b); Yang (2012)
- Geoelectric: Bergmann et al. (2010); Kießling et al. (2010); Schmidt-Hattenberger et al. (2011); Labitzke (2012); Bergmann et al. (2012)
- Controlled source electromagnetic (CSEM): Girard et al. (2011)
- Passive seismic: Xu et al. (2012)

One of the key results of the 3D surface seismic monitoring is a map of the distribution of CO<sub>2</sub> in the reservoir (Ivandic et al. (2012)). Figure 1.2 shows the normalised amplitude difference (repeat minus baseline) at the reservoir horizon (top of Stuttgart Formation). The difference is the result of time-lapse processing of the baseline and repeat surveys, which were measured autumn 2005 and autumn 2009, respectively. At the time of the repeat survey 22-25 kt have been injected. The CO<sub>2</sub> is visible in the difference map as strong amplitudes at the time interval of the reservoir.

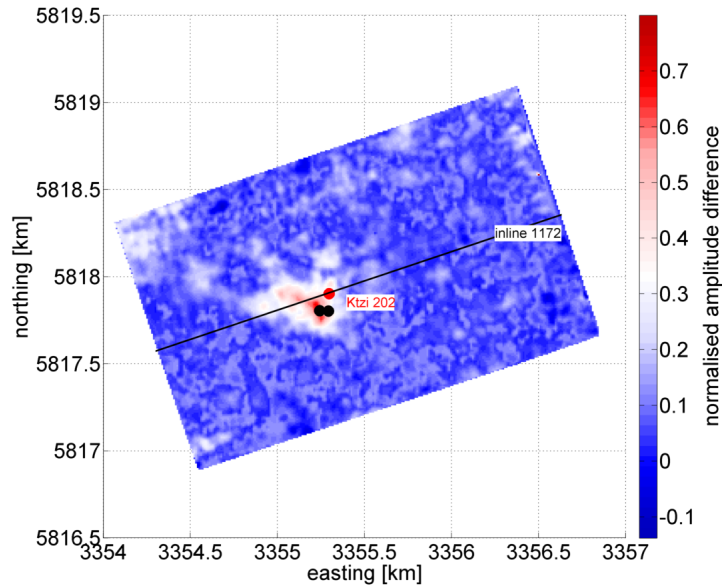


Figure 1.2: Map of the normalised amplitude difference (repeat minus baseline) at the reservoir horizon (top of Stuttgart Formation). The difference is the result of time-lapse processing of the 3D surface seismic baseline (measured autumn 2005) and repeat surveys (measured autumn 2009, Ivandic et al. (2012)). The Ketzin wells are marked as dots. The inline 1172, which is crossing the observation well Ktzi 202 is indicated by the black line.

## 1.3 Crosshole seismic, zero-offset and offset VSP, motivation and published results

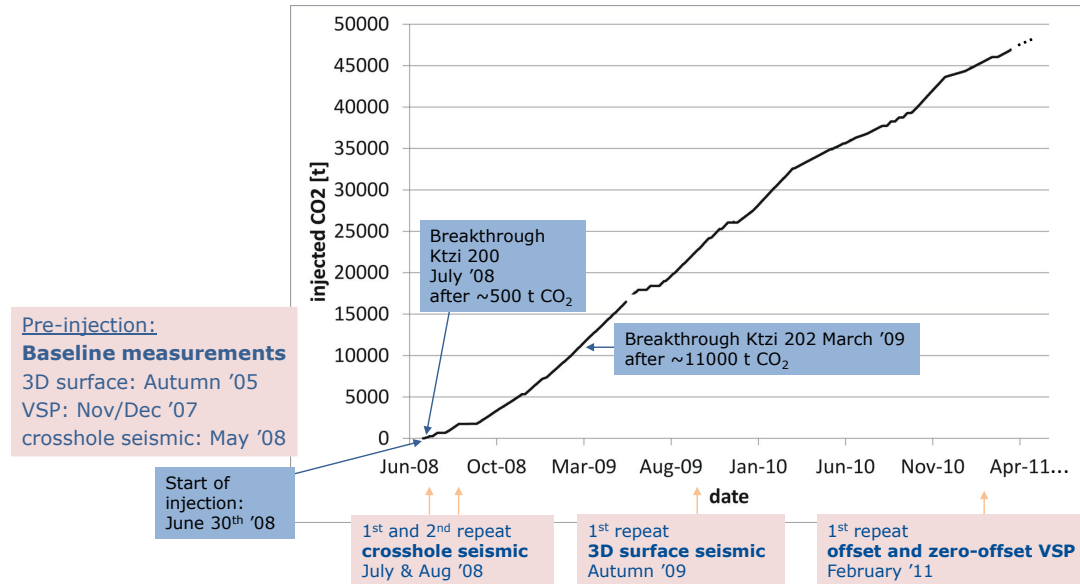
### 1.3.1 Overview and motivation

As part of a comprehensive geophysical monitoring program at Ketzin (Chap. 1.2), the research in this thesis focuses on the crosshole seismic, zero-offset and offset VSP measurements in Ketzin. While the baseline surveys provide the structural geometry and characterisation of the site, the repeat surveys aim at the observation of CO<sub>2</sub> propagation in the reservoir.

**Crosshole seismic:** The crosshole seismic measurement was designed to follow the migration of CO<sub>2</sub> at small scale during the injection. "As CO<sub>2</sub> replaces saline water in saturated reservoir sandstones a P-wave velocity reduction may occur. This velocity change can potentially be used to monitor CO<sub>2</sub> in sandstone aquifers using seismic tomography" (Zhang et al. (2012)). Prior to injection the crosshole seismic baseline was measured in May 2008 (Fig. 1.3). Injection started on 30 June 2008 and the CO<sub>2</sub> needed 15 days (500 t CO<sub>2</sub> injected) to migrate 50 m from the injection well Ktzi 201 to the observation well Ktzi 200. Since an equally fast propagation was expected towards Ktzi 202, two repeat measurements were scheduled shortly after the first breakthrough. The 1st repeat followed end of July 2008 after 660 t of CO<sub>2</sub> injected, the 2nd repeat followed end of August 2008 after 1750 t of CO<sub>2</sub> injected.

**Zero-offset and offset VSP:** The main objective of the zero-offset and offset VSP surveys was to generate high-resolution seismic images in the vicinity of the borehole. As CO<sub>2</sub> replaces saline water in saturated sandstones, the impedance contrast between

the gas filled sandstones and the caprock is increased, what leads to stronger reflections from top of the reservoir. This increased reflectivity can be used to image the spreading of CO<sub>2</sub> in the reservoir. Prior to injection the zero-offset and offset VSP baselines were measured November/December 2007 (Fig. 1.3). The repeat of the zero-offset VSP was measured February 2011 (45770 t CO<sub>2</sub> injected), together with the repeat of the offset VSP.



3D surface seismic	baseline	autumn 2005	
zero-offset and offset VSP	baseline	November/December 2007	
crosshole seismic	baseline	11 - 14 May 2008	
<i>start of injection</i>		<i>30 June 2008</i>	
<i>breakthrough in Ktzi 200</i>		<i>15 July 2008, after 15 days</i>	<i>500 t</i>
crosshole seismic	1st repeat	26 - 30 July 2008	660 t
crosshole seismic	2nd repeat	28 August - 3 September 2008	1750 t
<i>breakthrough in Ktzi 202</i>		<i>20 March 2009, after 263 days</i>	<i>11030 t</i>
3D surface seismic	1st repeat	autumn 2009	22 - 25 kt
zero-offset and offset VSP	1st repeat	February 2011	45770 t
3D surface seismic	2nd repeat	autumn 2012	61000 t

Figure 1.3: Timeline of 3D surface seismic, crosshole seismic, zero-offset and offset VSP measurements in Ketzin. Top: Dates of the measurements versus the injected CO<sub>2</sub> in tons. The start of injection and the breakthrough are also shown. Bottom: Table with the correspondent dates and tons of CO<sub>2</sub> injected.

### 1.3.2 Crosshole seismic, published results

Prior to injection the crosshole seismic baseline was measured. Injection started on 30 June 2008 and the CO<sub>2</sub> needed 15 days to migrate 50 m from the injection well Ktzi 201 to the observation well Ktzi 200 (Fig. 2.4). Since an equally fast propagation was expected towards Ktzi 202, two repeat measurements were scheduled shortly after the first breakthrough (Chap. 1.3.1). It was hoped to monitor the migration of the CO<sub>2</sub> between the observation wells. But since the CO<sub>2</sub> needed 263 days to reach Ktzi 202, only a small amount of CO<sub>2</sub> had migrated into the imaging plane during the 1st and

2nd repeat. Hence, the time-lapse observations did not observe significant travel time changes due to CO<sub>2</sub> saturation in the Stuttgart Formation (Lüth et al. (2011)).

According to Lüth et al. (2011), a time-lapse signature could be identified in the data by a more sensitive estimate of the change in seismic response than the travel times. This method consists of "a multiplication of the cross-correlation of corresponding baseline and repeat records with the logarithm of their amplitude ratios, in a 20 ms window after the picked P-wave times" (Lüth et al. (2011)). An amplitude variation between baseline and repeat survey was found, which is concentrated in the vicinity of observation well Ktzi200. The conclusion is, that at "the time of the crosshole repeat surveys, the amount of CO<sub>2</sub> between the two observation wells was sufficient to slightly affect the amplitudes of transmitted seismic waves (change in attenuation) but it was not sufficient to significantly affect the average propagation velocities between the observation wells" (Lüth et al. (2011)).

Zhang et al. (2012) presented a case study of time-lapse crosshole seismic waveform tomography for monitoring CO<sub>2</sub> injection. "Classical P-wave travel time tomography was not capable of detecting any velocity differences caused by CO<sub>2</sub> injection in the real data. Application of seismic waveform tomography to the real data showed some zones of decreased velocity between the two observation wells. Some of these zones may be artefacts due to poor receiver coupling, but a subhorizontal anomaly at the base of the caprock may be due to CO<sub>2</sub> injection. The location of the anomaly, the observed velocity change and the fact that it appears in the same location on both repeats are evidence for it being due to the injection of CO<sub>2</sub>. However, the anomaly should not be overinterpreted. The lack of a continuous channel of CO<sub>2</sub> between the wells makes interpretation of the seismic waveform tomography results more difficult" (Zhang et al. (2012)).

### 1.3.3 Zero-offset VSP, published results

Kazemeini et al. (2010b) performed a study on enhancing seismic data resolution using the prestack blueing technique. He used the high resolution baseline zero-offset VSP data as a reference when comparing the efficiency of the different blueing techniques. Kazemeini et al. (2010b) noticed that in the upper part of the survey no clear first arrivals could be identified, probably because of a poorly cemented casing. A routine VSP processing flow was applied to the data not influenced by casing waves with only the vertical component of the data being processed. "The wavefield separation was done using a 1D median filter combined with a bandpass filter applied on the flattened downgoing P-waves. The final output was a corridor stacked trace that is reproduced and plotted as several traces to facilitate comparison with the 3D seismic" (Kazemeini et al. (2010b)). The zero-offset VSP data are compared with a 3D surface seismic inline passing across the well (Fig. 1.2). The results of 3D seismic data with no blueing, from the poststack and prestack blueing are compared. It was found that "the higher resolution zero-offset VSP data show a better match with the prestack and poststack blued sections" (Kazemeini et al. (2010b)).

## 1.4 Research objectives and structure of the thesis

This thesis is about borehole seismic monitoring of CO<sub>2</sub> storage within a saline aquifer at Ketzin, Germany. Based on geological information and well cores, the reservoir is described as thin and heterogeneous at the research site (Yang (2012)). "The thickness

of the reservoir is generally less than 20 m”, what is ”below the resolution of conventional surface seismic data” (Yang (2012)). Borehole seismic methods are expected to have a higher resolution than surface seismic, therefore three different borehole seismic methods are tested:

- Crosshole seismic and its ability to follow the migration of CO<sub>2</sub> at small scale during the injection,
- zero-offset VSP for providing near-well corridor stacks and information about normal incidence reflectivity and
- offset VSP with the potential to generate a lateral image of the reservoir at the injection site.

The main questions to be answered are: With these methods, is it possible (1) to map the CO<sub>2</sub> in the reservoir layer and (2) to derive geometrical and petrophysical parameters describing the migration of CO<sub>2</sub> in a water saturated sandstone reservoir? The thesis is structured according to the methods applied. After the introduction, an overview of the Ketzin site is presented (Chap. 2), followed by Chapter 3 covering the theoretical background. Chapters 4 to 6 cover successively the crosshole, zero-offset and offset VSP measurements at Ketzin. Chapter 7 is the summary of the thesis.

# 2 Chapter 2

## Overview of the Ketzin site

*This chapter covers the geological background and the site development in Ketzin. The reservoir sandstone is specified by analysis of well cores, pumping tests and petrophysical laboratory experiments. Well logging results needed for the evaluation of the crosshole, zero-offset and offset VSP data are presented.*

### 2.1 Geology

**Overview:** The Ketzin storage site is located at the southern flank of the eastern part of the Roskow-Ketzin double anticline in the northeast German Basin (Figs. 1.1 and 2.1, Förster et al. (2006)). The anticline formed above an Upper Permian salt pillow situated at a depth of 1500-2000 m (Norden et al. (2010)). The axis of the anticline strikes SW-NE and its flanks gently dip at about 15°.

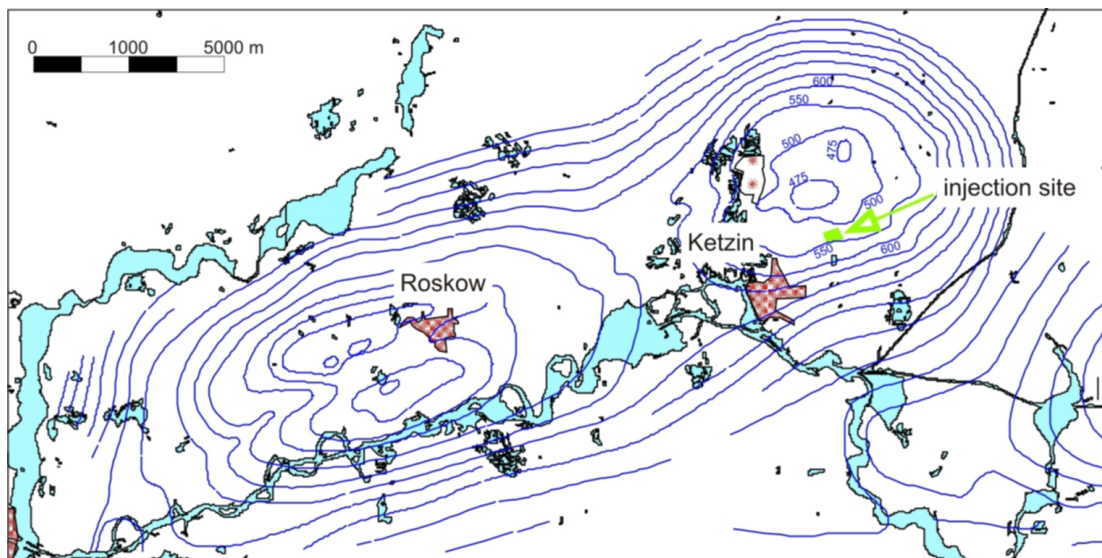


Figure 2.1: Structure of the Roskow-Ketzin double anticline (Norden et al. (2010), modified). The Ketzin site is indicated by the green rectangle. The blue isolines ( $\Delta = 50$  m) map the depth of the K2 reflector (top of the Weser Formation, Fig. 2.2) based on vintage seismic data. The depth of the K2 close to the injection site is 550 m below ground level.

The overburden of the salt comprises sedimentary rocks of the German Triassic

(Buntsandstein, Muschelkalk, Keuper) and of the Lower Jurassic, Tertiary and Quaternary (Fig. 2.2). The CO<sub>2</sub> is being injected into the upper part of the Triassic Stuttgart Formation at 630-650 m below ground level.

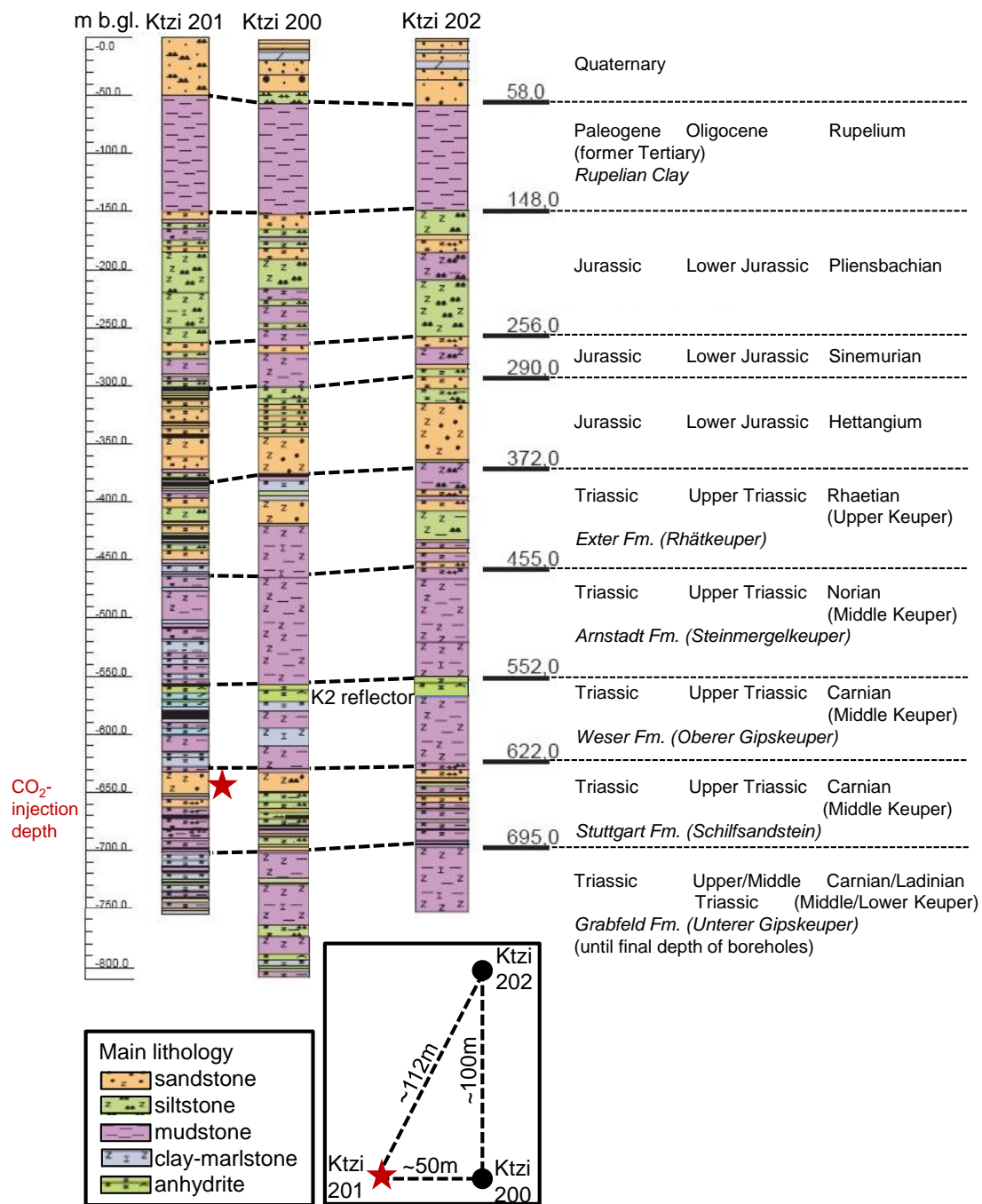


Figure 2.2: Stratigraphic and lithological sections of the three boreholes (Kazemeini et al. (2010b), modified). The CO<sub>2</sub> injection horizon is marked with a star. The top of the Weser formation, a 10-20 m anhydrite bed, is known as a good seismic reflector, the K2 reflector. The depth is in meter below ground level [m b.gl.].

**Faults:** The baseline 3D seismic survey over the Ketzin anticline provided information on existing faults (Juhlin et al. (2007)). At the top of the Ketzin dome clear faults are

observed, which form a central graben and extend down into Stuttgart formation. No obvious faults are observed near the planned injection site or within the range of the surface-to-borehole measurements.

**Topography:** Figure 2.3 displays the topography of Ketzin in an area covering the borehole seismic activities. The topography is relatively flat (around 34 m above sea level), but does contain some isolated highs (up to 50 m above sea level) consisting mainly of Quaternary sands (Juhlin et al. (2007)).

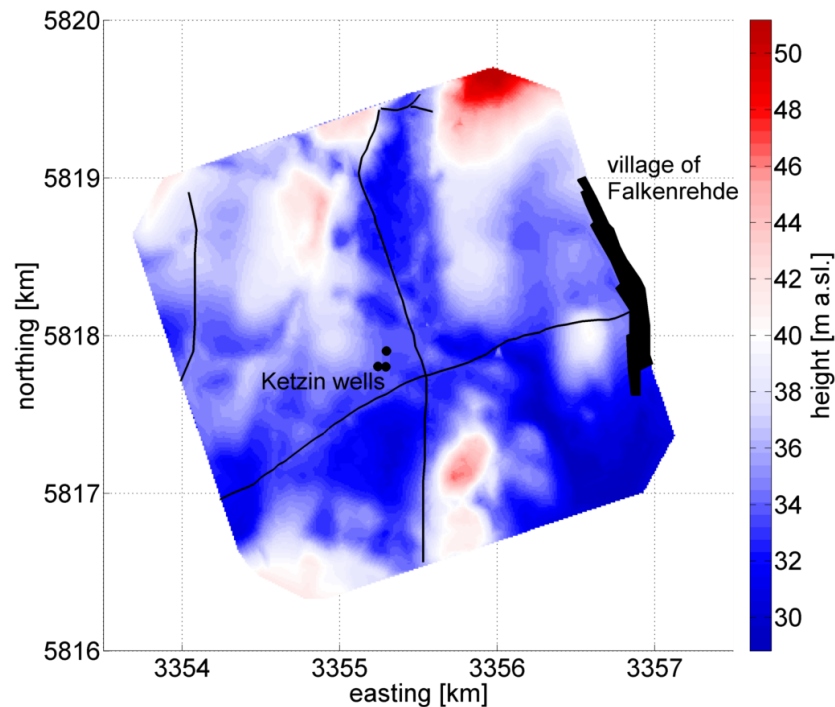


Figure 2.3: Topography around the injection site. The displayed area covers the region of borehole seismic activities. The three wells are marked with black dots. Streets are indicated by black lines, and the village of Falkenrehde is shown in the eastern part of the region. The topographic height is in meter above sea level [m a.s.l.].

## 2.2 Site development

Three boreholes, one injection well and two observation wells were drilled into the flank of the Roskow - Ketzin double anticline (Figs. 2.1 and 2.4, Prevedel et al. (2008, 2009)). The injection well has the designation 'CO<sub>2</sub> Ktzi 201/2007'. The observation wells are named 'CO<sub>2</sub> Ktzi 200/2007' and 'CO<sub>2</sub> Ktzi 202/2007'. For better readability the wells will be termed Ktzi 201 (injection well), Ktzi 200 and Ktzi 202 (observation wells) in the following. The two observation wells were drilled to support the monitoring and allowed to observe the migration of CO<sub>2</sub> in the storage formation. Figure 2.4 is an aerial view of the storage site: The injection well Ktzi 201 is located in the south-west part of the injection site, the observation well Ktzi 200 is 50 m east of the injection well and the observation well Ktzi 202 is 100 m north of Ktzi 200. Table 2.1 lists the coordinates and distances of the three wells in Ketzin (Rinke (2007)). "The choice of the relative well positions has been guided by geological and physical constraints to optimize the spatial resolution of the various monitoring methods, e.g. crosshole seismic and Electrical

Resistivity Tomography (ERT, Schmidt-Hattenberger et al. (2011)), in accordance to the planned injection volume of CO<sub>2</sub>” (Prevedel et al. (2009)). Injection of pure CO<sub>2</sub> started on the 30th June 2008. The CO<sub>2</sub> is injected in supercritical state with a mean injection rate of 46 t per day. Within 5 years of operation, between June 2008 and in April 2013, 65 kt of food-grade CO<sub>2</sub> have been injected. The initial reservoir conditions were 33.5 °C and 6.1 MPa at 630 m below ground level (Henniges et al. (2011)).

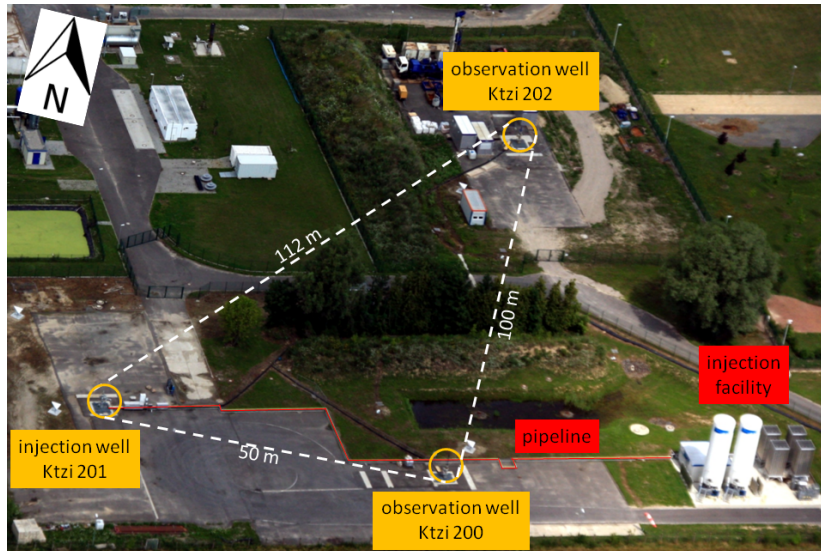


Figure 2.4: Areal view of the storage site. The yellow circles mark the locations of the three wells (Ktzi 200, Ktzi 201, Ktzi 202). The red line shows the pipeline which connects the two CO<sub>2</sub> storage tanks with the injection well. The distances between the three wells are indicated. In summer 2012 the observation well Ktzi 203 (not shown in this figure) has been drilled in 25 m distance to the injection well.

Table 2.1: Coordinates (UTM ETRS 89), heights in meter above sea level [m a.s.l.] and distances of the three Ketzin wells (Rinke (2007)).

Ktzi 201 (injection well)	(33) 355242.7	5817803.7	33.5 m a.s.l.
Ktzi 200 (observation well)	(33) 355292.7	5817801.6	33.6 m a.s.l.
Ktzi 202 (observation well)	(33) 355296.8	5817901.4	33.5 m a.s.l.
distances between the wells	Ktzi 201 to Ktzi 200	50.0 m	
	Ktzi 201 to Ktzi 202	111.7 m	
	Ktzi 200 to Ktzi 202	99.9 m	

## 2.3 Reservoir characterisation

### 2.3.1 Analysis of the cored section

”For a detailed characterization of the 72 m thick Stuttgart Formation and of the sealing properties at Ketzin, ~200 m of core was retrieved for laboratory analyses to be interpreted in combination with well-logging data” (Norden et al. (2010)).

**The reservoir:** ”The three wells, 50- 112 m apart, show a different lithostratification of the Stuttgart Formation, attesting lateral changes and cyclicity in fluvial sedimentation”

(Förster et al. (2009), Fig. 2.2). The Stuttgart formation consists of "sandstone, siltstone, and mudstone intervals, the latter interbedded with variable amounts of anhydrite and minor coal" (Norden et al. (2010)). "The fluvial sandstones" of the reservoir "are fine-grained to medium-grained and well-sorted" (Förster et al. (2009)). "In all wells, the upper part of the Stuttgart Formation hosts a permeable main reservoir sandstone with a thickness of 9-20 m" (Norden et al. (2010)).

In the Ktzi 200 and Ktzi 201 boreholes, the upper main reservoir "sandstone unit is 18-20 m thick, subdivided into two permeable sandstone layers separated from each other by a strongly cemented sandstone layer" (Norden et al. (2010)). In the Ktzi 202 borehole the reservoir sandstone is 8 m thick (Fig. 2.2). The main contents of the reservoir sandstone are quartz, feldspar and a variably high illite content (Norden et al. (2010)). "Cement distribution in most samples is characterised by local cement concentrations in spotted zones with high intergranular volume" (Förster et al. (2009)). "The saline aquifer at Ketzin shows a variable porosity/permeability distribution, which is related to grain size, facies variation, and rock cementation" (Norden et al. (2010)). "The core analyses and borehole logs show an effective aquifer porosity of about 20 %." The layer's average horizontal core permeabilities range between 500 mD and 1100 mD" (Wiese et al. (2010a)).

**The cap rock system:** "The top seal of the CO<sub>2</sub> storage formation, the Weser Formation, was deposited in a clay/mud-sulfate playa environment" (Förster et al. (2009)). "The playa-type mudstones of the Weser and Arnstadt formations" together form a 170 m "thick cap rock section above the Stuttgart Formation" (Förster et al. (2006), Fig. 2.2). The main mineral contents of the mudstones in the cored section of the Weser Formation are illite, dolomite and anhydrite (Förster et al. (2009)). "Ambient He-porosity ranges from 5-15 %. The higher values (>10 %) are observed in finely fractured rocks. The average gas-permeability is 0.01 mD; no significant correlation exists between gas permeability and porosity. Pore bodies and pore throats are small (<500 nm and 10-36 nm, respectively); the pore space is usually unconnected. The high clay mineral content and the observed pore space geometry attest good sealing properties" (Förster et al. (2009)).

### 2.3.2 Pumping tests

"Hydraulic testing evaluated as single-hole tests revealed" permeabilities of 50-100 mD for the reservoir (Würdemann et al. (2010); Wiese et al. (2010a)). "Considering that core permeabilities are one order of magnitude higher than pumping test permeabilities (Chap. 2.3.1)", Wiese et al. (2010a) "conclude that the latter values are clearly more representative of injection behaviour. The fact that core permeabilities are much higher than pumping test values is very unusual and it appears to be a unique feature of the field site. It also implies that the sandstone body is not continuous, but intersected by continuous low-permeability layers or regions" (Wiese et al. (2010a)).

### 2.3.3 Petrophysical laboratory experiments (P-wave, S-wave, CO<sub>2</sub> saturation)

*The reduction of P-wave velocity due to CO<sub>2</sub> injection will be used for the forward calculation of synthetic crosshole travel times (Chap. 4.8).*

The effect of CO<sub>2</sub> injection on the P-wave and S-wave velocities of the Ketzin reservoir was investigated at laboratory scale by Kummerow and Spangenberg (2011). The experiments were carried out on a sample from the reservoir sandstone of the Stuttgart

Formation which was cored from the well Ktzi 202 at 629 m below ground level. The sample has a porosity of 28 %. "In thin sections the distribution of porosity is inhomogeneous with less porous lenticular clay layers and porous grain supported sandstone layers" (Kummerow and Spangenberg (2011)). To mimic reservoir conditions, the sample was saturated with a synthetic formation brine and the flow experiments were performed at the conditions of the Ketzin reservoir ( $p_{confining} = 15$  MPa,  $p_{pore} = 7.5$  MPa,  $T = 40$  °C). First, pure supercritical CO<sub>2</sub> was injected in the completely brine saturated sample, which was then re-saturated with brine. Since there was no opportunity for a direct determination of water saturation of the sample during the experiments in the high-pressure cell, the water saturation was estimated from resistivity measurements. "Ultrasonic measurements were performed in the pulse transmission mode at a resonance frequency of 500 kHz" (Kummerow and Spangenberg (2011)).

CO<sub>2</sub> injection had hardly an effect on the S-wave velocity. An increase of the S-wave velocity with decreasing brine saturation from 1.38 km/s to 1.40 km/s was found (velocity change  $\sim 2\%$ ). "The measured P-wave velocity versus brine saturation is shown in Figure 2.5. The P-wave velocities  $v_p$  show a hysteretic behaviour resulting from a relative rapid decrease of  $v_p$  with decreasing brine saturation from 3.20 km/s to 2.69 km/s (16 %) and a hesitant increase of  $v_p$  at brine imbibition. The P-wave velocity reaches its initial value after the sample is re-saturated with brine at the end of the experiment" (Kummerow and Spangenberg (2011)).

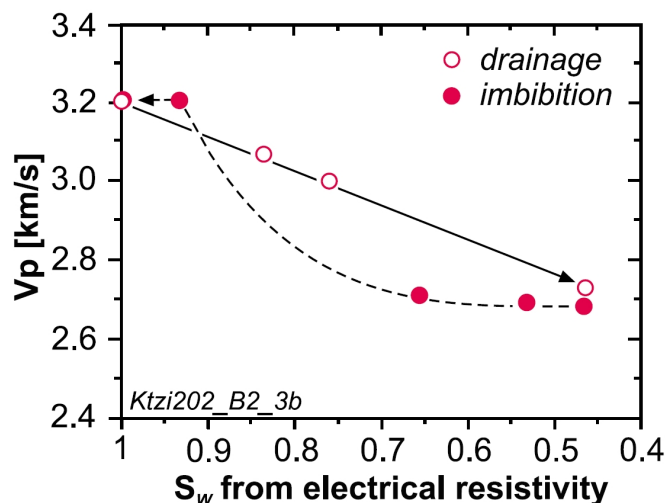


Figure 2.5: P-wave velocity  $v_p$  as function of the brine saturation  $S_w$  of the sample (Kummerow and Spangenberg (2011)).

## 2.4 Well cementing, well deviation, sonic and density logging

Amongst the various employed logging techniques (Norden et al. (2010)), especially the outcome of the cement bond logs, borehole deviation measurements, sonic logs and density logs are described. The borehole measurements were performed by BLM GmbH Gommern on behalf of the GFZ Potsdam. The coordinates of the wells and the horizontal well head distances are listed in Table 2.1 and shown in Figure 2.4.

### 2.4.1 Well cementing

The quality of well cementation had especially an influence on the zero-offset VSP data (Chap. 5.4.1), which was recorded in the observation well Ktzi 202.

According to the reports from Rinke (2007) and Prevedel et al. (2008, 2009) casing and cementation of Ktzi 202 are shown in Figure 2.6. Large parts of the observation well are completed with "multiple casing in which the casing strings are not rigidly cemented to one another and also not to the formation" (Hardage (2000)).

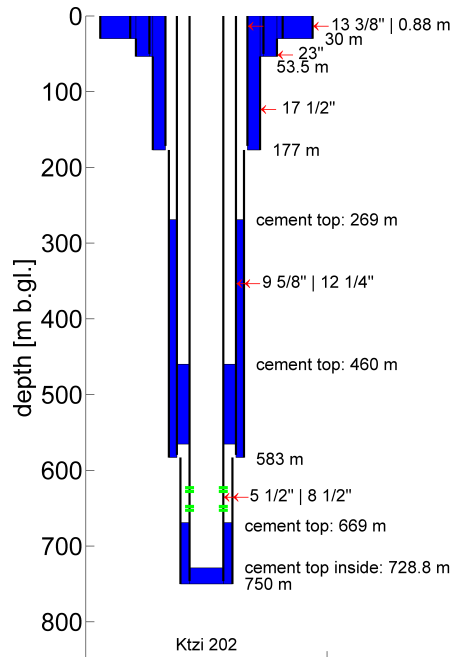


Figure 2.6: Well design and cementation of Ktzi 202. The specifications in inches, e.g. 5 1/2" | 8 1/2", denote the diameter of the casing and of the drilling bit, respectively. The cement is shown in blue colour, the filter screens are indicated in green. The depth is in meter below ground level [m b.g.l.].

### 2.4.2 Well deviation

The well deviation is especially important for the crosshole tomography (Chap. 4.7), since the positional accuracy of sources and receivers is within the range of centimetres. Since the crosshole survey was measured between the observation wells Ktzi 200 and Ktzi 202 the deviation measurements is shown for those wells.

The results of the well deviation measurements are reported in Rinke (2007) and are shown in Figure 2.7.

**Depth displacement:** According to Rinke (2007), the difference between measured depth and true vertical depth is 0.08 m for Ktzi 200 and 0.07 m for Ktzi 202. The depth displacement is not considered in the crosshole tomography. Both wells experience almost the same depth displacement, that means the crosshole sources and receivers are not shifted relative to another. Even if only one well would be shifted by 0.08 m, it would have hardly any effect compared to the 100 m horizontal distance.

**Horizontal displacement:** For both wells no azimuth could be measured in the upper cased section (Ktzi 200: 0 - 160 m below ground level, Ktzi 202: 0 - 171 m below ground level), because directional orientation is not possible through the steel casing. The

azimuth has been extrapolated for this section. For both wells the maximum deviation was found at the bottom of the well: Ktzi 200 has a maximum deviation of 7.3 m at 807 m below ground level, Ktzi 202 has a maximum deviation of 4.8 m at 749 m below ground level.

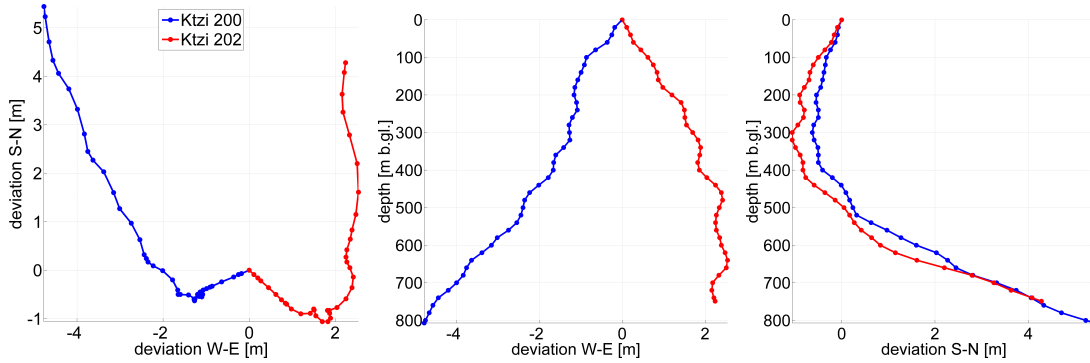


Figure 2.7: Borehole deviation measurements of Ktzi 200 and Ktzi 202. Left: plane view. Middle: West - East side view. Right: South - North side view. The deviation is measured relative to the well head, the depth is in meter below ground level [m b.gl.].

### 2.4.3 Sonic and density logging

For the crosshole tomography the *P*-wave sonic logs of Ktzi 200 and Ktzi 202 are used (Chap. 4.7). The *P*-wave, *S*-wave and density log of Ktzi 202 are needed for the impedance inversion (Chap. 5.8) and modelling of the zero-offset VSP (Chap. 5.7) and offset VSP (Chap. 6).

No sonic information is available down to  $\sim 170$  m below ground level (Zerbe (2007)). Figure 2.8 shows sonic and density logging results in the depth level from 420 - 700 m below sea level together with the lithology within the wells (Norden et al. (2010)). The *P*-wave sonic log is presented for both observation wells, (Fig. 2.8 left and middle, black lines). For Ktzi 202 the *S*-wave (Fig. 2.8 middle, blue line) and the density (Fig. 2.8 right, black line) is shown in addition. The *P*-wave and *S*-wave times were picked by BLM GmbH Gommern, few outliers of the logging were removed subsequently. Zerbe (2007) remarks that in areas with clearly enlarged calliper *S*-wave travel times are missing, e.g. in Figure 2.8 around 450 m below sea level. The anhydrite layer (K2 reflector) has the highest seismic velocity and density,  $v_p \approx 5500$  m/s,  $v_s \approx 2800$  m/s and  $\rho \approx 2.9$  g/cm<sup>3</sup>. The reservoir zone has a low velocity and density,  $v_p \approx 2800$  m/s,  $v_s \approx 1600$  m/s and  $\rho \approx 2.3$  g/cm<sup>3</sup>.

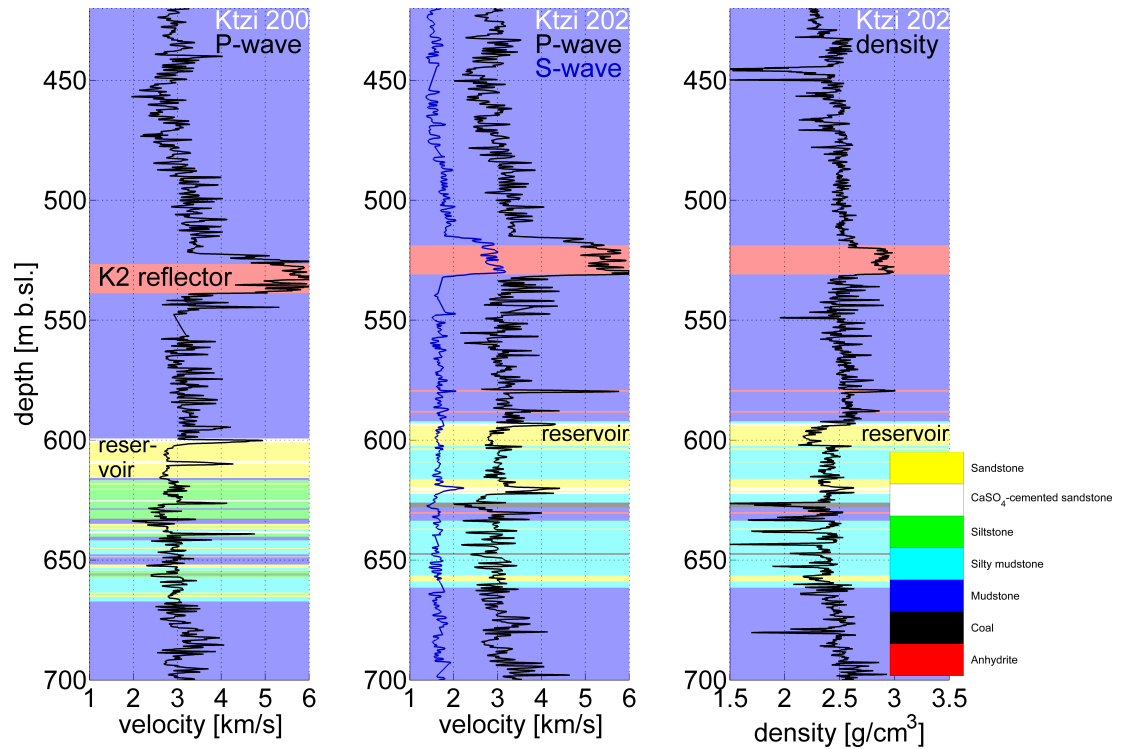


Figure 2.8: Sonic and density logs in the depth level from 420-700 m below sea level [m b.s.l.] together with the lithology within the wells (Norden et al. (2010)). The P-wave sonic log is presented for both observation wells (left and middle, black lines). For Ktzi 202 the S-wave (middle, blue line) and the density (right, black line) are shown in addition.



# 3 Chapter 3

---

## Theoretical Background

*In this chapter, the theoretical background needed for the processing and imaging of crosshole seismic, zero-offset and offset VSP data (Chaps. 4-6) is explained.*

### 3.1 The swept impact seismic technique (SIST)

*The seismic sources used for crosshole seismic and VSP measurements (Chaps. 4-6) are based on the swept impact seismic technique (SIST).*

According to Cosma and Enescu (2001) the swept impact seismic technique (SIST) combines the Vibroseis swept frequency and the Mini-Sosie multi-impact ideas. To reach a resolution in the order of meters, seismic data must contain frequencies in the order of kHz, which are usually associated with low-power sources. Conversely, the sources must deliver sufficient energy to carry the high frequencies through attenuative media over hundreds of meters. "The high-frequency and high-energy requirements can be both fulfilled if the signal energy is built-up in time, rather than being emitted as a short burst" (Cosma and Enescu (2001)). "With SIST, a low-power impact source generates a series of seismic pulses, hence the relation to Mini-Sosie. However, instead of a pseudo-random coding of the impact rates, a deterministic, monotonously varying rate is used, i.e. a swept impact rate, which makes SIST akin to Vibroseis. A SIST coded record  $r_c(t)$  can be written as" (Cosma and Enescu (2001))

$$r_c(t) = \psi(t) \star s(t) \star e(t) + n(t) \quad (3.1)$$

where  $\star$  denotes the convolution operator.  $\psi(t)$  is the controlled impact sequence (inversely linear frequency),  $s(t)$  is the source signature and  $e(t)$  is the earth impulse response. The noise is described by  $n(t)$ . "Following Park et al. (1996), a 'normal' seismic record  $r_d(t)$  can be obtained by cross-correlating the controlled impact sequence  $\psi(t)$  and the coded record  $r_c(t)$ " (Cosma and Enescu (2001))

$$\begin{aligned} r_d(t) &= \psi(t) \otimes r_c(t) \\ &= ACF\{\psi(t)\} \star s(t) \star e(t) + \psi(t) \star n(t). \end{aligned} \quad (3.2)$$

"A key assumption in Equation 3.2 is that the auto-correlation function  $ACF\{\psi(t)\} \approx 0$ , everywhere except at zero-lag. In practice, the degree of compliance with this condition will provide a way to evaluate the performance of various coding schemes. In particular, an inversely linear frequency (linear period) was found to be effective" (Cosma and Enescu (2001)). The linear period sweep leads to a more effective cancellation of the

correlation noise and needs a narrower frequency band. "In principle, the upper limit of the impact frequency band should be as low as possible to reduce the correlation noise. In practice, there are considerable benefits in increasing the impact frequency as much as possible, provided that the quality of the decoded signal does not decrease notably" (Cosma and Enescu (2001)). "As in Equation 3.2  $\psi(t) = 1$  at the moments of impact and  $\psi(t) = 0$  at any other time, the cross-correlation can be replaced by simple "shift-and-stack". For purely random noise, the signal-to-noise ratio (S/N) of the sum signal will decrease by the square root of the number of impacts" (Cosma and Enescu (2001)). However, in Cosma and Enescu (2001) it is shown that not the straight sum is the most efficient way to increase the S/N ratio but, that the median techniques are the best to estimate the source signal.

## 3.2 Principal Component Analysis (PCA)

*The observation wells in Ketzin are slightly deviated (Chap. 2.4.2). To perform a 2D travel time tomography of the crosshole data (Chap. 4), an inclined plane is fitted to the 3D wells using Principal Component Analysis (PCA).*

The PCA is explained according to the internet source Smith (2002). "PCA is mathematically defined as an orthogonal linear transformation that transforms the data to a new coordinate system, such that the greatest variance by any projection of the data comes to lie on the first coordinate (the principal component), the second greatest variance on the second coordinate, and so on" (Wikipedia (2012a)). Once these coordinates are found it is possible to compress the data by reducing the number of dimensions. Here, the data are three dimensional well coordinates (easting ( $x$ ), northing ( $y$ ), depth ( $z$ )).

**(1) Subtract the mean:** In order to produce a data set whose mean is zero, the average across each dimension ( $x$ ,  $y$ ,  $z$ ) is subtracted from that dimension.

**(2) Calculate the covariance matrix:** The covariance is a measure how much the dimensions vary from the mean with respect to each other.

**(3) Calculate the eigenvectors and eigenvalues of the covariance matrix:** The eigenvectors of the covariance matrix are orthogonal, that means the data can be expressed in terms of these orthogonal eigenvectors, instead of expressing them in terms of the  $x$ ,  $y$  and  $z$  axes. The amount by which the original vector was scaled after multiplication by the covariance matrix is the eigenvalue associated with that eigenvector.

**(4) Choosing components and forming a feature vector:** Once the eigenvectors are found from the covariance matrix, the next step is to order them by eigenvalue, highest to lowest. The eigenvector with the highest eigenvalue is the principle component of the data set, because it is the most significant relationship between the data dimensions. Now it is possible to ignore the components of less significance. If some components are left out, the final data set will have lower dimensions than the original. If a plane is fitted to a three dimensional data set, the two components with highest significance are kept, the third component is ignored.

**(5) Deriving the new data set:** The final data set is the original data solely in terms of the chosen vectors. When fitting a 2D imaging plane to 3D deviated wells, the coordinates are changed from being in terms of the axes easting, northing and depth, to being in terms of two eigenvectors.

### 3.3 Tomography with FAST

The travel time tomography of the crosshole data (Chap. 4) is calculated with the first-arrival regularized tomographic method of Zelt and Barton (1998) FAST (First Arrival Seismic Tomography). The open source software can be obtained from the internet source Zelt (2012).

The program run sequence is contained in a shell script file. A starting model and an iterative approach are employed in which new ray paths are calculated for each iteration. The sparse linear system of equations is solved using the LSQR (least squares QR decomposition) variant of the conjugate gradient method (Paige and Saunders (1982)).

**(1) Number of non-linear iterations:** "Travel time inversion is a non-linear problem because the raypaths are dependent on the velocity model. Therefore, a linearised iterative approach is applied using a Taylor series expansion in which a starting model is required and the model and raypaths are updated over a series of iterations" (Zelt et al. (2006)). The first input parameter for the shell script is the maximum number of non-linear iterations, these are iterations in which the model is updated and new raypaths are calculated.

**(2) Forward calculation of travel times and raypaths:** The forward calculation of travel times and raypaths is done with the finite difference eikonal solver of Vidale (1990), with modifications for large velocity gradients by Hole and Zelt (1995). This eikonal solver is part of the FAST software package. "Travel times are calculated progressively away from a source on the sides of an expanding cube, one side being completed before the next is considered" (Zelt and Barton (1998)). Through the iterative calculation of neighbored grid points, the travel time table for the whole area of interest is calculated. The travel time tables used for the Fresnel migration of offset VSP data (Chap. 6) are calculated with this eikonal solver as well.

**(3) The tradeoff parameter  $\lambda$ :** The second input parameter for the shell script is the maximum number of  $\lambda$  values to test for each non-linear iteration. In order to treat the underdetermined part of the solution, FAST uses regularized inversion, in which at each iteration, an objective function, which "measures a combination of the data misfit and constraints of the structure of the model, is minimized in the least square sense" (Zelt et al. (2006), Zelt and Barton (1998)). The objective function  $\phi(\mathbf{s})$  minimized at each iteration can be written as

$$\phi(\mathbf{s}) = \text{data misfit} + \lambda \text{ model structure}, \quad (3.3)$$

where  $\mathbf{s}$  is the model slowness vector. From a free starting value  $\lambda_0$ , the algorithm reduces the trade-off parameter systematically by a chosen factor  $\lambda_r$ . "The systematic reduction of  $\lambda$  stabilizes the inversion by constraining the long-wavelength model structure in the initial iterations and by allowing finer model structure in later iterations" (Zelt et al. (2006)).

The data misfit term is expressed by

$$\text{data misfit} = \delta \mathbf{t}^T \mathbf{C}_d^{-1} \delta \mathbf{t} \quad (3.4)$$

where  $\delta \mathbf{t}$  is the travel time misfit vector and  $\mathbf{C}_d$  is the data covariance matrix. " $\mathbf{C}_d$  is a diagonal matrix with elements  $\sigma_{ii}^2$ , where  $\sigma_{ii}$  is the prior uncertainty of the  $i$ -th travel time" (Zelt and Barton (1998)).

The testing of  $\lambda$  values is stopped if the maximum number of values to test is reached or if a model is found which "predicts the picked travel times within an accuracy consistent

with their assigned uncertainties” (Zelt et al. (2006)). This means the inversion will not attempt to overfit the data for any iteration, but will only iterate towards a model for which the  $\chi^2$  between the observed and predicted data ideally reaches one ( $\chi^2 = 1$ , Zelt et al. (2006)):

$$\chi^2 = \frac{1}{N} \sum_{i=1}^N \left[ \frac{t_i^0 - t_i^p}{\sigma_i} \right]^2, \quad (3.5)$$

where  $N$  is the number of data points,  $t_i^0$  and  $t_i^p$  are the  $i$ -th observed and predicted travel time, and  $\sigma_i$  is the assigned picking uncertainty. The algorithm finds the largest value of the trade-off parameter  $\lambda$  that provides a model with a misfit of one, which yields a model with minimum amount of structure required by the data.

**(4) Model structure constraints:** ”The regularisation is a jumping method in that the constraints are applied to the model perturbation with respect to a background model (usually the starting model)” (Zelt (1998)) . The constraints of the model structure provided by FAST can be written as

$$\begin{aligned} \text{model structure} &= \\ \alpha \text{ model roughness constraint} &+ (1 - \alpha) \text{ smallest perturbation constraint} \end{aligned} \quad (3.6)$$

The parameter  $\alpha$  determines the relative weight of the model roughness (also referred to as model smoothness) and perturbation regularization. The smallest perturbation constraint measures the relative perturbation of the current model from the starting model. Perturbation regularization is not part of the original algorithm (Zelt and Barton (1998)). For the inversion of the crosshole data (Chap. 4.7) a value of  $\alpha = 1$  is used, which means the model roughness is constrained only. ”For ray-based travel time tomography it makes sense to minimize model roughness for several reasons: (1) infinite-frequency ray methods are valid for smooth media only, (2) travel times constrain only the long wavelength model features since the data represent integrals through the model, (3) the linearisation assumption of stationary ray paths is more likely to be satisfied for smooth models, and (4) a consideration of the first Fresnel zone means our recovered model should represent a smoothed version of the true structure” (Zelt and Barton (1998)). The model roughness constraint can be written as

$$\text{model roughness constraint} = \mathbf{s}^T \mathbf{W}_h^T \mathbf{W}_h \mathbf{s} + s_z \mathbf{s}^T \mathbf{W}_v^T \mathbf{W}_v \mathbf{s} \quad (3.7)$$

where  $\mathbf{s}$  is the model slowness vector,  $\mathbf{W}_h$  and  $\mathbf{W}_v$  are the horizontal and vertical roughening matrices, respectively, and  $s_z$  governs the relative importance of maintaining vertical versus horizontal model smoothness. ”The roughness matrices contain the 2D and 1D second spatial derivative finite difference operators that measure the model roughness in the horizontal and vertical directions. Each row of  $\mathbf{W}_h$  contains the five non-zero elements of the Laplacian operator equal to  $1/s_j$ ,  $1/s_j$ ,  $-4/s_j$ ,  $1/s_j$ , and  $1/s_j$ , where the elements correspond to a central cell and the four adjacent cells in the  $x$  and  $y$  directions (in the 3D case) and  $s_j$  is the prior slowness of the centre cell. Similarly, each row of  $\mathbf{W}_v$  has three non-zero elements equal to  $1/s_j$ ,  $-2/s_j$ , and  $1/s_j$ , where the elements correspond to three adjacent cells in the  $z$  direction. The normalization by the prior slowness (division by  $s_j$ ) is applied to avoid a bias toward greater levels of model roughness in regions of high velocity” (Zelt and Barton (1998)).

**(5) Linear system of equations:** The objective function minimized is given by Equations 3.3, 3.4, and 3.7:

$$\phi(\mathbf{s}) = \delta \mathbf{t}^T \mathbf{C}_d^{-1/2} \delta \mathbf{t} + \lambda (\mathbf{s}^T \mathbf{W}_h^T \mathbf{W}_h \mathbf{s} + s_z \mathbf{s}^T \mathbf{W}_v^T \mathbf{W}_v \mathbf{s}) \quad (3.8)$$

and leads to the system of equations (Zelt and Barton (1998))

$$\begin{bmatrix} \mathbf{C}_d^{-1/2} \mathbf{L} \\ \lambda \mathbf{W}_h \\ s_z \lambda \mathbf{W}_v \end{bmatrix} \delta \mathbf{s} = \begin{bmatrix} \mathbf{C}_d^{-1/2} \delta \mathbf{t} \\ -\lambda \mathbf{W}_h \mathbf{s}_0 \\ -s_z \lambda \mathbf{W}_v \mathbf{s}_0 \end{bmatrix} \quad (3.9)$$

where  $\mathbf{L}$  is the partial derivative matrix with elements  $L_{ij} = \partial t_i / \partial s_j$  equal to the length of the  $i$ -th ray in the  $j$ -th cell of the slowness model. The current slowness model is represented by  $\mathbf{s}_0$ ,  $\delta \mathbf{s}$  is the model perturbation, and  $\mathbf{s} = \mathbf{s}_0 + \delta \mathbf{s}$ . "This system is solved using the LSQR variant of the conjugate gradient algorithm" (Zelt and Barton (1998); Paige and Saunders (1982)).

**(6) Evaluation of the quality of the solution:** The root mean square error (rms error) is a measure of the differences between values predicted by a model and the values actually observed (Wikipedia (2012b)). The rms error is calculated by summing the squared difference of the  $i$ -th observed  $t_i^0$  and predicted  $t_i^p$  travel times  $\delta t = t_i^0 - t_i^p$ , dividing the sum through the number of source-receiver pairs  $N$  and calculating the square-root of the quotient:

$$RMS(\delta t) = \sqrt{\frac{\sum_{i=1}^N (t_i^0 - t_i^p)^2}{N}}. \quad (3.10)$$

## 3.4 Band limited impedance inversion

*The seismic impedances of the zero-offset VSP data (Chap. 5) are calculated with the Band Limited IMPedance inversion (BLIMP) method by Ferguson and Margrave (1996).* The BLIMP algorithm is part of a seismic MATLAB package which can be downloaded from CREWES (2012). The sonic and density logs of Ktzi 202 (Chap. 2.4.3) are used to provide the low frequency content required by the inversion process. "The impedance estimate from the well logs is combined in the frequency domain with integrated seismic data. The result is inverse Fourier transformed to provide the final impedance trace. Detailed impedance values are thus provided by the integrated seismic data, and the low-frequency trend is provided by the well-log" (Ferguson and Margrave (1996)).

### 3.4.1 The algorithm

It is assumed that the seismic trace is an estimate of the reflection coefficient series which is given by the true reflection coefficient series convolved with the seismic pulse (Berteussen and Ursin (1983)). The normal incidence reflection coefficient is defined as

$$r_i = \frac{z_{i+1} - z_i}{z_{i+1} + z_i} \quad (3.11)$$

where  $z_i$  is the acoustic impedance, and  $r_i$  is seismic reflectivity. Equation 3.11 is solved for  $z_{i+1}$ , what leads to the relationship between seismic trace and seismic impedance (Ferguson and Margrave (1996))

$$z_{i+1} = z_1 \exp \left( 2 \sum_{k=1}^i r_k \right). \quad (3.12)$$

BLIMP uses Equation 3.12 to invert the seismic trace, it is integrated and subsequently exponentiated to provide the impedance trace. The following is a step by step description

of the BLIMP method, as an example the inversion of the stacked zero-offset VSP baseline is shown (Chap. 5.6).

**Step (1):** The seismic trace is integrated and subsequently exponentiated to provide the impedance trace (Eq. 3.12).

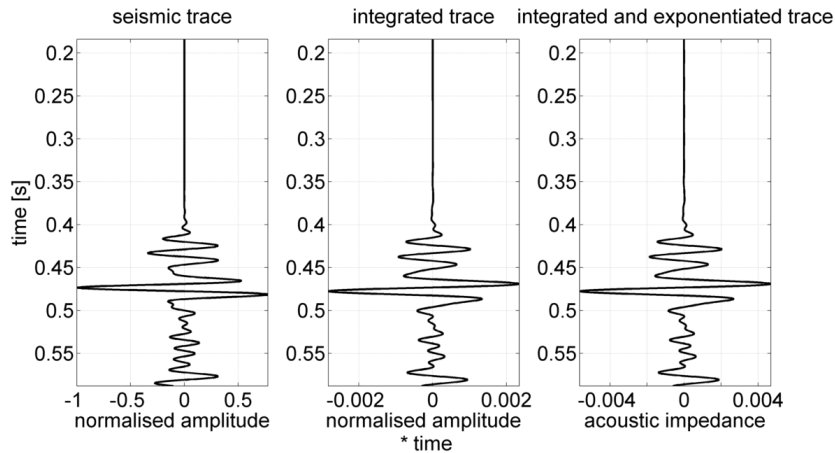


Figure 3.1: BLIMP algorithm step (1): Left: seismic trace, stacked zero-offset VSP baseline. Middle: integrated trace. Right: integrated and exponentiated trace.

**Step (2):** An impedance estimate from the Ktzi 202 sonic and density logs ( $z = \rho \cdot v_p$ ) is obtained, converted from depth to time and tied to the seismic section (Chap. 5.8.1). The linear trend of the impedance log is computed and subtracted. This reduces edge effects during subsequent frequency domain operations (Ferguson and Margrave (1996)).

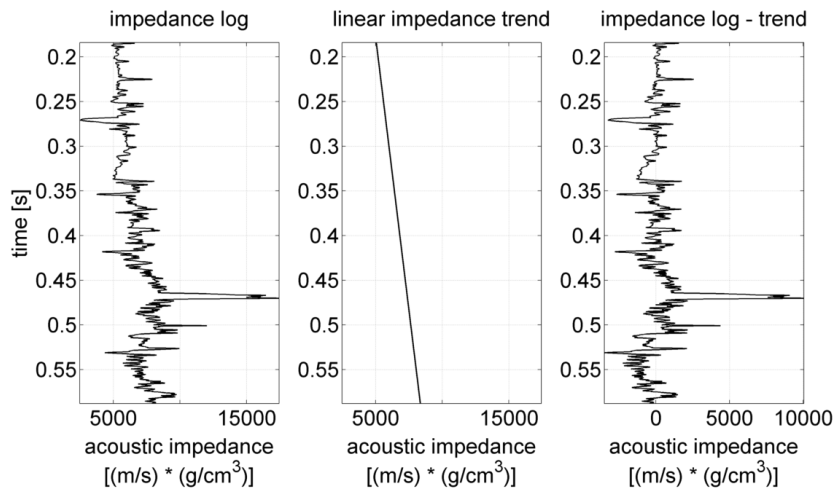


Figure 3.2: BLIMP algorithm step (2): Left: impedance log from Ktzi 202 sonic and density logs in time domain (Chap. 5.8.1). Middle: linear trend of impedance log. Right: impedance log with linear trend subtracted.

**Step (3):** The Fourier spectrum of the impedance log minus its linear trend (step 2) is computed, a low-pass filter is designed and applied to derive the spectrum of the filtered log  $Z_{filteredlog}(\omega)$ . The low-pass is needed to incorporate the low frequencies from the well into the band limited seismic data.

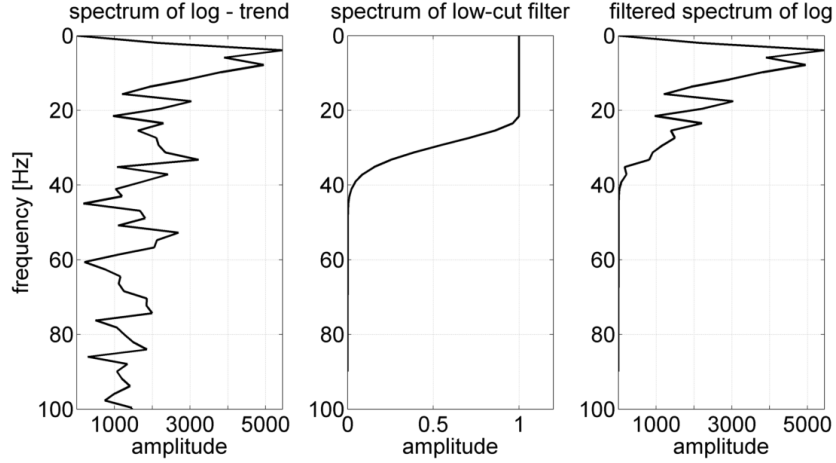


Figure 3.3: BLIMP algorithm step (3): Left: Fourier spectrum of the impedance log minus its linear trend (step 2). Middle: low-pass filter (20 Hz with 10 Hz Gaussian roll-off). Right: filtered spectrum of impedance log.

**Step (4):** The Fourier spectrum of the impedance trace which was obtained from the seismic trace (step 1) is computed ( $Z_{impedance\ trace}(\omega)$ ). The mean power of both spectra (low-pass filtered impedance log (step 3) and impedance trace) is matched by a scalar  $\beta$  and combined to form the spectrum of the output impedance  $Z(\omega)$ .

$$Z(\omega) = Z_{filtered\ log}(\omega) + \beta \cdot Z_{impedance\ trace}(\omega) \quad (3.13)$$

The scalar  $\beta$  is found by a least squares algorithm which minimizes the squared error computed with

$$error = \sum_i (Z(\omega_i) - Z_{filtered\ log}(\omega_i))^2 \quad (3.14)$$

Thus, the final impedance  $Z(\omega)$  has its high frequencies from the seismic trace  $Z_{impedance\ trace}(\omega)$  but the spectral combination is constrained to match the impedance log  $Z_{filtered\ log}(\omega)$  as closely as possible. So the impedance log needs to be broadband even though only its low frequencies are used.

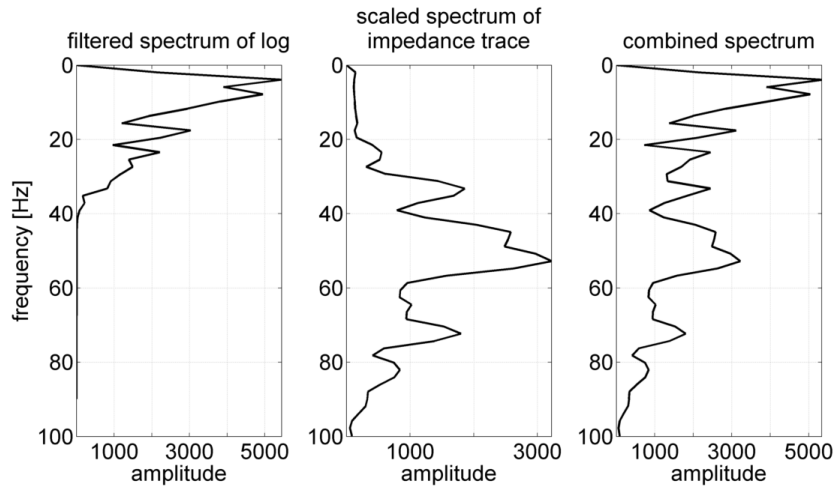


Figure 3.4: BLIMP algorithm step (4): Left: filtered spectrum of impedance log (step 3). Middle: spectrum of impedance trace (obtained from the seismic trace, step 1), scaled to the mean power of both spectra (low-pass filtered impedance log and impedance trace). Right: combination of both spectra (Eq. 3.13).

**Step (5):** An inverse Fourier transformation is applied to the combined spectrum (Eq. 3.13) and the low-frequency trend (step 2) is added.

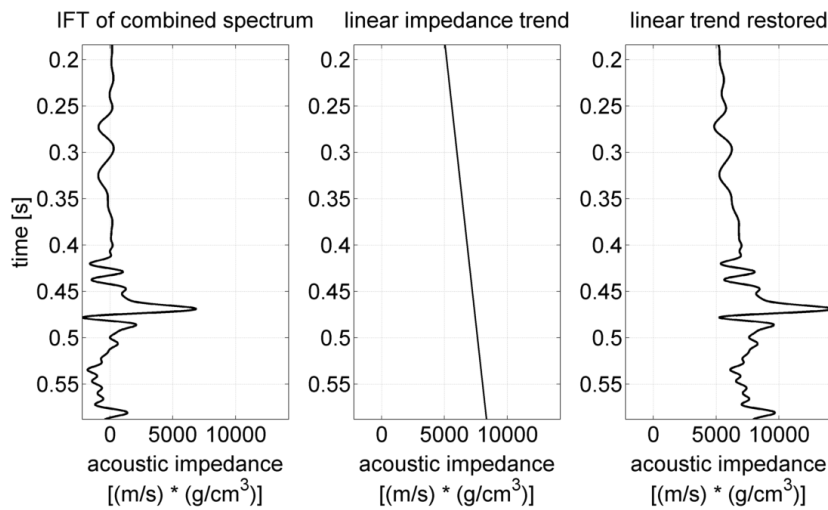


Figure 3.5: BLIMP algorithm step (5): Left: inverse Fourier transformation of combined spectrum (Eq. 3.13). Middle: linear trend of impedance estimate (step 2). Right: final result of the band limited impedance inversion.

### 3.4.2 Conversion of the acoustic impedance to P-wave velocity

The acoustic impedances (Chap. 3.4.1) are converted to P-wave velocities in order to derive the velocity change due to CO<sub>2</sub> injection within the reservoir.

The acoustic impedance  $z$  is defined as

$$z = \rho \cdot v_p \quad (3.15)$$

where  $\rho$  is the density and  $v_p$  the P-wave velocity. Gardner et al. (1974) give a velocity-density relation, "which is approximately correct for brine-saturated sedimentary rocks,

over a wide range of basins, geologic ages, and depths” (Becquey et al. (1979)). If the velocity  $v_p$  is expressed in [m/s], this relationship is

$$\rho = 0.31 \cdot v_p^{0.25} \quad (3.16)$$

where  $\rho$  is the density in [g/cm<sup>3</sup>]. The relationship between velocity  $v_p$  and acoustic impedance  $z$  is given by the combination of Equations 3.15 and 3.16:

$$v_p = \sqrt[1.25]{\frac{z}{0.31}} \quad (3.17)$$

where the acoustic impedance  $z$  is in  $(m/s) \cdot (g/cm^3)$ .

### 3.5 Fresnel zone based sensitivity kernels

*Fresnel zone based sensitivity kernels are used to derive the width and shape of the Fresnel zone, when migrating offset VSP data (Chap. 6.6).*

Fresnel zone based sensitivity kernels have been developed to overcome resolution limitations of tomography experiments based on the asymptotic high-frequency solution of the wave equation (ray theory). ”The fat ray constructed on the basis of the wave equation is the sensitivity kernel, also called the Fréchet kernel. It reflects the sensitivity of the recorded seismic signals including amplitude and travel time to the perturbation of the media (Liu et al. (2009))”.

According to Jensen et al. (2000), ”the first Fresnel zone is that part of the refracting medium through which energy is transmitted from the source to the receiver within less than a quarter of a period of the ray arrival; thus this energy interferes more or less constructively. For a single-frequency sensitivity kernel the Fresnel zone contains regions of alternating positive and negative sensitivity. The odd zones are all regions from which waves are scattered such as to interfere constructively at the receiver, whereas the even Fresnel zones are regions where the scattered waves interfere destructively. For sensitivity kernels for a multi-frequency wave field the negative and positive Fresnel zones tend to cancel except for the first Fresnel zone, and therefore the Fréchet kernel is almost confined to the first Fresnel zone” (Jensen et al. (2000)). ”The region with the highest sensitivity corresponds to the first Fresnel volume, through which the main energy of the wave travels to the receiver around the geometric ray” (Liu et al. (2009)), therefore the sensitivity kernel can be used to monitor the properties of the Fresnel zone (Jensen et al. (2000); Spetzler and Snieder (2004)).

The sensitivity kernels used for the migration of offset VSP data are based on the work of Jensen et al. (2000). To find the first Fresnel zone, the delay time  $\Delta t(\mathbf{x})$  between the first arrival and the arrival of waves that have been scattered at  $\mathbf{x}$  is calculated. The delay time is given as

$$\Delta t(\mathbf{x}) = t(s, \mathbf{x}) + t(\mathbf{x}, r) - t_0(s, r). \quad (3.18)$$

Here  $t(s, \mathbf{x})$  and  $t(\mathbf{x}, r)$  are the travel time from source ( $s$ ) to  $\mathbf{x}$  and from  $\mathbf{x}$  to the receiver ( $r$ ) and  $t_0(s, r)$  is the travel time along the ray path from source to receiver. A point  $\mathbf{x}$  is defined to be in the first Fresnel zone, if the corresponding travel times satisfy the equation

$$|\Delta t(\mathbf{x})| < T/4 \quad (3.19)$$

where  $T$  is the dominant period of the wave. As an approximate Fréchet kernel delimited by the first Fresnel zone Jensen et al. (2000) use the following sensitivity function:

$$S(\mathbf{x}) = \cos\left(\frac{2\pi\Delta t(\mathbf{x})}{T}\right) \cdot \exp\left[-\left(\frac{\alpha\Delta t(\mathbf{x})}{T/4}\right)^2\right]. \quad (3.20)$$

Here  $S(\mathbf{x})$  is the sensitivity at  $\mathbf{x}$ . "The cosine factor models the alternating sensitivity being positive in the odd Fresnel zones and negative in the even Fresnel zones. The  $\alpha$  value in the Gaussian controls the degree of cancellation in Fresnel zones beyond the first" (Jensen et al. (2000)).

# 4

## Chapter 4

---

# Crosshole: baseline, 1st and 2nd repeat

*This chapter is about the baseline, 1st and 2nd repeat of the crosshole seismic measurements in Ketzin. The main focus of the chapter is the travel time tomography of measured and simulated data.*

### 4.1 Motivation and research objectives

The crosshole seismic measurement was designed to follow the migration of CO<sub>2</sub> at small scale during the injection. "As CO<sub>2</sub> replaces saline water in saturated reservoir sandstones a P-wave velocity reduction may occur. This velocity change can potentially be used to monitor CO<sub>2</sub> in sandstone aquifers using seismic tomography" (Zhang et al. (2012)).

Prior to injection the crosshole seismic baseline was measured. Injection started on 30 June 2008 and the CO<sub>2</sub> needed 15 days to migrate 50 m from the injection well Ktzi 201 to the observation well Ktzi 200 (Fig. 2.4, Chap. 1). Since an equally fast propagation was expected towards Ktzi 202, two repeat measurements were scheduled shortly after the first breakthrough (Chap. 1.3.1), in order to monitor the migration of the CO<sub>2</sub> between the observation wells. But since the CO<sub>2</sub> needed 263 days to reach Ktzi 202, only a small amount of CO<sub>2</sub> had migrated into the imaging plane during the 1st and 2nd repeat. Hence, the time-lapse observations did not observe significant travel time changes due to CO<sub>2</sub> saturation in the Stuttgart Formation (Lüth et al. (2011)).

Even though, no significant time-lapse effects were observed in the measured data, travel time tomography is tested on synthetic data having the same geometry as the real data. The results of the modelling study can be generalised for the interpretation of time-lapse crosshole experiments investigating the migration of CO<sub>2</sub> in a water saturated sandstone. The velocity model for this study is based on the results of travel time tomography of baseline and repeat measurements.

### 4.2 Equipment and recording parameters

*The crosshole seismic was measured between the observation wells Ktzi 200 and Ktzi 202 (Fig. 2.4). Recording and pre-processing, which involves the SIST processing (shift-and-stack, Chap. 3.1) and tube wave removal was done by Vibrometric Oy, Finland.*

**Lubricator, access to pressurised wells:** Since the 1st and 2nd repeat measurements were performed after the breakthrough of CO<sub>2</sub> in Ktzi 200, a lubricator (Fig. 4.1) is needed to access the pressurised well with the borehole source. The lubricator was operated by Atlas G.I.P. A lubricator is a large pipe construction which is installed vertically onto the pressurized borehole. In the upper part of the pipe construction the high pressure grease injector and suitable seal elements are installed. First, the borehole source is inserted into the lubricator which is not yet pressurised. The cable of the borehole is led out at the top through the high pressure grease injector and the seal elements. In order to be able to lower the source into the well, the valves between the lubricator and the well are opened. The interior of the lubricator, inside which the source is placed, now has the same pressure as the borehole, and the source can be lowered into the well. The seal elements together with the high pressure grease injector prevent the pressurized CO<sub>2</sub> inside the lubricator to pass through the cable outlet into the atmosphere. In order to retrieve the source from the well, it is pulled up with the borehole cable into the pipe construction of the lubricator, the valves between well and lubricator are closed and the excess pressure in the lubricator is being discharged (Geo Sys - Umwelttechnik und Geogeräte GmbH Leipzig (2012)).



Figure 4.1: A lubricator on top of the receiver well Ktzi 202 (photo: R. Giese).

**Borehole source VIBSIST SPH 64:** The borehole source VIBSIST SPH 64 is a piezoelectric actuator (Fig. 4.2) working according to the swept impact seismic technique (SIST), which is explained in Chapter 3.1. The seismic signals are produced as rapid series of several hundred high voltage pulses, maintaining a monotonic variation of the impact rate to achieve a non-repeatable sequence. The seismograms are obtained by cross-correlating the swept impact sequence with a pilot signal recorded at the source.

The low power of the individual pulses maintains a relatively high signal frequency content, while the energy is built up by using a long actuation time (20-30 s) for each record (Cosma and Enescu (2001)). "The seismic actuator is set into motion by applying high voltage (6000 V) to a stack of piezoelectric crystals in the borehole source" (?). The measurement device VIBSIST SPH 64 is composed of three modules, which are linked by a steel armoured cable. These modules are (1) the electric power supply outside of the well, (2) the generator and the piezoelectric actuator, both within the well, with acoustic impedance converter and (3) the motor-driven wedge clamping mechanism (? , Fig. 4.2).

Energy output per impact	4 - 8 J
Impact repetition rate	2 - 70 ms
Impact frequency	35 - 3500 Hz
Sweep time adjustment	2 - 70 s



Figure 4.2: The VIBSIST SPH 64 borehole source. Top: Specifications (Zhang et al. (2012)). Bottom: motor-driven sliding wedge clamping mechanism (photos: ?).

**Borehole receiver TC 12 chain:** The crosshole seismic is recorded with the 12-level chain TC 12 with water coupled piezoelectric transducer modules (hydrophones, Fig. 4.3).

Frequency range 10 Hz - 20 kHz
Sensitivity -160 dB re 1 V/1 $\mu$ Pa
Horizontal directivity (radial x-y plane) $\pm 3$ dB at 10 kHz ( $0^\circ$ - $360^\circ$ )



Figure 4.3: The TC 12 borehole receiver. Top left: Specifications (Zhang et al. (2012)). Bottom left: Piezoelectric transducer (hydrophone). Right: receiver chain with 12 hydrophone modules (photos: R. Giese).

**Recording parameters:** During each measurement (baseline, 1st and 2nd repeat), 9129 traces with a sample rate of 0.05 ms and a length of 204.75 ms have been recorded. This leads to 4096 samples per trace and a sample frequency of 20 kHz. The Nyquist frequency is  $f_{Ny} = \frac{1}{2}f_{sample} = 10$  kHz.

### 4.3 Source - receiver configuration

The crosshole seismic was measured between the two observation wells over a distance of 100 m (Fig. 2.4). The source was activated in Ktzi 200 at 289 depth levels (1 m spacing), the traces were recorded in Ktzi 202 at 261 depth levels (1 m spacing). The depth interval of the measurement was 452 - 740 m below ground level (or 418 - 706 m below sea level [m b.sl.], Tab. 2.1). In Figure 4.4 (left image), the precise depth intervals of sources and receivers are indicated by the thick lines.

A dense pattern of 9129 rays crossing the imaging plane in many directions is recorded in the form of common source gathers. The hydrophone chain, consisting of 12 receiver levels at 1 m vertical distance (Chap. 4.2), is lowered to the first measurement depth. The source is activated at several depths (1 m vertical distance) and simultaneously recorded with 12 hydrophones. Since a receiver spreading larger than 12 m is desired,

the hydrophone chain is dropped to the next depth interval, and prior source positions are repeated. This leads to gathers of 9, 12, 24, 36 or 48 receivers per source point. As an example, two source gathers located at 466.4 m and 476.4 m b.sl. are shown in the left image of Figure 4.4 in red and blue.

The source-receiver configuration of the crosshole measurement is shown in Figure 4.4, right image. The red line marks the source gather at 466.4 m b.sl. (Figure 4.4, left, red gather) which is recorded with receivers from 454.8-489.8 m b.sl.. This source belongs to layout number 7 (the grey scale indicates the layout number). Within one layout, all source positions recorded with the same receiver configuration are summarised. The deepest source belonging to layout number 7 (likewise recorded from 454.8-489.8 m b.sl.) is marked by the blue line and corresponds to the source gather at 476.4 m below sea level (Figure 4.4, left, blue gather).

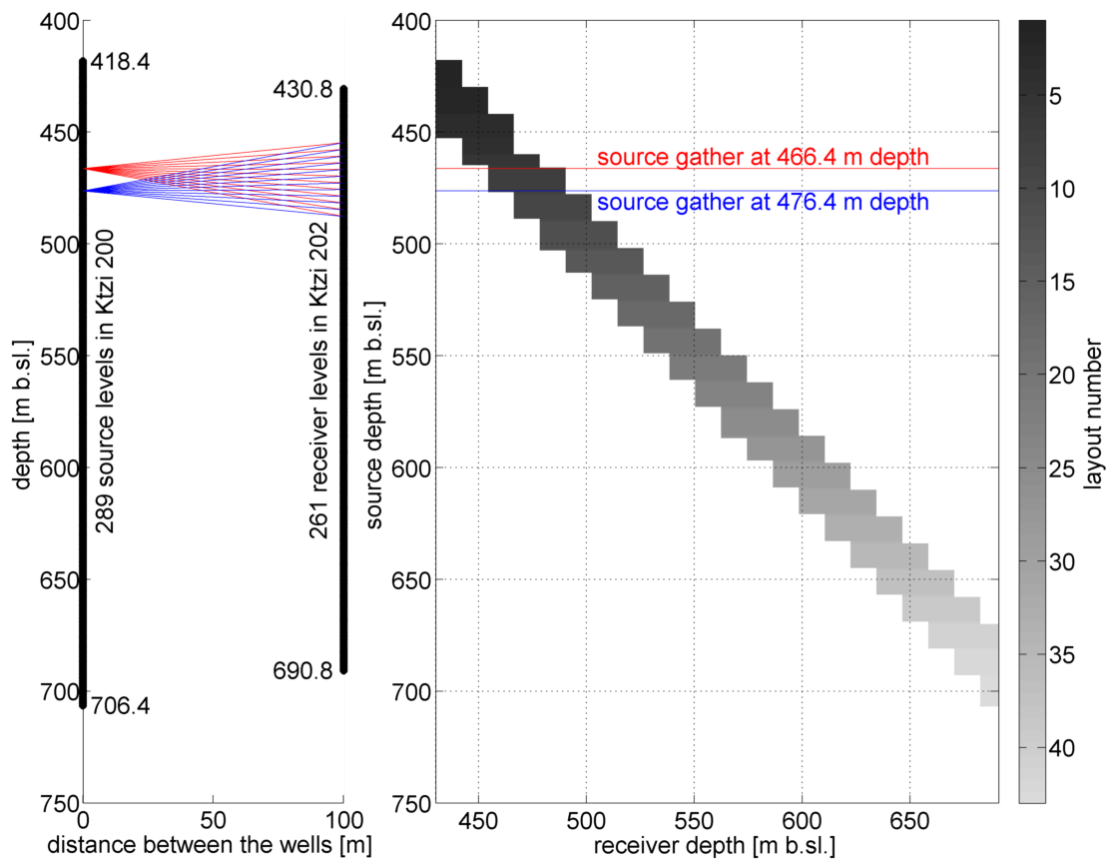


Figure 4.4: Crosshole measurement geometry (left image) and source-receiver configuration (right image). Left: the depth range of the source levels in Ktzi 200 is 418-706 m below sea level [m b.sl.]. The depth range of the receiver levels in Ktzi 202 is 431-691 m b.sl.. As an example, two source gathers of sources located at 466.4 m b.sl. (red) and 676.4 m b.sl. (blue) are shown. Right: The grey scale indicates the layout number. For instance layout number 7 (between the red and blue lines) represents sources from 466.4-476.4 m b.sl., which are recorded with the receivers from 454.8-489.9 m b.sl..

## 4.4 Data sets

To analyse the time-lapse frequency content (Chap. 4.5) and to pick the first breaks (Chap. 4.6) two different processed data sets are used (the processing was done by Vibrometric Oy, Finland).

(1) **Within the K2 reflector** (see Fig. 2.2 for the lithology) raw data with a high frequency content and strong tube waves (Figs. 4.5 and 4.6) were used. Figure 4.5 shows baseline raw data in the depth range of the K2 as a common source gather (top) and as a common receiver gather (bottom). The first breaks recorded close to the K2 are not direct waves, but refracted waves from this very fast ( $>5500$  m/s, Fig. 2.8 sonic logs) anhydrite layer. Within the common receiver gather, strong tube waves are visible. Figure 4.6 shows the same common source gather as in Figure 4.5, but for the 1st repeat and 2nd repeat (top and bottom, respectively). Within the K2 the first breaks of baseline, 1st and 2nd repeat show excellent repeatability.

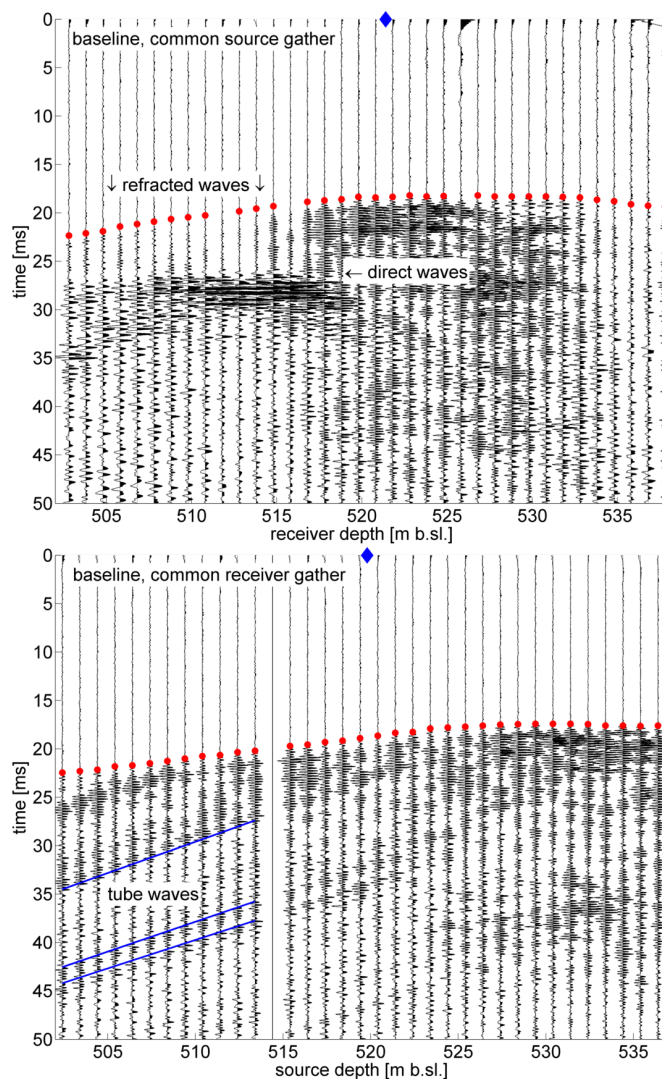


Figure 4.5: Baseline raw data within the K2 as a common source gather (top) and as a common receiver gather (bottom). The blue diamonds mark the position of the common source and common receiver, respectively. The red dots mark the picked first break travel times (Chap. 4.6). The depth is in meter below sea level [m b.sl.].

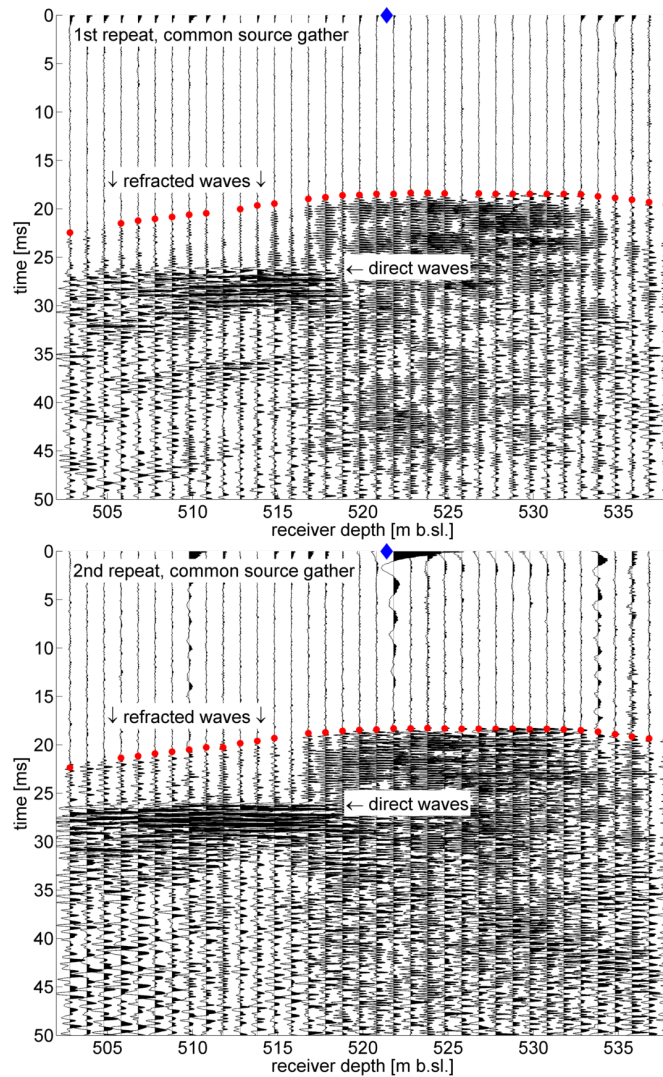


Figure 4.6: Common source gathers of raw data within the K2 of 1st repeat (top) and 2nd repeat (bottom). The blue diamonds mark the position of the common source. The red dots mark the picked first break travel times (Chap. 4.6). The depth is in meter below sea level [m b.sl.].

(2) **Within the reservoir** a data set with tube waves removed and the frequency filtered to the maximum reservoir frequency of  $\sim 2000$  Hz (Chap. 4.5) was used. Figure 4.7 shows tube wave filtered data of the reservoir as common source gathers for baseline (top), 1st repeat (middle) and 2nd repeat (bottom). Within the reservoir, a low velocity “shadow” zone ( $< 2800$  m/s, Fig. 2.8 sonic logs) the signal to noise ratio is low, what leads to a greater uncertainty when picking the first breaks. However, some features, marked with blue circles in Figure 4.7, are reproduced in each of the measurements.

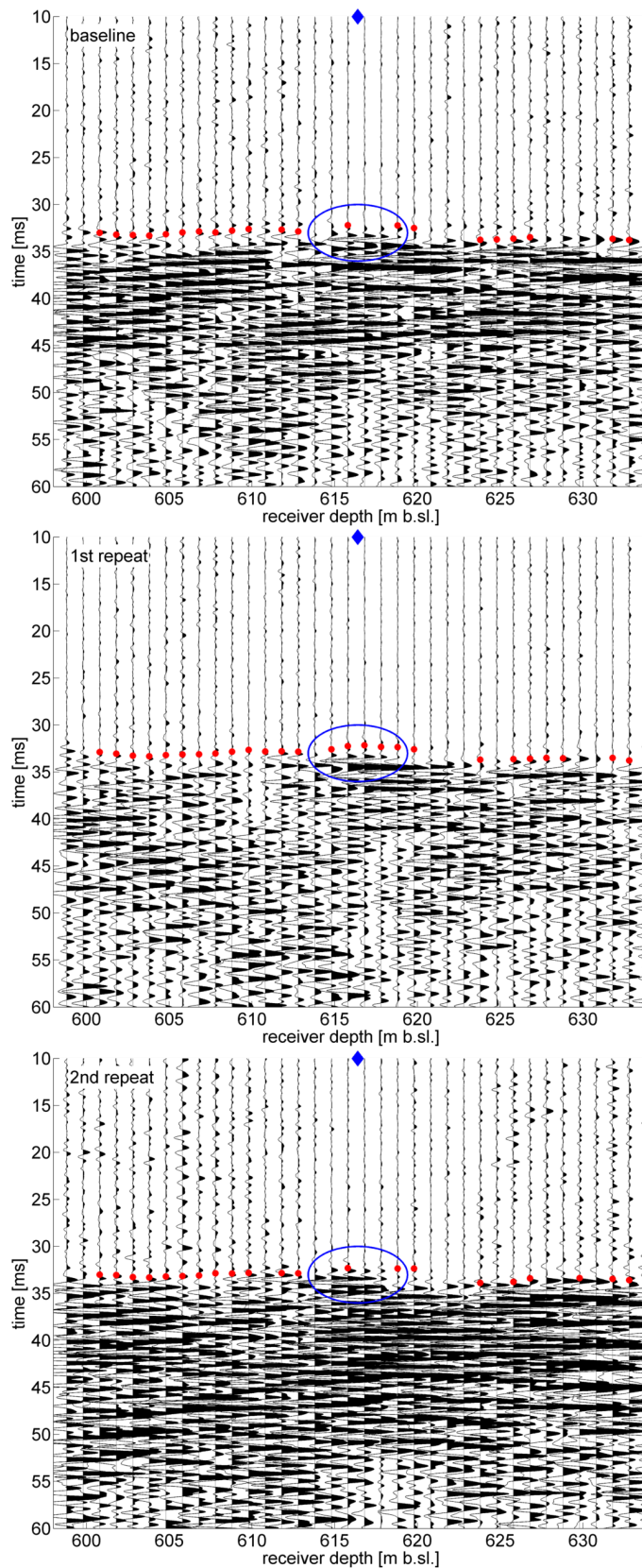


Figure 4.7: Tube wave filtered data within the reservoir as common source gathers for baseline (top), 1st repeat (middle) and 2nd repeat (bottom). The blue diamonds mark the position of the common source. The blue circles mark a feature which is reproduced in each of the measurements. The red dots mark the picked first break travel times (Chap. 4.6). The depth is in meter below sea level [m b.sl.].

## 4.5 Frequency content

Figure 4.8 shows selected amplitude spectra of the crosshole baseline, 1st and 2nd repeat. The left column shows spectra of common source gathers, the right column shows spectra of common receiver gathers. Three depth ranges of the crosshole measurements are selected: The top row shows spectra of sources and receivers in the depth range of the K2, the middle row is an example for the reservoir and the bottom row shows spectra from below the reservoir (see Fig. 2.2 for the lithology). The spectra within the reservoir are calculated for those source gathers which show a travel time delay when modelling CO<sub>2</sub> injection (Chap. 4.8). The frequency content is calculated in a time window of  $\sim 20$  ms centred around the picked first break times (Chap. 4.6). Within the anhydrite layer of the K2, frequencies up to 4250 Hz have been recorded. The maximum frequency within the sandstone units of the reservoir (and below) is 2000 Hz. Due to the small amount of CO<sub>2</sub> that had migrated into the imaging plane during the 1st and 2nd repeat, no significant frequency changes within the reservoir are observed.

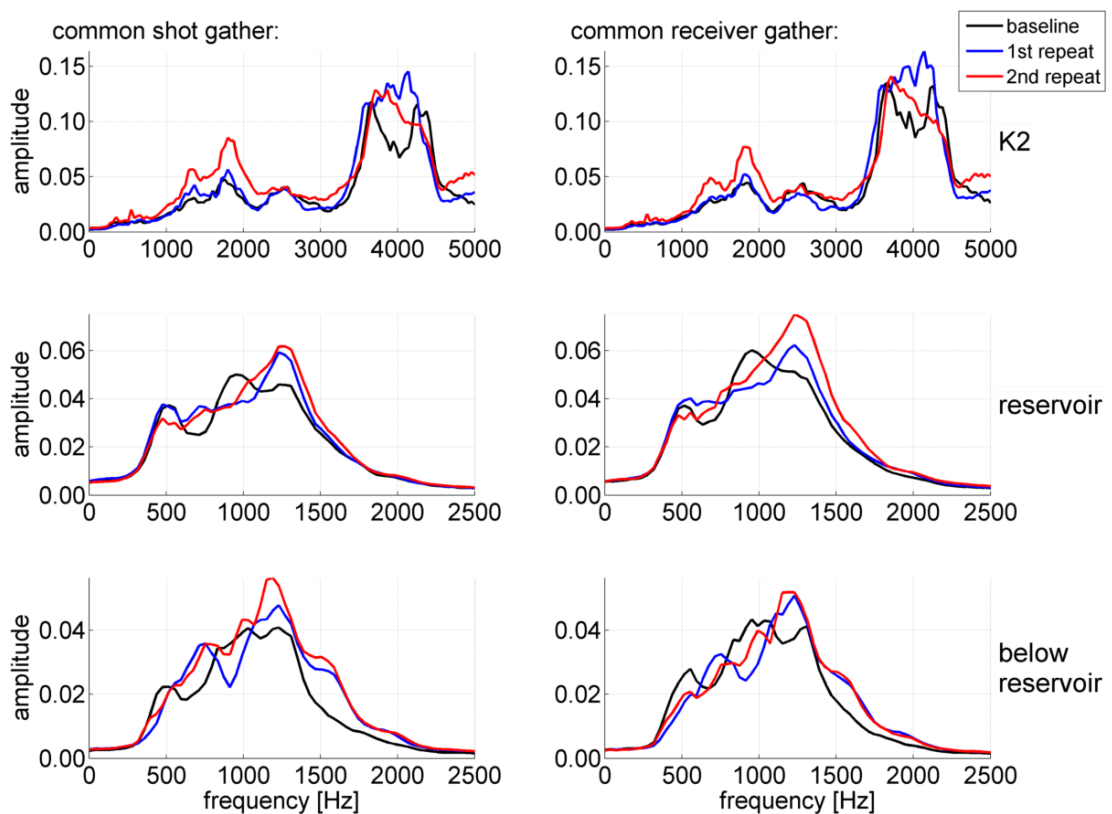


Figure 4.8: Amplitude spectra of the crosshole baseline, 1st and 2nd repeat. The left column shows spectra of common source gathers, the right column shows spectra of common receiver gathers. Three depth ranges of the crosshole measurements are selected: The top row shows spectra of sources and receivers in the depth range of the K2, the middle row is an example for the reservoir and the bottom row shows spectra from below the reservoir. The baseline is plotted in black, the 1st repeat in blue and the 2nd repeat in red.

## 4.6 Picking the first breaks

The first breaks are picked on the tube wave filtered data, except in the depth range of the K2, where raw data are used. The picking is done in common source gathers and common receiver gathers. Based on the assumption that the time-lapse observations (1st and 2nd repeat) did not observe significant travel time changes due to CO<sub>2</sub> saturation in the Stuttgart Formation (Chaps. 1.3.1 and 1.3.2), differences in picked travel times are attributed to picking errors within zones of high noise level, or to the sources/hydrophones not being located at identical depths during the different surveys (Zhang et al. (2012)). High noise levels can be caused by bad or different hydrophone coupling conditions between surveys or by a lower ray coverage within low velocity zones (Chap. 4.7.2, Fig. 4.14).

Due to the low signal-to-noise ratio, especially within the reservoir (Fig. 4.7), it is difficult to pick a consistent phase in all three data sets, for which reason only those travel times were used as an input for the tomography, which match in all of the measurements (baseline, 1st repeat and 2nd repeat) to an accuracy of 0.25 ms. This accuracy represents one period of the highest expected frequency (4000 Hz, Chap. 4.5). Within the desired accuracy of 0.25 ms, 6610 (72 %) travel times could be picked for the baseline, 6684 (73 %) for the 1st and 6628 (73 %) for the 2nd repeat (number of possible travel times: 9129). Examples of the travel times used for tomography can be found in the Figures 4.5 - 4.7 marked as red dots. Figure. 4.9 shows a compilation of the baseline travel times used for tomography. The velocity model in the background is the result of the baseline tomography (Chap. 4.7). The observation wells Ktzi 200 and Ktzi 202 are indicated by black lines. The lowest travel time (17.15 ms) is associated with the fast anhydrite layer, whereas the highest travel time (34.78 ms) is measured within the slow reservoir zone.

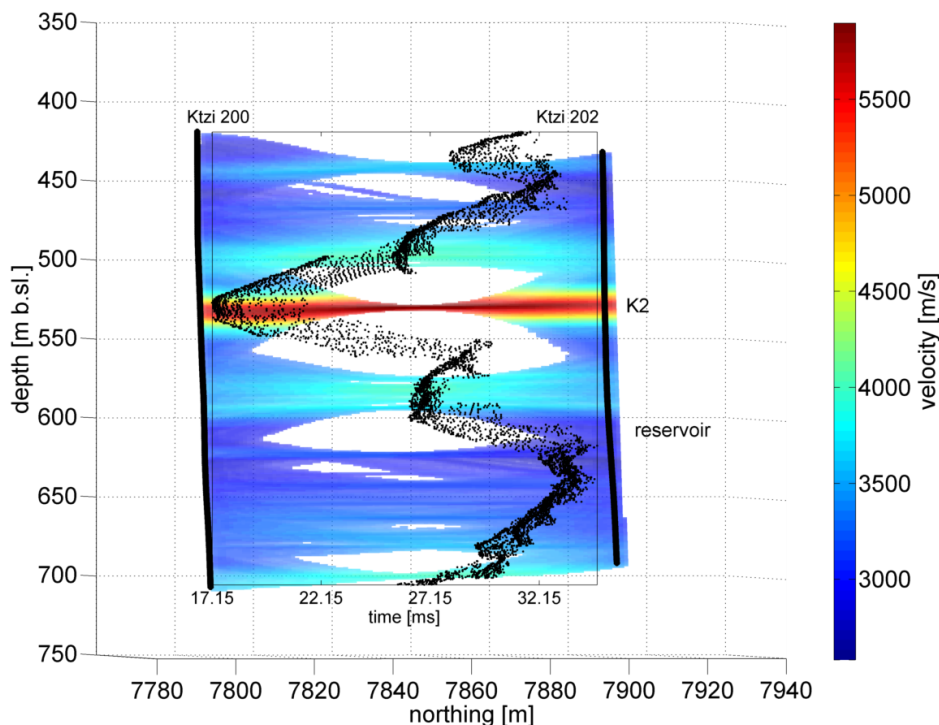


Figure 4.9: Baseline travel times used for tomography. The velocity model in the background is the result of the baseline tomography (Chap. 4.7). The depth is in meter below sea level [m b.sl.].

## 4.7 Travel time tomography

### 4.7.1 FAST: Input parameters and mode of operation

*The travel time tomography of the crosshole, calculated with the open source software FAST (First Arrival Seismic Tomography) by Colin Zelt (Zelt and Barton (1998)), is explained following the outline in Chapter 3.3 (Tomography with FAST).*

”The free-parameter values were varied to facilitate a systematic exploration of the model space to determine the simplest and most geologically reasonable model that fits the data” (Zelt et al. (2006)). The program run sequence is contained in a shell script file, which calls various executables.

#### **Number of non-linear iterations:**

The tomography is calculated with 4 non-linear iterations.

#### **Forward calculation of travel times and raypaths:**

*1D starting velocity model:* Since sonic logs are available for both observation wells (Chap. 2.4.3, Fig. 2.8), the 1D starting velocity model is derived from these sonic logs. To generate a smoother log as an input for the tomography a moving average over 50 values, sampled in 1 m depth intervals, is calculated for both sonic logs (Fig. 4.10, left and middle). These smoothed sonic logs are again averaged to derive the 1D starting velocity model (Fig. 4.10, right). This velocity model is written to an input file that is read by FAST when setting up the model for inversion.

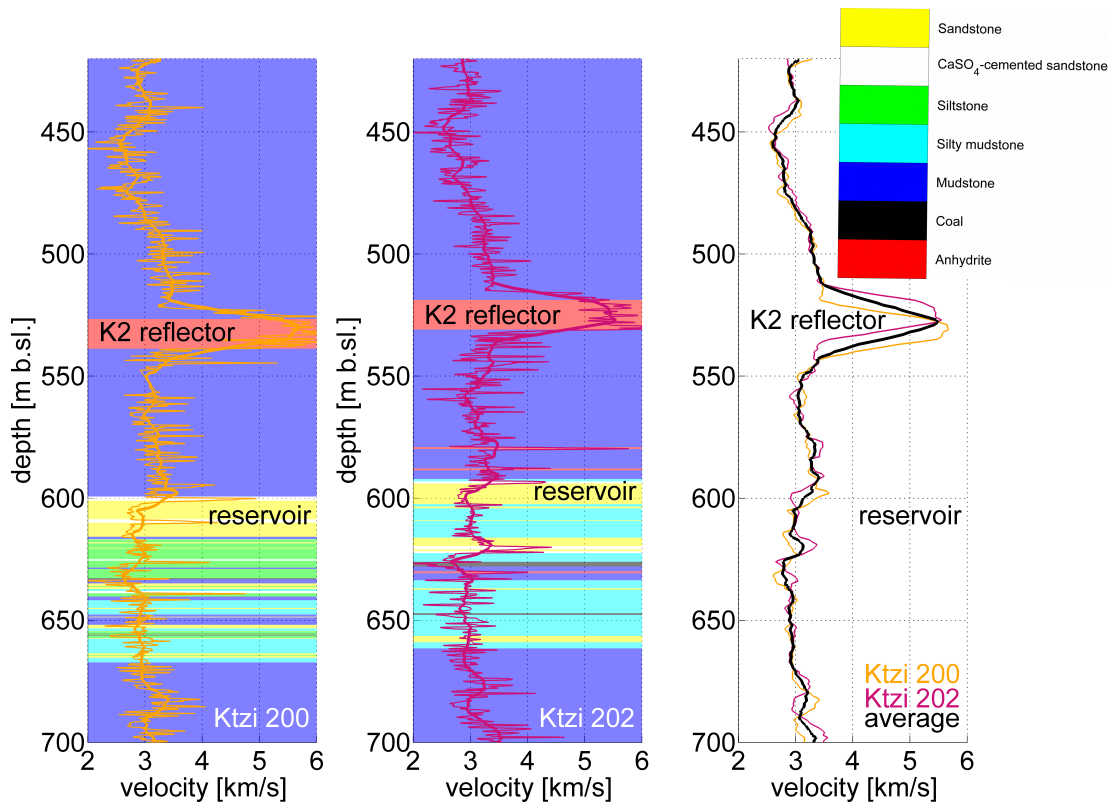


Figure 4.10: Development of the starting velocity model for travel time tomography. Left (Ktzi 200) and centre (Ktzi 202): sonic log raw data (thin lines) and moving average (thick lines) over 50 values, sampled in 1 m depth intervals. Right: Starting velocity model (1D) for the tomography with FAST: Orange and magenta lines: moving average of sonic logs (see left and middle figure). Black line: 1D starting model, average velocity between Ktzi 200 and Ktzi 202. The depth is in meter below sea level [m b.sl.].

*Input of source - receiver coordinates, model size, cell size of the forward grid, travel times and uncertainty of travel times:* The deviated observation wells (Chap. 2.4.2) "result in a 3D problem, so the well deviation cannot be fully accounted for in 2D tomography" (Moret et al. (2006)). The deviated well coordinates are fitted with an inclined plane in 3D space by principal component analysis (PCA, Chap. 3.2). Figure 4.11 shows the 2D tomography plane fitted to the 3D wells in UTM coordinates, the velocity model is the result of the inversion of the baseline travel times (the same as in Fig. 4.9). The PCA transformed source and receiver coordinates, the picked travel times and the uncertainty of the travel times are written to input files for FAST. The uncertainty of each travel time is set to 0.25 ms, since only picks which match at least to this accuracy are used (Chap. 4.6). Additional input files control the size of the model and the grid point distance. The model has the dimension 0-135 m in horizontal direction and 0-325 m in vertical direction. The forward grid is set to a cell size of 1 m.

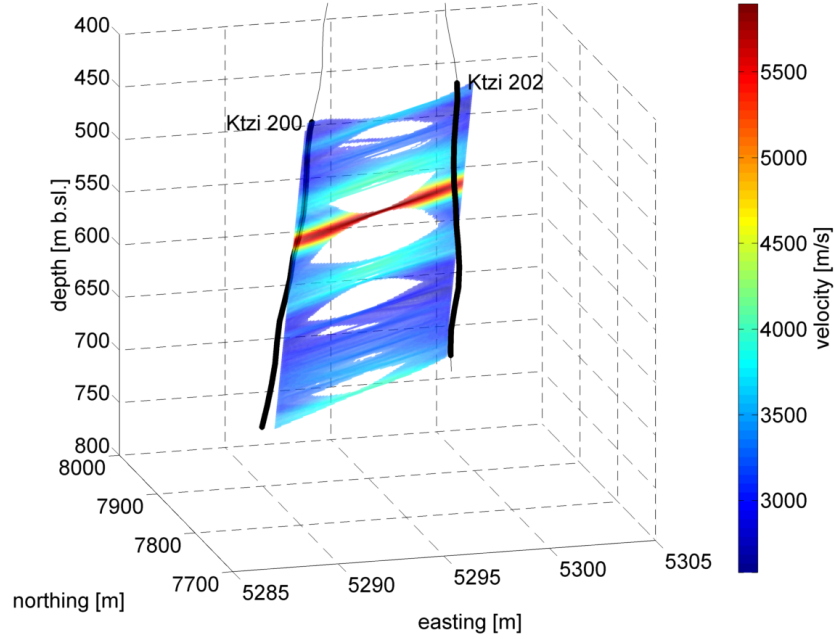


Figure 4.11: 2D tomography plane fitted to the 3D wells in UTM coordinates. The black lines show the deviated wells Ktzi 200 and Ktzi 202 in absolute coordinates (Chap. 2.4.2). The 2D tomography plane fitted to the 3D wells is shown, the velocity model is the result of the inversion of the baseline travel times (the same as in Figure 4.9).

### The trade-off parameter $\lambda$ :

The goal of the inversion is to find a minimum structure model that satisfies the chosen normalized  $\chi^2$  test (Eq. 3.5). That means the model includes only structure required to fit the data according to the noise level.

For the non-linear iterations 1-3 the inverse grid is set to cell size of 5 m. The  $\chi^2$  values of the starting model for baseline, 1st and 2nd repeat are 132.3, 129.8 and 134.7, respectively. The starting value of the trade-off parameter is  $\lambda_0 = 1000$ , the algorithm reduces the trade-off parameter systematically by a chosen factor of  $\lambda_r = 1.414214 = \sqrt{2}$ . The number of  $\lambda$  values to test for each iteration is set to 10. Figure 4.12 shows the evolution of the trade-off parameter during the 4 non-linear iterations and the resulting  $\chi^2$  values. Within the first non-linear iteration (Fig. 4.12, top left) the  $\lambda$  value is reduced from 1000 to 44.2, the best model is found for the 10th test. The 10th model is selected for the 2nd non-linear iteration (Fig. 4.12, top right), which starts with a  $\lambda$  value of 44.2. Here the best model is found for the 5th test ( $\lambda = 11$ ). A further reduction of the  $\lambda$  value leads to an increase of the  $\chi^2$  and the test is stopped. The starting value ( $\lambda = 11$ ) of the 3rd non-linear iteration (Fig. 4.12, bottom left) leads to  $\chi^2 < 1$ , therefore the trade-off parameter is increased and a bisection procedure begins until the largest value of the trade-off parameter  $\lambda$  is found with a misfit close to one (Zelt (1998)).

After the 3rd non-linear iteration the best models are selected (Fig. 4.12, bottom left), which are model 4 for the baseline and 1st repeat and model 3 for the 2nd repeat. The  $\chi^2$  for baseline, 1st and 2nd repeat fit the data according to the noise level with values of 1.0028, 1.0059 and 1.0084, respectively. Based on these models the 4th non-linear iteration is calculated with a refined inverse grid of 1 m cell size. In order to find the smoothest model for this finer grid the lambda value is again increased to the starting value  $\lambda_0 = 1000$ , which leads to a  $\chi^2$  close to one for the first test of  $\lambda$  (Fig. 4.12, bottom

right). The final  $\chi^2$  for baseline, 1st and 2nd repeat are 1.0017, 1.0048 and 1.0073, respectively.

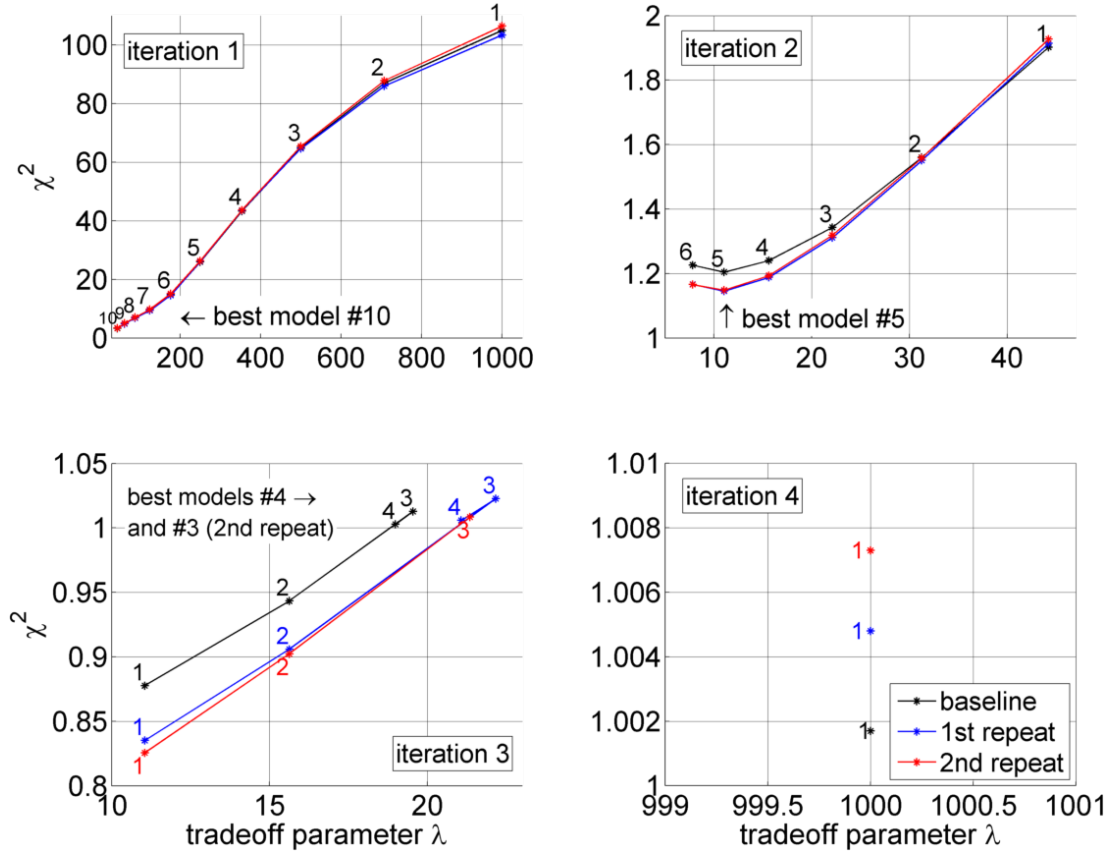


Figure 4.12: Evolution of the trade-off parameter  $\lambda$  during the 4 non-linear iterations, from top left to bottom right, and the resulting  $\chi^2$  values. The different colours represent the inversion of baseline (black), 1st repeat (blue) and 2nd repeat (red). The numbers next to the data points count the  $n$ -th test of the  $\lambda$  value. The best model of the corresponding non-linear iteration is marked.

**The model structure constraints:**

Since the model roughness is constraint only ( $\alpha = 1$ ), only the value of  $s_z$ , which governs the relative importance of maintaining vertical versus horizontal model smoothness, has to be set. A value of 0 would eliminate any constraint on vertical smoothness (Eq. 3.7), the chosen value  $s_z = 0.125$  adds some smoothness in the vertical direction.

**Evaluation of the quality of the solution:**

To evaluate the quality of the solution the root mean square error (rms-error) is calculated (Eq. 3.10). Figure 4.13 shows the travel time residuals for the starting model (black) and the final models after 4 iterations (red) as a function of the receiver depth, for baseline, 1st and 2nd repeat (from top to bottom). The rms travel time misfit for the starting model is 2.88 ms ( $\chi^2 = 132.3$ ), 2.85 ms ( $\chi^2 = 129.8$ ) and 2.90 ms ( $\chi^2 = 134.7$ ) for baseline, 1st and 2nd repeat. The rms travel time misfit of the final models after 4 iterations is 0.2502 ms ( $\chi^2 = 1.0017$ ), 0.2506 ms ( $\chi^2 = 1.0048$ ) and 0.2509 ms ( $\chi^2 = 1.0073$ ) for baseline, 1st and 2nd repeat.

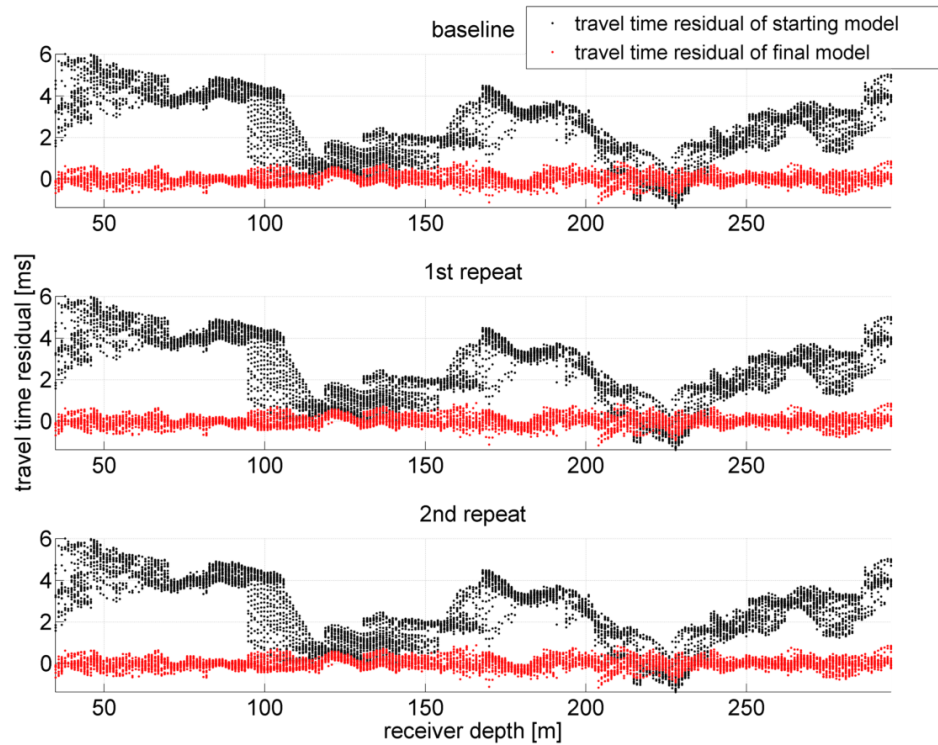


Figure 4.13: Travel time residuals for the starting model (black) and the final models after 4 iterations (red) as a function of the receiver depth, for baseline, 1st and 2nd repeat (from top to bottom).

#### 4.7.2 Results of the travel time tomography

The data sets used for the tomography are the picked travel times for baseline, 1st and 2nd repeat (Chap. 4.6). All data sets are inverted on the same 1D velocity model derived from the sonic logs (Chap. 4.7.1). After inversion, differences of inversion results are calculated (Fig. 4.15).

Figure 4.14 shows the result of the baseline tomography in UTM coordinates overlaid by the calculated rays. The rays are bent into seismically fast layers (like the K2, Chap. 2.4.3), what leads to large differences in the ray coverage. The ray coverage ranges from 0 rays per cell (e.g. within the low velocity parts of the reservoir), to 845 rays per cell (within the K2). For a better overview the results are presented as 2D planes with relative coordinates, shaded according to the ray coverage in the following.

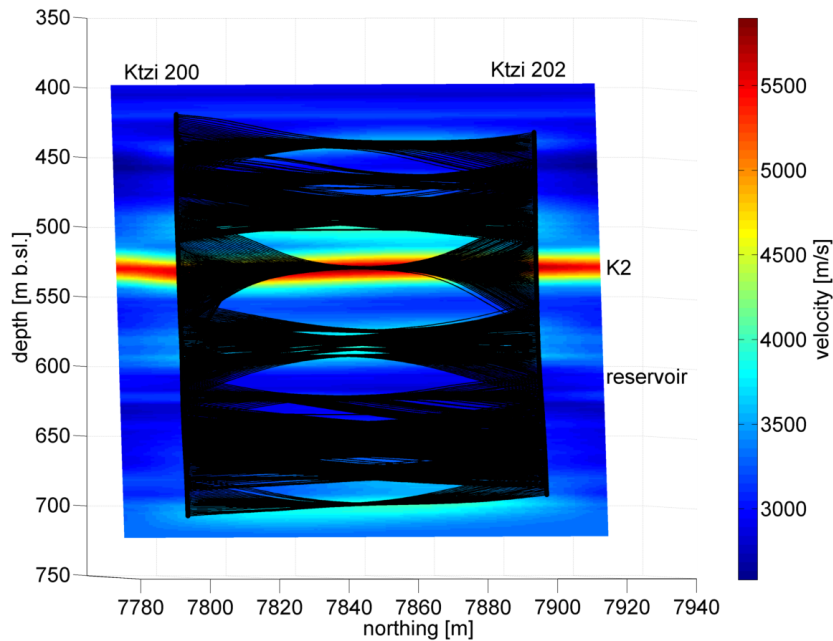


Figure 4.14: Result of the baseline tomography overlaid by the calculated rays. The rays are bent into seismically fast layers (like the K2, Chap. 2.4.3), what leads to large differences in the ray coverage. The ray coverage ranges from 0 rays per cell, e.g. within the low velocity parts of the reservoir (Chap. 2.4.3), to 845 rays per cell, within the K2.

Figure 4.15 shows the tomography results of baseline, 1st repeat and 2nd repeat (top row, from left to right), and the differences between 1st repeat and baseline, 2nd repeat and baseline and 2nd repeat and 1st repeat (bottom row, from left to right). There are no significant differences between the baseline and the two repeats in the depth range of the reservoir at about 205-215 m relative depth (Fig. 4.15, red lines, Lüth et al. (2011), Zhang et al. (2012)). The main velocity difference with a magnitude of  $\pm 90$  m/s at 130-140 m relative depth (Fig. 4.15) is associated with the anhydrite layer. These changes were also observed by Zhang et al. (2012) with a magnitude of  $\Delta v = \pm 1000$  m/s and cannot be due to the injection of  $\text{CO}_2$ . These changes are attributed to inversion artefacts caused by (1) differences in picked travel times (limited to 0.25 ms) and (2) varying source-receiver pairs used for the inversion (Chap. 4.6). These differences between the data sets are illustrated in the Figures 4.5 and 4.6, where used traces (= picked source-receiver pairs) are marked with red dots. Given the high velocity of the anhydrite layer, small differences can result in significant differences in the inverted velocity fields. The tomography of modelled traces (Chap. 4.8), whose travel times and locations match perfectly in areas not influenced by  $\text{CO}_2$  injection, show no artefacts (Fig. 4.19).

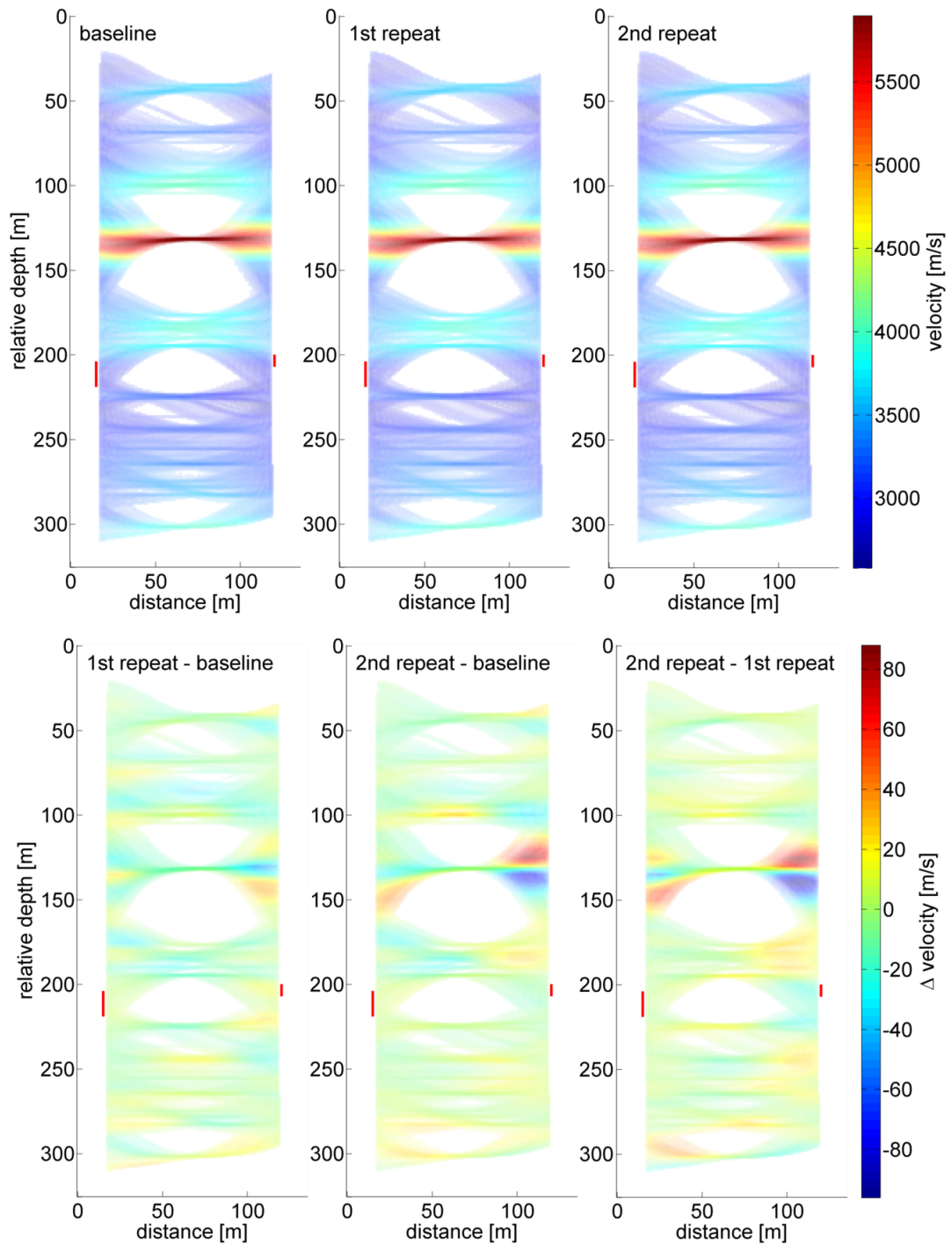


Figure 4.15: Tomography results of baseline, 1st repeat and 2nd repeat (top row, from left to right), and the differences between 1st repeat and baseline, 2nd repeat and baseline and 2nd repeat and 1st repeat (bottom row, from left to right). The red lines below 200 m depth mark the depth range of the reservoir in Ktzi 200 and Ktzi 202. The results are shaded according to the ray coverage.

Figure 4.16 shows the velocity derived by travel time tomography as an average of baseline, 1st and 2nd repeat together with the lithology (Fig. 2.2). The reservoir sandstone is marked with a star. The average of all three measurements is a reliable

representation of the velocity models derived by crosshole travel time tomography. The average model is used for the forward calculation of travel times (Chap. 4.8). The K2 layer, as dominant seismic reflector, is well resolved in thickness and its P-wave velocity of  $\sim 5500$  m/s is in agreement with the sonic logs (Chap. 2.4.3). The distinction of other layers or vertical structures is not possible. Low velocity zones are characterized through poor or no ray coverage.

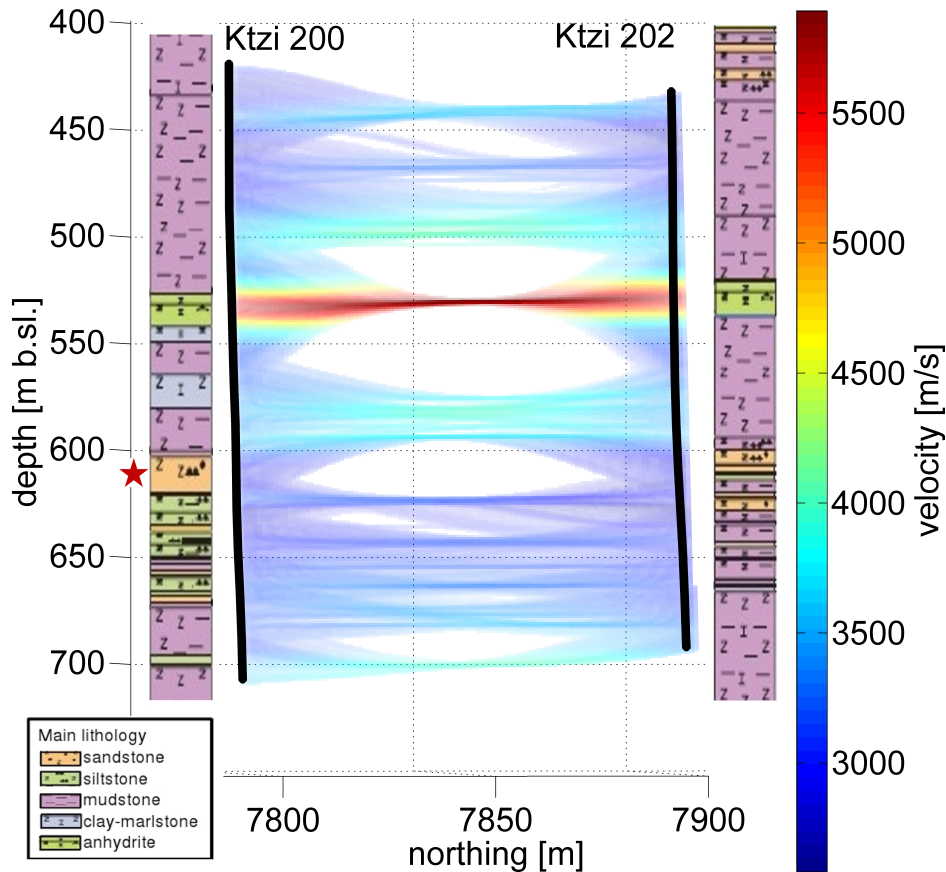


Figure 4.16: The velocity derived by travel time tomography as an average of baseline, 1st and 2nd repeat together with the lithology (Fig. 2.2). The reservoir sandstone is marked with a star. The depth is in meter below sea level [m b.sl.].

In order to compare the tomography (Fig. 4.16) with the sonic logs of Ktzi 200 and Ktzi 202, two 1D velocity - depth functions are derived from the average velocity model: The first function is the mean velocity calculated horizontally across the 'left side' (0 - 67.5 m) of the model. This 1D velocity profile is plotted with red dots on the left side of Figure 4.17. On the right side in Figure 4.17 the red dots represent the second function, the mean velocity calculated horizontally across the 'right side' (67.5 - 135 m) of the model. The size of the red dots is an indication of the ray coverage, where large dots correspond to a high ray coverage. Both 1D velocity - depth functions are shown with the corresponding sonic log and lithology of Ktzi 200 and Ktzi 202. The comparison between the sonic log velocities and the travel time tomography (Fig. 4.17) show a comparable fit with the sonic logs, the main trends of velocity change with depth are mapped. The more horizontal velocities, as determined from the tomography, are  $\sim 200$  m/s faster than the vertical sonic log velocities. This effect was observed by Zhang et al. (2012) as well.

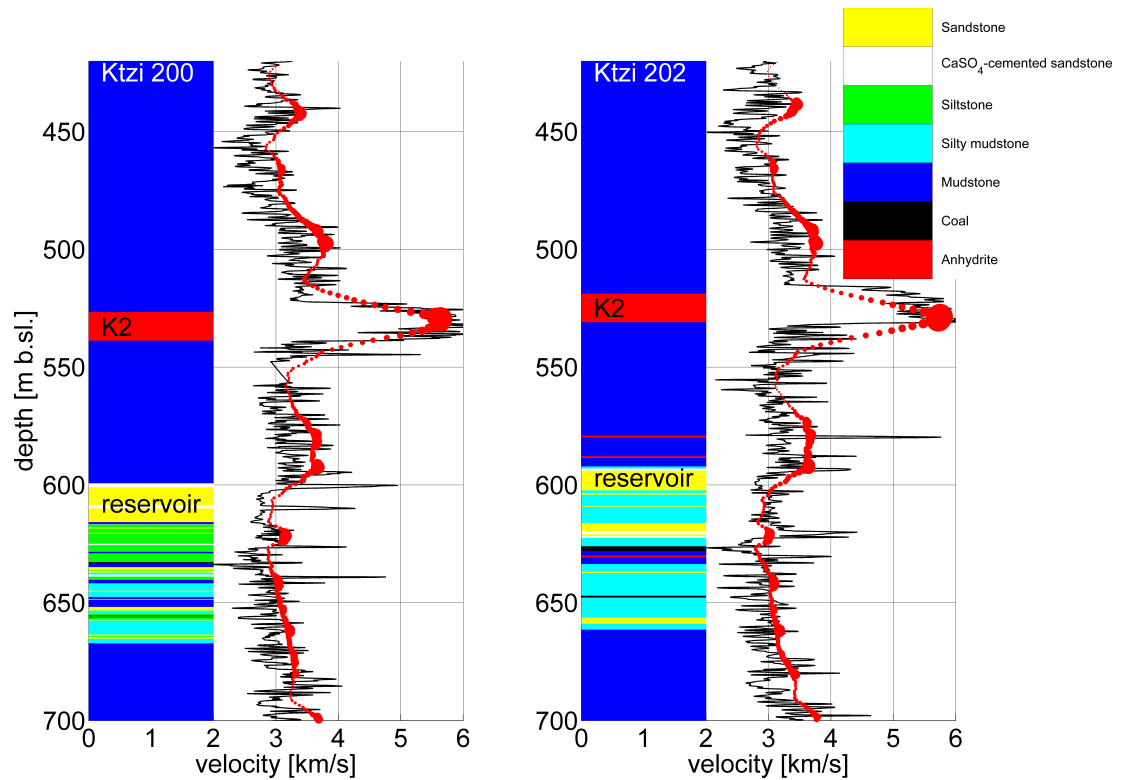


Figure 4.17: 1D velocity - depth functions derived from the average tomography velocity model (Fig. 4.16). The 1D velocity - depth functions (red dots) are compared with the sonic logs (black lines) for Ktzi 200 (left) and Ktzi 202 (right). The 1D velocity is calculated as horizontal mean across the “left side” (0 - 67.5 m, Ktzi 200) and the “right side” (67.5 - 135 m, Ktzi 202) of the average velocity model. The size of the red circles is an indication of the ray coverage, where large dots correspond to a high ray coverage. The depth is in meter below sea level [m b.s.l.]. For both wells the lithology is shown (Chap. 2.4.3).

## 4.8 Simulated CO<sub>2</sub> injection: Forward calculation and tomography of travel times

The synthetic baseline travel times are calculated on the average velocity model of baseline, 1st and 2nd repeat (Chap. 4.7.2, Fig. 4.16). The CO<sub>2</sub> injection is simulated by decreasing the velocity of the model in the depth range of the reservoir by 10%. As the CO<sub>2</sub> extends into the formation, the thickness of the CO<sub>2</sub> layer is reduced (Lengler et al. (2010)). Reducing the velocity by 10% is within the expected range of the velocity reduction due to CO<sub>2</sub> injection: Kummerow and Spangenberg (2011) (Chap. 2.3.3) found a decrease of the P-wave velocity from 3200 m/s to 2700 m/s with decreasing the brine saturation from 100% to 45% (Fig. 2.5). A velocity reduction by 10% would correspond to a brine saturation of ~70%.

Two different scenarios are investigated: (1) The CO<sub>2</sub> has reached Ktzi 202 within the upper reservoir compartment (Fig. 4.19, top row left) and (2) the CO<sub>2</sub> migrated only half the distance between the observation wells (Fig. 4.19, bottom row left).

The source and receiver positions used for the forward calculation equal the 6610 traces picked for the baseline measurements (Chap. 4.6), in order to make the measured and

modelled tomography results comparable. As for the tomography of the measured data, the picking uncertainty is set to 0.25 ms (Chap. 4.6). Figure 4.18 shows an example of the forward calculated travel times within the K2 (top) and within the reservoir (bottom) as common source gathers of the baseline data. The blue dots mark the modelled baseline travel times. The red dots are the result of the travel time calculation based on model (1), where the CO<sub>2</sub> has reached Ktzi 202 within the upper compartment. For model number (1) the maximum observed travel times change is 1.089 ms (this shot gather is shown in Fig. 4.18, bottom), the mean observed travel time change is 0.360 ms. For model number (2) the maximum observed travel times change is 0.798 ms, the mean observed travel time change is 0.263 ms.

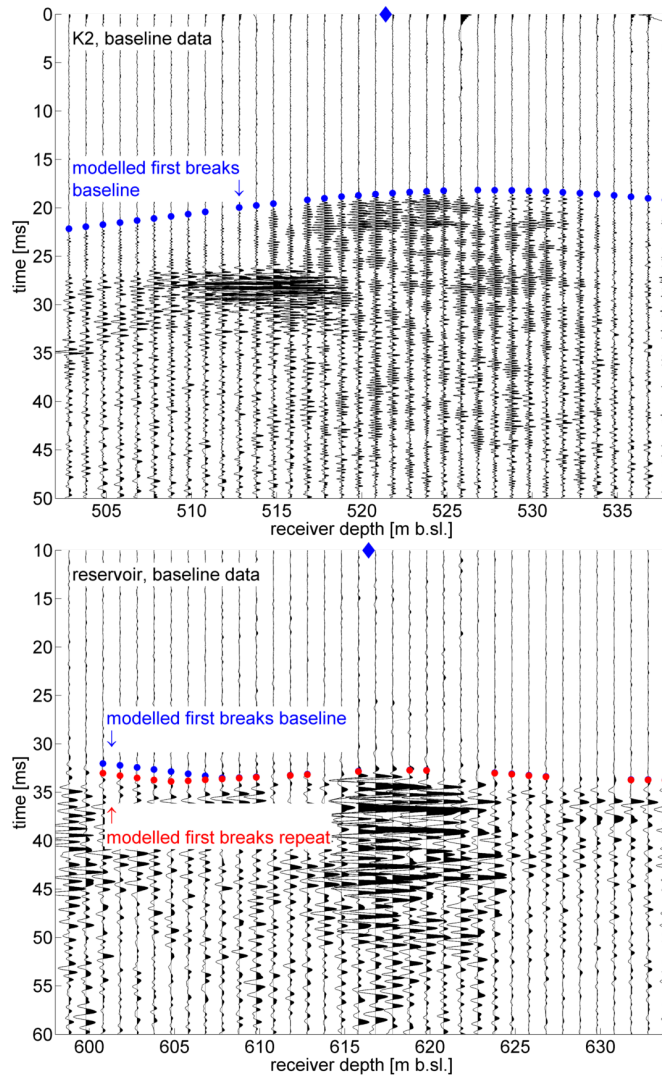


Figure 4.18: Example of the forward calculated travel times within the K2 (top) and within the reservoir (bottom) plotted as dots on common source gathers of the measured baseline data. The blue dots mark the synthetic baseline travel times. The red dots are the result of the travel time calculation based on model (1) where the CO<sub>2</sub> has reached Ktzi 202 within the upper compartment. The depth is in meter below sea level [m b.sl.], the blue diamonds mark the position of the common source.

The inversion of the forward modelled travel times is done with the same 1D starting

velocity model and the same inversion parameters as used for the measured data (Chap. 4.7). Figure 4.19 summarizes the results of the travel time tomography based on synthetic travel times: The left column shows the velocity difference between the forward models and the baseline model (Fig. 4.16). The middle column shows the velocity difference after the inversion and the right column shows the velocity difference in percent of the baseline velocity.

**(1) Shape of velocity anomaly:** The velocity change follows the input anomaly as a rough estimate of the location of the changes in the reservoir caused by the injection of CO<sub>2</sub>. Inherent layering or thinning of the input anomaly is not resolved. The main CO<sub>2</sub> anomaly after inversion of model (1) is more elongated than that of model (2). The main anomaly of model (2) is concentrated within the left half of the model but is smeared out beyond the range of the input model.

**(2) Amplitude of velocity anomaly:** The input velocity was reduced by 10% within the reservoir, after forward calculation and inversion the final maximum velocity reduction in the reservoir was 2.44% for model (1) and 1.85% for model (2).

The underestimation of the anomaly is linked to an overestimation of the observed travel time, since the fastest rays are those that circumvent the low velocity zone. This leads to an overestimation of the velocity and therefore to an underestimation of the amplitude of velocity anomalies in an inversion problem. For media with structures a size smaller than the Fresnel volume, this effect is intensified by the forward calculation of travel times based on the standard ray theory, which is derived using a high-frequency approximation (Musil et al. (2003), Spetzler et al. (2008)). Using an average frequency of  $f = 1000$  Hz (Chap. 4.5) and a velocity  $v_p = 2800$  m/s (Chap. 2.4.3) within the reservoir, the wavelength is  $\lambda = v_p/f = 2.8$  m. This leads to an average width of the first Fresnel zone  $L_F$  of 11.8 m in 50 m distance and of 16.7 m in 100 m distance ( $L_F = \sqrt{\lambda \cdot \text{raypath length}}$ ). The expected time-lapse structure as shown in Figure 4.19 is smaller in size than the average Fresnel volume.

At the Nagaoka CO<sub>2</sub> injection site, sonic logging indicated a sound speed reduction of 21% due to CO<sub>2</sub> injection. An inversion of crosshole data with 3D finite-frequency wavefield theory found a velocity decrease of 18%, whereas the inversion with standard ray theory observed only a velocity change in the order of 3% (Spetzler et al. (2008)).

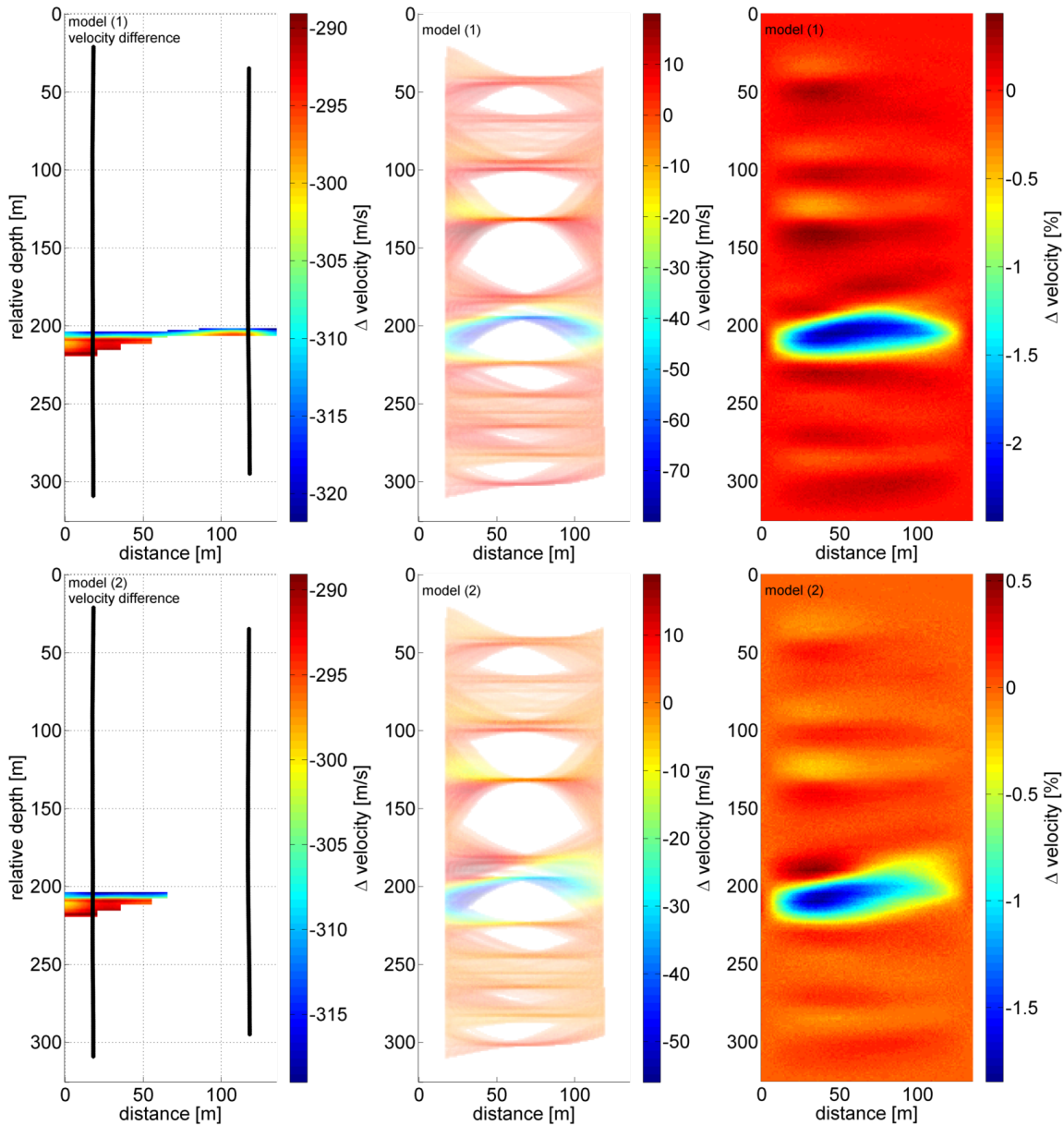


Figure 4.19: Results of the travel time tomography based on modelled travel times. The left column shows the velocity difference between the forward models and the baseline model (Fig. 4.16). The middle column shows the velocity difference after the inversion and the right column shows the velocity difference in percent of the baseline velocity.

## 4.9 Conclusions

- Time-lapse seismic tomography of baseline, 1st repeat and 2nd repeat (Fig. 4.15) show no significant velocity differences in the depth range of the reservoir (Lüth et al. (2011), Zhang et al. (2012)). The main velocity difference with a magnitude of  $\pm 90$  m/s is associated with the anhydrite layer. These changes were also observed by Zhang et al. (2012) and cannot be due to the injection of  $\text{CO}_2$ . These changes are attributed to inversion artefacts caused by (1) differences in picked

travel times and (2) varying source-receiver pairs used for the inversion. Given the high velocity of the anhydrite layer, small differences can result in significant differences in the inverted velocity fields. The tomography of modelled traces, whose travel times and locations match perfectly in areas not influenced by CO<sub>2</sub> injection, show no artefacts (Fig. 4.19).

- An average velocity model of baseline, 1st and 2nd repeat is calculated. It is a reliable representation of the velocity models derived by crosshole travel time tomography (Fig. 4.16). The K2 layer, as dominant seismic reflector, is well resolved in thickness and its P-wave velocity of  $\sim 5500$  m/s is in agreement with the sonic logs. The distinction of other layers or vertical structures is not possible. The rays are bent into seismically fast layers (like the K2), what leads to large differences in the ray coverage. Low velocity zones are characterised through poor or no ray coverage. The average model is used for the forward calculation of travel times.
- In order to compare the crosshole seismic tomography result (Fig. 4.16) with the sonic logs of Ktzi 200 and Ktzi 202, 1D velocity-depth functions are derived from the average velocity model. The comparison between the sonic log velocities and the travel time tomography show a comparable fit with the sonic logs, the main trends of velocity change with depth are mapped. The more horizontal velocities, as determined from the tomography, are  $\sim 200$  m/s faster than the vertical sonic log velocities. This effect was observed by Zhang et al. (2012) as well.

Based on the average velocity model derived from the measured data, travel time tomography is tested on synthetic data having the same geometry as the real data. The results of the modelling study can be generalised for the interpretation of time-lapse crosshole experiments investigating the migration of CO<sub>2</sub> in a water saturated sandstone. Figure 4.19 summarizes the results of the travel time tomography based on synthetic travel times.

- **Shape of velocity anomaly:** The velocity change follows the input anomaly as a rough estimate of the location of the changes in the reservoir caused by the injection of CO<sub>2</sub>. Inherent layering or thinning of the input anomaly is not resolved. The CO<sub>2</sub> anomaly is smeared out beyond the range of the input model.
- **Amplitude of velocity anomaly:** The input velocity was reduced by 10% within the reservoir (corresponding to a CO<sub>2</sub> saturation of 30%), after forward calculation and inversion the final maximum velocity reduction in the reservoir was about 2%. The underestimation of the anomaly is linked to an overestimation of the observed travel time, since the fastest rays are those that circumvent the low velocity zone. This leads to an overestimation of the velocity and therefore to an underestimation of the amplitude of velocity anomalies in an inversion problem. For media with structures a size smaller than the Fresnel volume, this effect is intensified by the forward calculation of travel times based on the standard ray theory, which is derived using a high-frequency approximation (Musil et al. (2003), Spetzler et al. (2008)).



# 5 Chapter 5

---

## 5 Zero-offset VSP: baseline and repeat

*This chapter is about the zero-offset VSP baseline and repeat measurements in Ketzi. The main focus of the chapter is imaging of amplitude changes due to CO<sub>2</sub> injection.*

### 5.1 Motivation and research objectives

The main objective of the zero-offset and offset VSP surveys was to generate high-resolution seismic images in the vicinity of the borehole. As CO<sub>2</sub> replaces saline water in saturated sandstones, the impedance contrast between the gas filled sandstones and the caprock is increased, what leads to stronger reflections from top of the reservoir. This increased reflectivity can be used to image the spreading of CO<sub>2</sub> in the reservoir. Prior to injection the zero-offset and offset VSP baselines were measured November/December 2007 (Fig. 1.3, Chap. 1.3.1). The repeat of the zero-offset VSP was measured February 2011 (45770 t CO<sub>2</sub> injected), together with the repeat of the offset VSP.

Zero-offset VSP measurements provide near-well corridor stacks and information about normal incidence reflectivity. It is investigated, if CO<sub>2</sub> induced amplitude changes in the monitoring data, can be used to derive geometrical and petrophysical parameters describing the migration of CO<sub>2</sub> in a water saturated sandstone reservoir.

### 5.2 Equipment and recording parameters of the zero-offset VSP

The zero-offset VSP was recorded in the observation well Ktzi 202 (Fig. 2.4). Recording and pre-processing (shift-and-stack, Chap. 3.1) was done by Vibrometric Oy, Finland.

**Lubricator, access to pressurized wells:** Just as for the crosshole measurements (Chap. 4.2) a lubricator is needed to access the Ktzi 202 well during the repeat measurement after the breakthrough of CO<sub>2</sub>.

**Seismic sources VIBSIST-1000 and VIBSIST-3000:** The VIBSIST-1000 was used for the baseline measurements of zero-offset VSP and offset VSP (Chap. 6). For the repeat measurements the VIBSIST-3000 was used (Fig. 5.1). The VIBSIST source uses an excavator-mounted hydraulic rock-breaker, powered through a computer controlled flow regulator. The seismic signals are produced as rapid series of impacts on a steel

ground impact plate, maintaining a monotonic variation of the impact rate to achieve a non-repeatable sequence. The seismograms are obtained by cross-correlating the swept impact sequence with a pilot signal recorded at the source (Cosma and Enescu (2001)). The swept impact seismic technique (SIST) is described in Chapter 3.1. The impact sequence produced by the VIBSIST must be recorded in the immediate vicinity of the source location. The standard procedure involves a sensor installed on the impact plate and the transmission of the pilot signal by radio to the recording station (Yordkayhun et al. (2009a)). The table above Figure 5.1 gives an overview on the technical specifications of the VIBSIST-1000 and VIBSIST-3000.

hammer impact energy VIBSIST-1000	2500 J/impact
hammer impact energy VIBSIST-3000	3000 J/impact
maximum theoretical peak force	700 kN
impact frequency band	5 - 250 Hz
repetition rate	1 - 12 impacts/s
total weight	7.5 t



Figure 5.1: Technical specifications of the VIBSIST-1000 and VIBSIST-3000 (top) and VIBSIST-3000 during field work at Ketzin (bottom, photo: R. Giese).

**Borehole 3-component RD-XYZ-cg receiver:** The 3-component RD-XYZ-cg receiver is used for zero-offset and offset VSP measurements (Fig. 5.2, Yang et al. (2010)). The tool is equipped with omnidirectional geophones. "One component is directed along the borehole, while the others are perpendicular to the borehole and to each other" (Vibrometric (2012)). The units are clamped with independently controlled side-arms, activated by DC motors. The receiver chain is moved in the well by a winch with electrical power supply (Vibrometric (2012)). The table in Figure 5.2 lists the specifications of the RD-XYZ-cg receiver chain.

frequency range	60 - 2000 Hz
sensitivity	600 mV/ips
pre-amplification gain	50 or 100



Figure 5.2: Specifications of the RD-XYZ-cg receiver chain (top) and geophone receiver module with side clamping arm (bottom, photo: R. Giese).

**Recording parameters:** For the baseline 132 traces per component (2 horizontal, 1 vertical) with a sample rate of 0.25 ms and a length of 2499.75 ms have been recorded. Since the upper part of the baseline is affected by strong tube waves, only the lower part of the zero-offset VSP was repeated (Chap. 5.4.1): 80 traces per component with a sample rate of 0.25 ms and a length of 2047.75 ms have been recorded for the repeat. The sample frequency for both measurements is 4000 Hz, what leads to the Nyquist frequency of  $f_{Ny} = \frac{1}{2}f_{sample} = 2000$  Hz.

### 5.3 Geometry of the zero-offset VSP

The zero-offset VSP was measured in the observation well Ktzi 202 (Fig. 2.4). The source was placed within the range of a few meters to Ktzi 202. The baseline was measured with 132 depth levels, from 34 - 700 m below ground level (m b.gl.). Since the upper part of the baseline is affected by strong tube waves (Chap. 5.4.1), only the lower part of the zero-offset VSP was repeated. The repeat was measured at 80 depth levels, from 325 - 720 m b.gl.. The vertical distance between the levels is 5 m. For further processing and imaging only the vertical component of the data sets and only data which is not influenced by tube waves is used (460 - 700 m b.gl., 49 depth levels).

## 5.4 Processing the zero-offset VSP data

### 5.4.1 Influence of uncemented casing on data

The zero-offset VSP was measured in the observation well Ktzi 202. According to the reports from Rinke (2007) casing and cementation Ktzi 202 is shown in Figure 2.6. Large parts of the observation well is completed with "multiple casing in which the casing strings are not rigidly cemented to one another and also to the formation" (Hardage (2000), Chap. 2.4.1). This is an unfavourable casing situation for recording VSP data (Hardage (2000)), since there is no good medium (cement) between the casing and the

formation to transmit the seismic energy. Figure 5.3 shows the vertical component of the baseline zero-offset VSP together with the casing of Ktzi 202 and the lithology. The traces are balanced and a linear moveout (LMO) with steel velocity (6100 m/s, Keary et al. (2002)) was applied. Apparently, the waves down to 440 m below ground level (m b.gl.) travel along the uncemented steel casing. At 440 m b.gl. the first onsets are shifted and change their character, when the receivers are placed in cemented casing. Only traces which are not influenced by tube waves (below 440 m b.gl.) are used for processing and imaging.

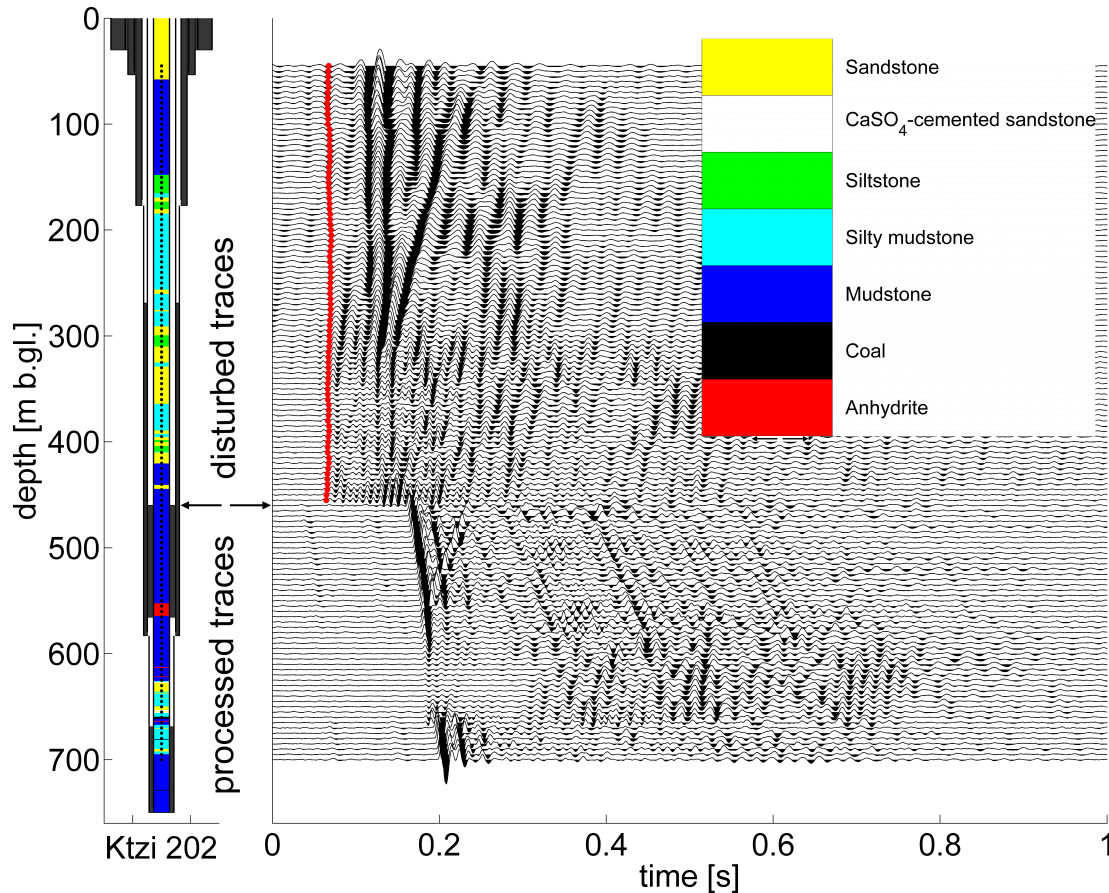


Figure 5.3: Vertical component of the baseline zero-offset VSP together with the casing of Ktzi 202 and the lithology. Left: Casing and cementation (grey) of Ktzi 202, the lithology is plotted in the centre of the well (Rinke (2007), Norden (2007)). Right: zero-offset VSP, vertical component with trace balance and LMO with 6100 m/s steel velocity (Keary et al. (2002)). The first breaks in the upper part are marked with red dots.

#### 5.4.2 Processing

The processing of the zero-offset VSP data is divided into three steps (Bubshait and Lawton (2008)): (1) shifting and cross-correlating the traces to equal first break times, (2) removal of downgoing and enhancement of upgoing waves by median filtering and (3) application of a corridor mute to account for propagation effects of upgoing waves, such as multiples. In this case, neither corrections of spherical spreading or trace balance nor a deconvolution operator is applied.

(1) **Shifting and cross-correlating the traces to equal first break times:** A

bulk static shift upward is applied to compensate for source delays (baseline 25 ms, repeat 50 ms). The polarity of the baseline traces is reversed, to set the first break amplitude positive and the trace length is cut to 2047.75 ms to make both measurements the same length. The repeat traces are matched to the baseline traces by application of a cross-correlation time-shift (Bergmann et al. (2011)): First, the sampling rate of baseline and repeat data is increased to 0.1 ms to allow a finely resolved cross-correlation time-shift of the repeat data. Then, the cross-correlation of baseline and repeat traces is calculated. Finally, the time-shift between the maximum of the cross-correlation and zero-lag is applied to the repeat data. Figure 5.4 shows the vertical component of measured data (left column) and modelled data (right column) after bulk static shifts and cross-correlation. The generation of the modelled data is described in Chapter 5.7. Baseline and repeat data are shown in the top and bottom row, respectively. An upgoing reflection from the K2 anhydrite layer can be observed in the measured baseline and modelled data (Fig. 5.4, blue lines). In the baseline data, at depth range of the reservoir the first breaks have low energy and a resonance in the wavefield between 0.4 ms and 0.9 ms is observed. This is related to an uncemented part of the single casing string (Fig. 5.3). The wavefield of the repeat data displays no resonance and a different characteristic of the downgoing wave. These differences can be source related, since for baseline and repeat measurements the VIBSIST-1000 and VIBSIST-3000, with a different impact energy, were used (Chap. 5.2). Furthermore, the source was placed on asphalt close to the well for the baseline measurement, whereas for the repeat it was moved a few meters away and activated on gravel, what might reduce the influence of the casing. Better seismic bonding to the formation has also been observed as a well ages, since drilling mud, rock cuttings, and sloughing that fill the annulus between the casing and the formation tend to solidify (Hardage (2000)). This can also contribute to the differences between baseline and repeat data.

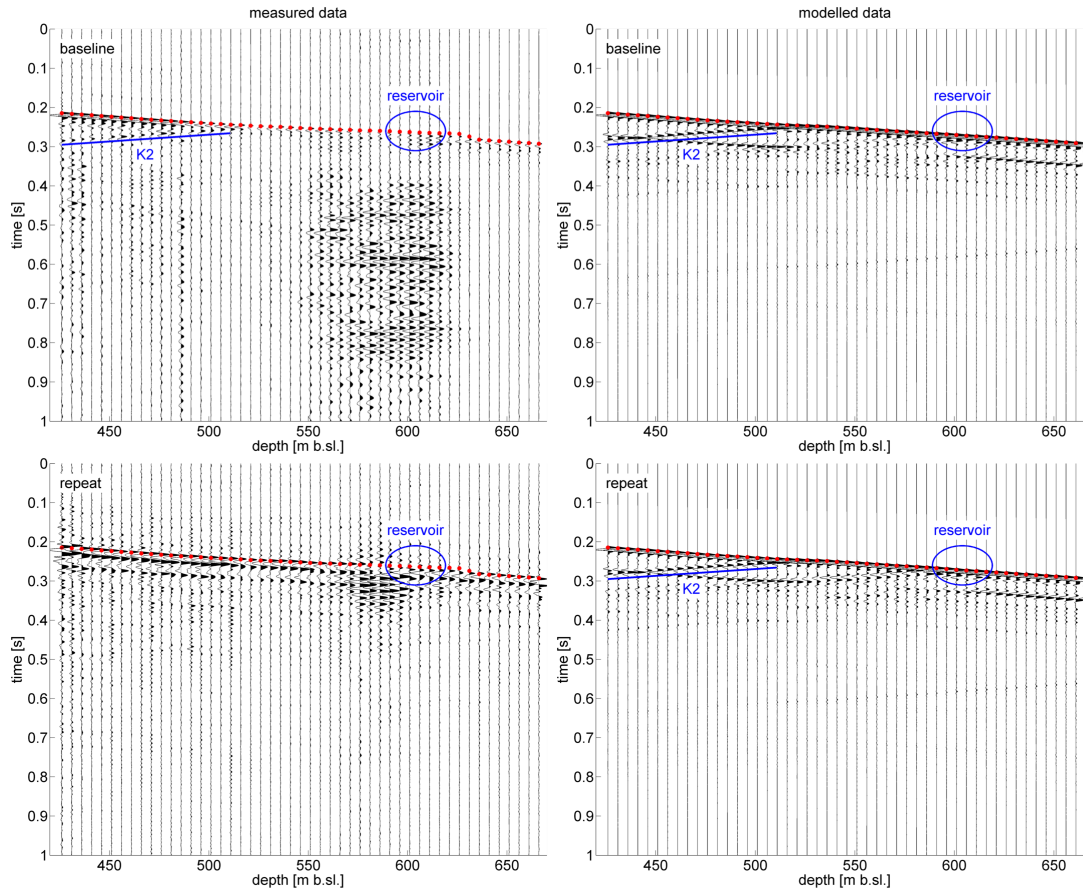


Figure 5.4: Zero-offset VSP vertical component, measured (left column) and modelled (right column) data after bulk static shifts and cross-correlation. Baseline and repeat data are shown in the top and bottom row, respectively. Upgoing reflections from the K2 anhydrite layer (blue lines) and the depth of the reservoir (blue circle) are indicated. The red dots indicate the picked first break travel times. The depth is in meter below sea level [m b.sl.].

**(2) Removal of downgoing and enhancement of upgoing waves by median filtering:** The downgoing waves are flattened to coherent events by applying a static shift according to the picked first break travel times (Fig. 5.4, red dots). These coherent events are reproduced with a 9-point median filter and then subtracted from the traces. The traces are shifted back twice the picked travel time, which leads to a horizontal alignment of upgoing events. To enhance the horizontal energy a 9-point median filter is applied. The horizontally aligned upgoing waves are shown in Figure 5.5 for the measured and modelled data. The reflection from the K2 is observed in all measurements and marked by red lines. The 9-point median filters, compared to filters of different order, best enhanced the upgoing waves while eliminating the downgoing waves.

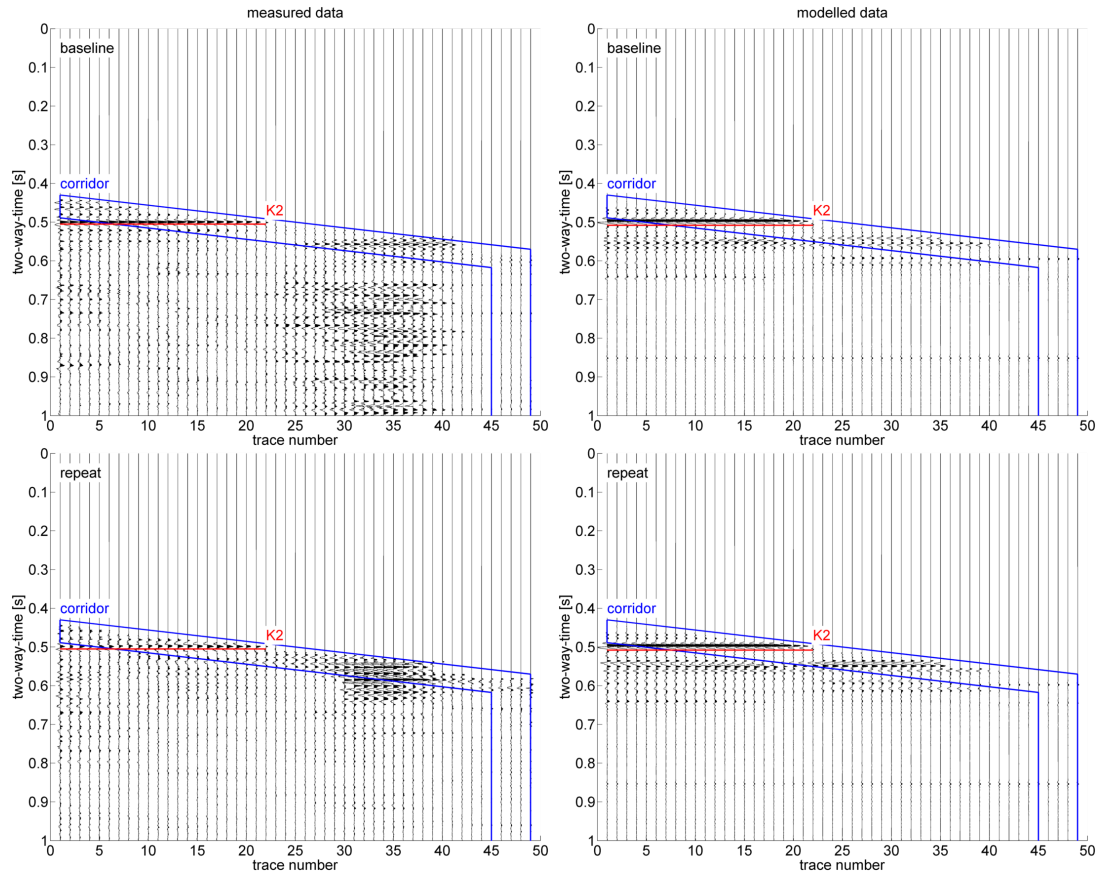


Figure 5.5: Zero-offset VSP vertical component, measured (left column) and modelled (right column) data after removing the downgoing waves, horizontal alignment and enhancement of the upgoing waves. Baseline and repeat data are shown in the top and bottom row, respectively. The reflection from the K2 is observed in all measurements and marked by red lines. The blue polygon indicates the corridor mute window, which is applied in processing step (3).

**(3) Application of an outside corridor to account for propagation effects of upgoing waves, such as multiples:** After trace balancing, the last step is the application of an outside corridor mute of 60 ms (Fig. 5.6, Hampson and Mewhort (1983)). The width of the corridor mute was adjusted to achieve good correlation between the zero-offset VSP data and the 3D surface seismic data. Comparing the baseline (top row) and repeat data (bottom row), one can notice the increased amplitudes at the two-way-time of the reservoir ( $\sim 550$  ms).

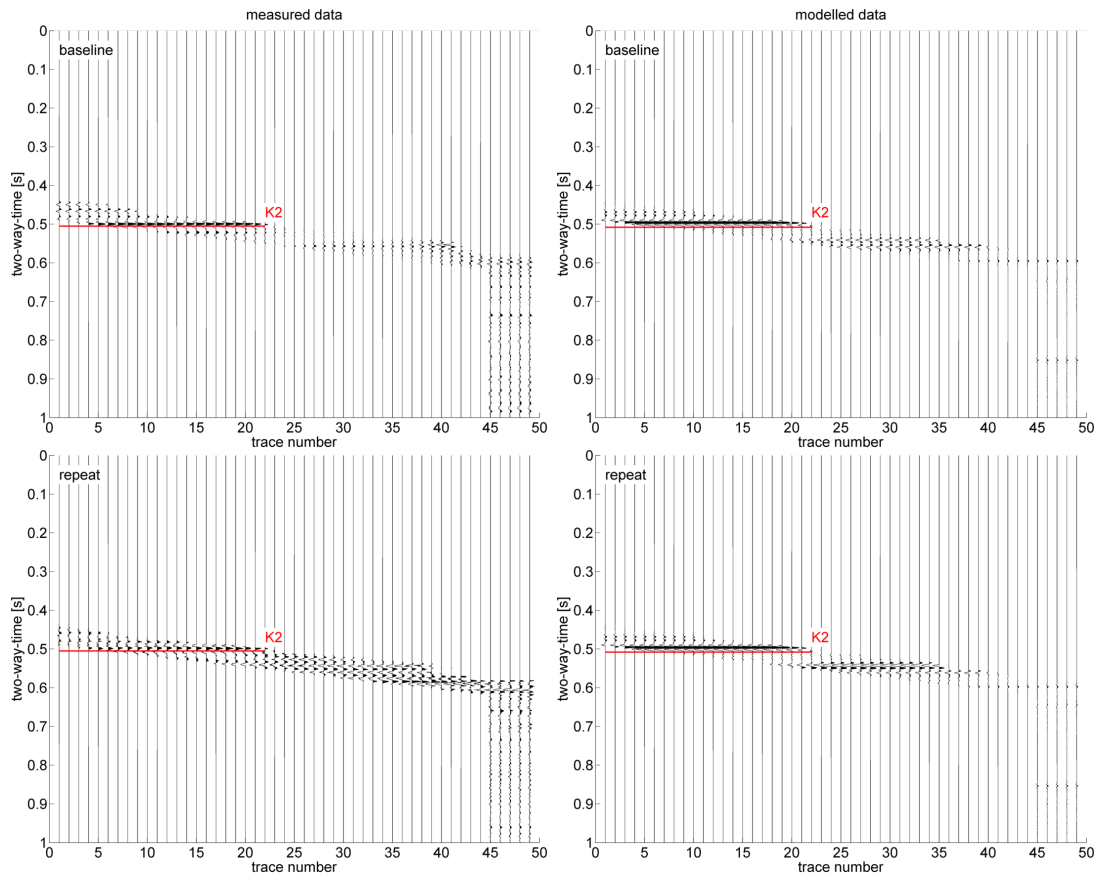


Figure 5.6: Zero-offset VSP vertical component, measured (left column) and modelled (right column) data after trace balancing and application of a corridor mute. Baseline and repeat data are shown in the top and bottom row, respectively. The reflection from the K2 is observed in all measurements and marked by red lines.

## 5.5 Frequency before and after processing

Figure 5.7 shows the amplitude spectra of the zero-offset VSP baseline for measured and modelled data (top and bottom row). Baseline and repeat measurements are plotted as black and blue lines. The spectra of raw data are shown on the left, the spectra after processing (Chap. 5.4) are shown on the right. The main frequency content of the data lies between 25 Hz and 125 Hz, with a centre frequency of 60 Hz.

There is a noticeable difference in the frequency spectra of baseline and repeat data. The baseline spectrum exhibits two strong amplitude peaks at 50 and 80 Hz, whereas the repeat has one main frequency of 60 Hz (Fig. 5.7, top right). This tendency can be observed in the raw data as well (Fig. 5.7, top left). Differences in the frequency content can be source related: for baseline and repeat measurements the VIBSIST-1000 and VIBSIST-3000, with a different impact energy, were used (Chap. 5.2). Furthermore, the source was placed on asphalt close to the well for the baseline measurement, whereas for the repeat it was moved a few meters away and activated on gravel, what can lead to a stronger attenuation of the signal at higher frequencies. In order to make baseline and repeat data comparable, a bandpass with corner frequencies of 10-20-80-100 Hz is applied to both measurements before displaying the data (Chap. 5.6). This bandpass

is indicated by the blue line in Figure 5.7.

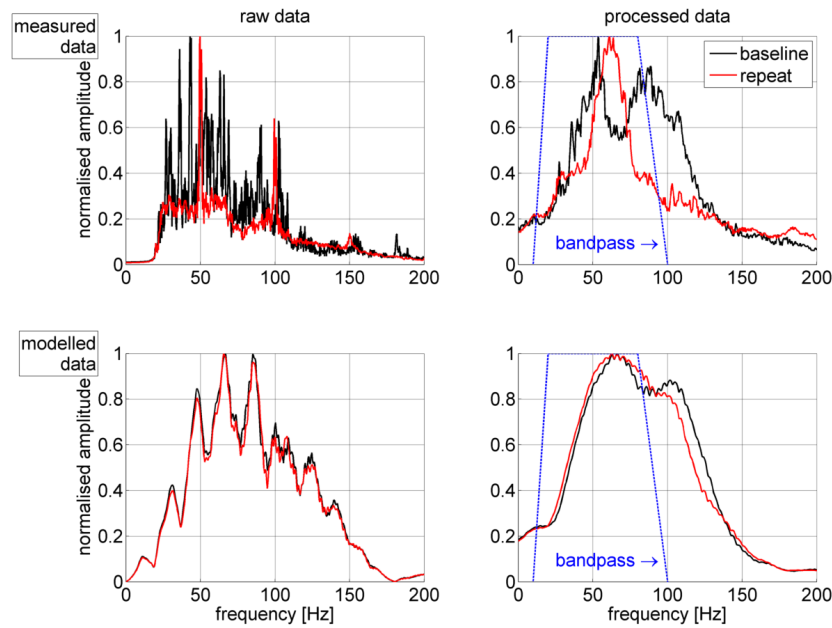


Figure 5.7: Normalised amplitude spectra of the zero-offset VSP baseline for measured and modelled data (top and bottom row). Baseline and repeat measurements are plotted as black and blue lines. The spectra of raw data are shown on the left, the spectra after processing (Chap. 5.4) are shown on the right. The blue line indicates the corner frequencies of a bandpass filter (10-20-80-100 Hz) which is applied before displaying the data (Chap. 5.6).

## 5.6 Comparison of zero-offset VSP with 3D surface seismic

The processed traces (Chap. 5.4, Fig. 5.6) are vertically stacked (median stack) and duplicated 9 times before displaying. Figure 5.8 shows a detail of inline 1172 of the baseline 3D surface seismic which crosses the observation well Ktzi 202 (Fig. 1.2). The stacked traces of the zero-offset VSP baseline and repeat measurements are inserted at the intersection with the well. Two different bandpass filters are applied: In order to make zero-offset VSP baseline and repeat data comparable, a bandpass with corner frequencies of 10-20-80-100 Hz is applied (Fig. 5.8, top). For comparison of the zero-offset VSP with the 3D surface seismic a bandpass with corner frequencies of 10-20-50-70 Hz is applied (Fig. 5.8, bottom). The different data sets are normalised to the centre peak of the K2 reflector. To normalise the 3D surface seismic inline, one trace on each side of the well, is used as reference. Furthermore, the K2 of the zero-offset VSP is matched in time with the K2 of the 3D surface seismic. The time shift of the K2 between zero-offset VSP baseline and repeat is 11.5 ms (46 samples). The time-shift between zero-offset VSP and 3D surface seismic is 26 ms (104 samples). This shift is caused by various statics applied to the 3D surface data like bulk static shifts to compensate for source delay, refraction statics and residual statics (Ivanova et al. (2012)). The black lines in Figure 5.8 mark the positions of the K2 (upper line), the top and bottom of the reservoir (middle and bottom line). The K2 is picked within the upper trough of the strong double reflection (trough-peak-trough, Juhlin et al. (2007)). Since the reservoir is not indicated as a clear reflection (Juhlin et al. (2007)), it is

marked with an offset of 43 ms. The offsets between K2 and reservoir are derived by a depth-to-time conversion of the sonic log (Chap. 5.8.1).

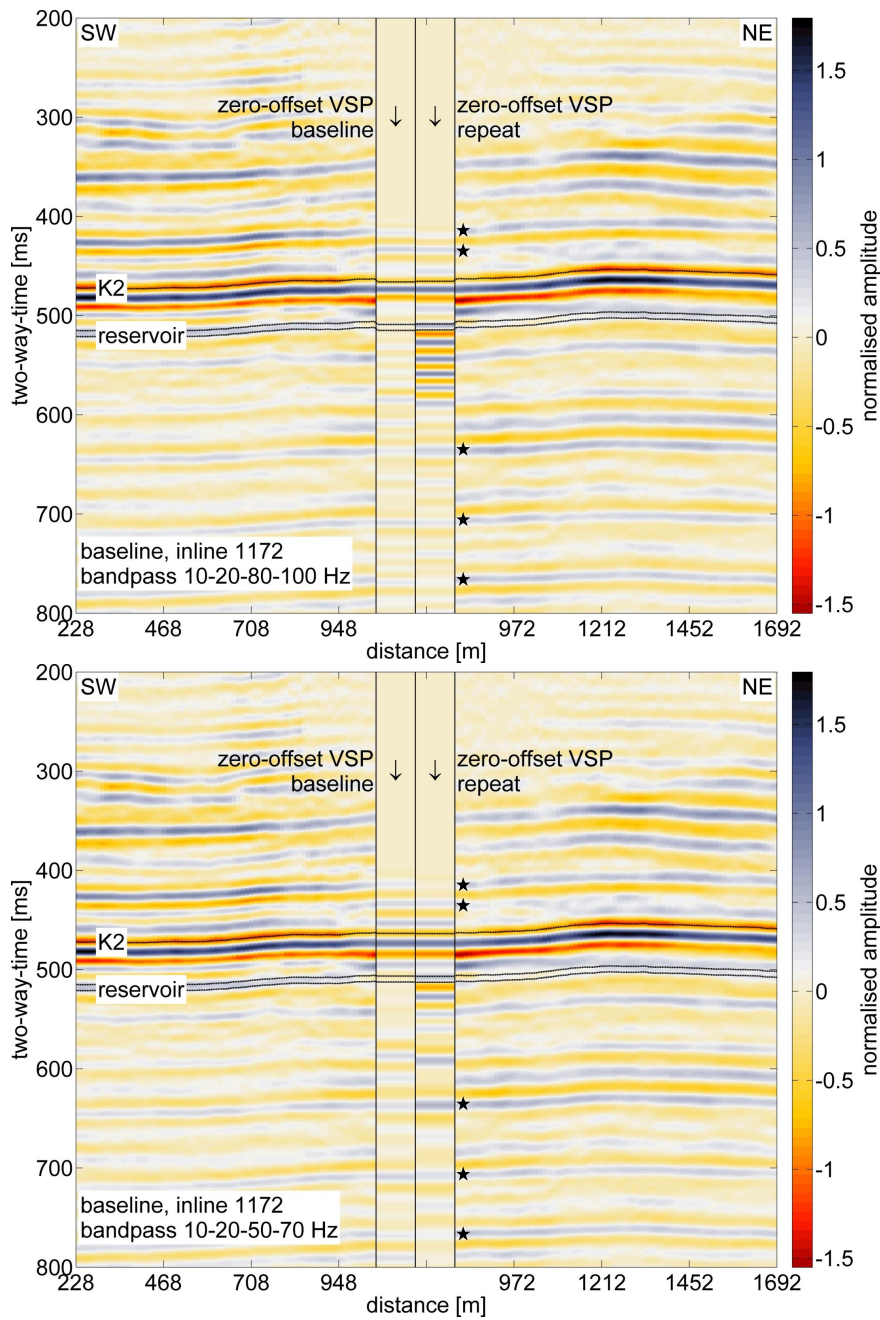


Figure 5.8: Comparison of zero-offset VSP with 3D surface seismic. A detail of inline 1172 of the baseline 3D surface seismic (Fig. 1.2) which crosses the observation well Ktzi 202 is shown. The traces of the zero-offset VSP baseline and repeat measurements are inserted at the intersection with the well. Top: zero-offset VSP traces with a 10-20-80-100 Hz bandpass. Bottom: zero-offset VSP traces with a 10-20-50-70 Hz bandpass. The black lines mark the positions of the K2 (upper line), the top and bottom of the reservoir (middle and bottom line). Consistent phases of 3D surface seismic and zero-offset VSP are marked with stars.

When comparing the 3D surface seismic inline with the zero-offset VSP data, it is possible to identify consistent phases marked with stars in Figure 5.8. The dynamic range of the amplitudes is comparable for both methods, as well. The baseline VSP exhibits weak amplitudes from top of the reservoir to 600 m depth and is therefore hardly comparable to 3D surface seismic or repeat VSP measurement. As in 3D surface seismic the reservoir is not indicated as a clear reflection in the baseline zero-offset VSP data. For the VSP data, this is related to an uncemented part of the single casing string (Fig. 5.3, Chap. 5.4.2). CO<sub>2</sub> induced changes in reflectivity can be observed in the zero-offset VSP repeat data. The amplitudes of the high frequency VSP data (Fig. 5.8, top) show a strong amplitude signature, with ringing extending almost 70 ms below the reservoir. Within the bandpass filtered data (Fig. 5.8, bottom) the increased amplitudes are confined to reservoir depth. More details of the structure below the top of the reservoir are resolved in the zero-offset VSP repeat data than in the 3D surface seismic data. When comparing the offset VSP and the 3D surface seismic difference, one has to bear in mind that the associated repeat measurements were measured at different times. The 3D surface seismic repeat was measured in autumn 2009 with 22 - 25 kt of CO<sub>2</sub> injected, whereas the zero-offset VSP was repeated in February 2011 with ~ 46 kt of CO<sub>2</sub> injected (Fig. 1.3).

## 5.7 Modelling of zero-offset VSP data

*Modelling of zero-offset VSP data was done to test the processing workflow. Furthermore, when evaluating the velocity change in the reservoir by band limited impedance inversion (Chap. 5.8), recovering the pre-set velocity contrast when modelling the data, is an indication for the quality of the inversion process.*

### 5.7.1 Petrophysical model parameters

The modelling was done in ReflexW based on an 1D seismic elastic model, for which three petrophysical parameters are needed: The P-wave velocity, the S-wave velocity and the density.

**P-wave velocity:** Since only zero-offset VSP receivers below 460 m below ground level are processed and imaged (Chap. 5.4) a constant P-wave velocity of 2900 m/s is assumed in the upper part of the model (down to 430 m below ground level). To derive the finer structure in the lower part of the model, where the zero-offset receivers are actually placed, the 10-point median filtered P-wave sonic log of Ktzi 202 (Fig. 5.9, thin black line) is averaged over the model layers (Fig. 5.9, thick black line). The CO<sub>2</sub> injection is simulated by decreasing the P-wave velocity of the model by 30 % in the depth range of the reservoir (Fig. 5.9, red line). This velocity reduction is chosen based on the results of the impedance inversion of the zero-offset VSP measurements (Chap. 5.8, Fig. 5.16). As reservoir the first sandstone layer within the Stuttgart Formation is chosen (Chap. 5.8.1).

**S-wave velocity:** The S-wave velocity was derived for the same model layers as the P-wave velocity, based on the S-wave sonic log of Ktzi 202 (Chap. 2.4.3). Figure 5.9 shows the 10-point median filtered S-wave sonic log of Ktzi 202 (thin green line) and the averaged velocity over the layers (thick green line). Since laboratory experiments of Kummerow and Spangenberg (2011) indicated no change in S-wave velocity due to CO<sub>2</sub> injection, the S-wave velocity is kept constant for baseline and repeat (Chap. 2.3.3).

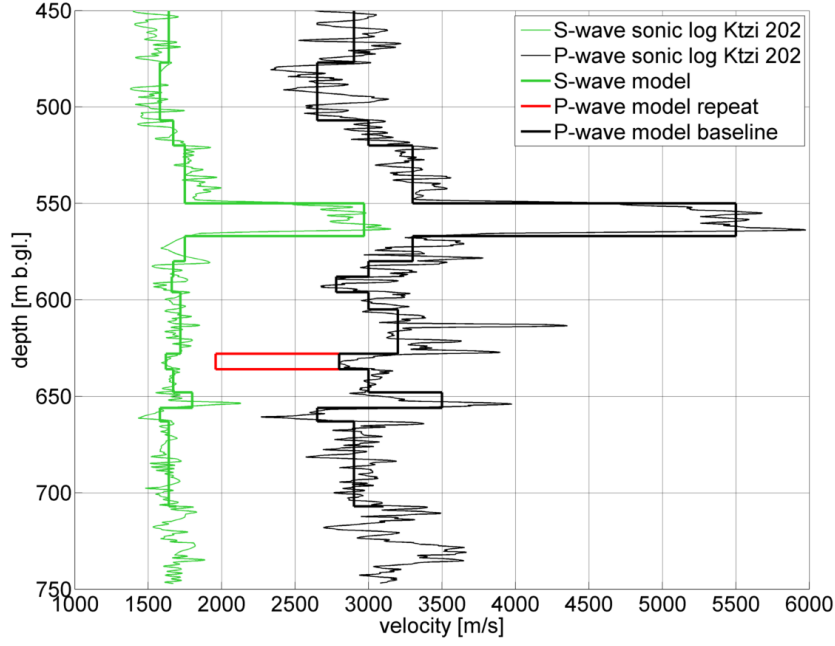


Figure 5.9: P-wave and S-wave velocity model. Thin black line: 10-point median filtered P-wave sonic log of Ktzi 202. Thick black line: P-wave velocity averaged over the model layers. Red line: reservoir layer with a velocity reduction of 30%. Thin green line: 10-point median filtered S-wave sonic log of Ktzi 202. Thick green line: S-wave velocity averaged over the model layers.

**Density:** Figure 5.10 shows the density model, which was derived in the same way, as the P-wave velocity model, based on the density log of Ktzi 202 (Chap. 2.4.3). A constant density of  $2.3 \text{ g/cm}^3$  is assumed in the upper part of the model (down to 430 m below ground level). Figure 5.10 shows the density log of Ktzi 202 (thin black line) and the averaged density over the layers (thick black line). The  $\text{CO}_2$  injection is simulated by decreasing the density from  $2.2 \text{ g/cm}^3$  to  $2.0 \text{ g/cm}^3$  within the reservoir. (Fig. 5.10, red line). The density reduction in the reservoir is based on the following calculations. The density of the rock matrix  $\rho_{matrix} = 2.5 \text{ g/cm}^3$  is derived with

$$\rho_{brine\ saturated} = \rho_{matrix} (1 - \phi) + \rho_{brine} \phi \quad (5.1)$$

where the density of the brine saturated rock  $\rho_{brine\ saturated} = 2.2 \text{ g/cm}^3$  (Fig. 5.10), the effective porosity  $\phi = 20\%$  (Chap. 2.3.1) and the density of the brine  $\rho_{brine} = 1.2 \text{ g/cm}^3$  (Ivanova et al. (2012)).

An estimation of the  $\text{CO}_2$  saturation cannot be made based on Kummerow and Spangenberg (2011) (Chap. 2.3.3), since the maximum measured velocity reduction was 16% with a  $\text{CO}_2$  saturation of 45%. Based on the results of the impedance inversion of the zero-offset VSP measurements (Chap. 5.8) which indicates a velocity contrast of 30%, a fully  $\text{CO}_2$  saturated rock is assumed. This means the brine within the effective pores is totally replaced by  $\text{CO}_2$  with a density of  $\rho_{\text{CO}_2} = 0.2 \text{ g/cm}^3$  (Ivanova et al. (2012)). The density of the  $\text{CO}_2$  saturated rock  $\rho_{\text{CO}_2\ saturated} = 2.0 \text{ g/cm}^3$  is calculated with

$$\rho_{\text{CO}_2\ saturated} = \rho_{matrix} (1 - \phi) + \rho_{\text{CO}_2} \phi \quad (5.2)$$

where  $\rho_{matrix}$  has been calculated with Equation 5.1.

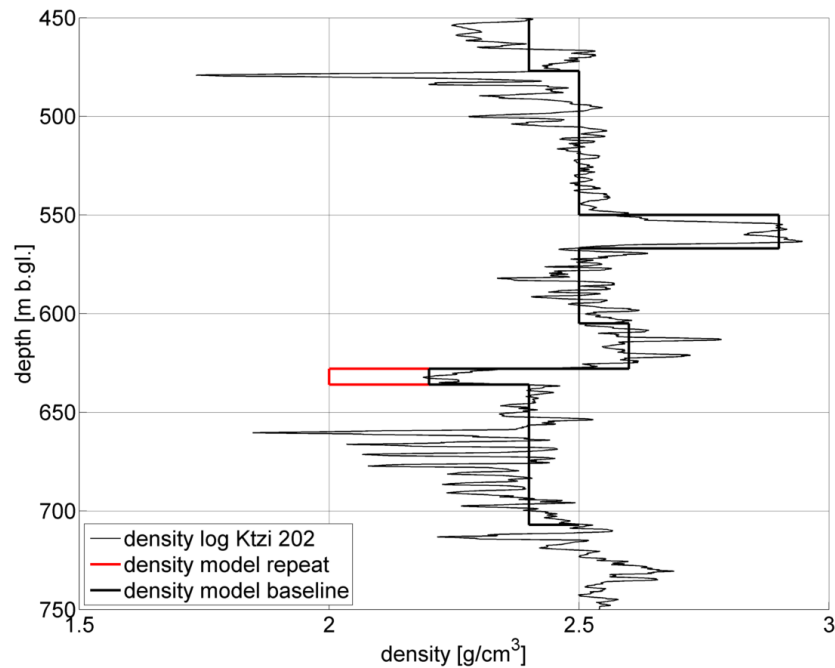


Figure 5.10: Density model. Thin black line: density log of Ktzi 202. Thick black line: density averaged over the model layers. Red line: Reservoir layer with a density reduction from  $2.2 \text{ g/cm}^3$  to  $2.0 \text{ g/cm}^3$ .

### 5.7.2 2D Finite Difference (FD) modelling

*The modelling is done with the Finite Difference (FD) modelling tool of the ReflexW software, which allows the simulation of seismic wave propagation based on the 2D elastic-wave equation.*

”This method allows the simulation of the kinematic (travel time) as well as dynamic (amplitude, frequency)” attributes. ”No attenuation is taken into consideration and the elastic parameters are assumed to be frequency independent” (Sandmeier (2004)).

**Geometry of the model:** The 1D seismic elastic model (Chap. 5.7.1), is transferred to a lateral constant 2D model in ReflexW. Figure 5.11 shows the geometry of the model. The model boundaries (top, sides and bottom) have distances of  $\sim 100 \text{ m}$  to the source and receiver locations to minimize their influence. That leads to model dimensions of 0-200 m in horizontal direction and 0-1200 m in vertical direction. The source and the receivers are placed in the centre of the model, with an horizontal offset of 10 m between source and receivers. The whole model was shifted 100 m downward, leading to a thick homogeneous top layer, in which the source is placed at 100 m depth, the receiver depth range is also shifted relative to the source depth to 560-800 m (Chap. 5.3).

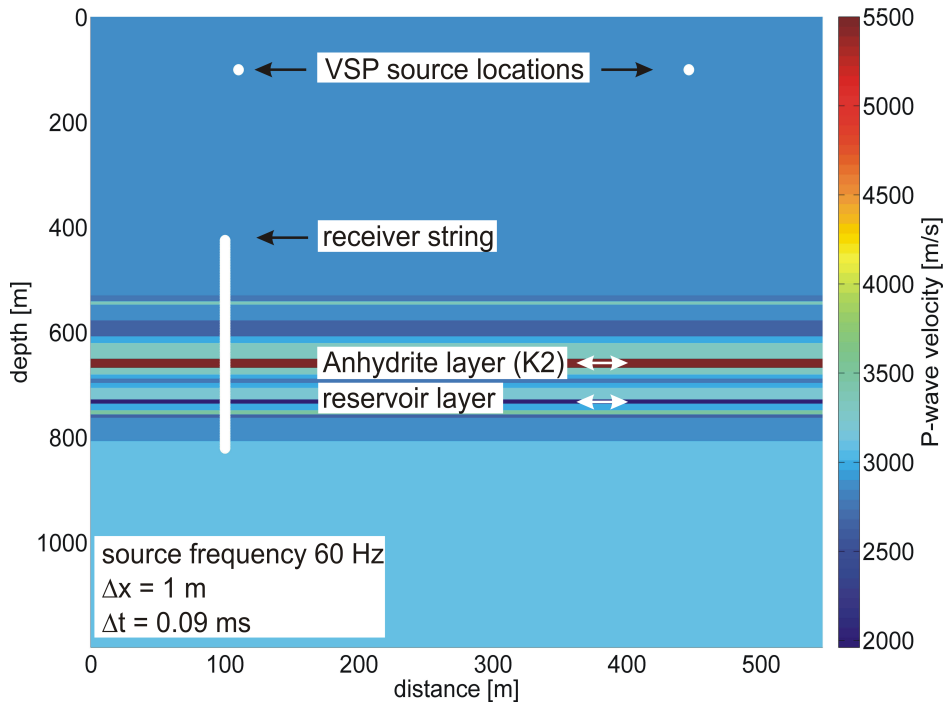


Figure 5.11: Geometry of the lateral constant 2D ReflexW model. Exemplary, the P-wave velocities of the repeat are shown. The source (white points) and receiver (white line) locations are indicated. The whole model was shifted 100 m downward, leading to a thick homogeneous top layer, in which the source is placed at 100 m depth, the receiver depth range is also shifted relative to the source depth to 560-800 m (Chap. 5.3). Modelling of the offset VSP was done for the same seismic elastic model, so the offset VSP location is marked as well (Chap. 6.7).

**2D FD modelling parameters:** The source is a P-wave minimal phase, point source with a centre frequency of 60 Hz (Chap. 5.5). For the FD computation the seismic elastic model is rasterised with a given increment in horizontal and vertical direction. The size of the space increment corresponds to the minimal wave length. "The program determines automatically the critical value of the space increment for the 2D FD scheme as 1/8 of the minimum wave length ( $\lambda_{min} = v_{s,min}/f = 1580/60 \text{ m} = 3.29 \text{ m}$ , Fig. 5.9). This value should not be passed over, a too big chosen space increment results in numerical dispersion of the wavelet" (Sandmeier (2004)). For the modelling of zero-offset VSP data a space increment of 1 m is chosen. A time increment has to be given as well and the maximum time increment depends on the maximum velocity  $v_{p,max}$  as well as on the given space increment  $\Delta x$ , with  $\Delta t \leq \Delta x/2v_{p,max} = 1/(2 \cdot 5500) \text{ s} = 0.09091 \text{ ms}$  (Fig. 5.9). "A too big chosen  $\Delta t$  increment results in an instability, this means the amplitude increases exponentially with time" (Sandmeier (2004)). The  $\Delta t$  for the modelling is set to 0.09 ms. The trace length is 2047.75 ms, equal to the real measurements (Chap. 5.2). The boundary condition of the model is set to absorbing and only the vertical displacement is calculated.

### 5.7.3 Processing

The modelled traces are processed in the same way as the measured traces (Chap. 5.4.2) and shown in the right column of the Figures 5.4-5.6. Since the velocity model is set to

a constant velocity down to 430 m below ground level (Chap. 5.7.1), the resulting shift of the first break travel times is corrected during the processing of the modelled data. The first break travel times of the modelled data have to be shifted 51.53 ms downward to match the first break travel times of the baseline measurements.

#### **5.7.4 CO<sub>2</sub> signature of measured and modelled zero-offset VSP**

Figure 5.12 shows a detail of the 3D surface seismic baseline of Figure 5.8 (Chap. 5.6). The traces of the measured and modelled VSP are plotted side by side and inserted at the intersection of inline 1172 with the well. Figure 5.12 shows from top to bottom baseline, repeat and difference (repeat minus baseline) of 3D surface seismic and VSP. The VSP data of the left column is bandpass filtered with corner frequencies of 10 - 20 - 80 - 100 Hz. For a better comparison with the 3D surface seismic, the VSP data of the right column is bandpass filtered with corner frequencies of 10 - 20 - 50 - 70 Hz. As in Chapter 5.6 the different data sets are normalised and matched in time to the centre peak of the K2 reflector. The black lines in Figure 5.12 mark the positions of the K2 (upper line), the top and bottom of the reservoir (middle and bottom line).

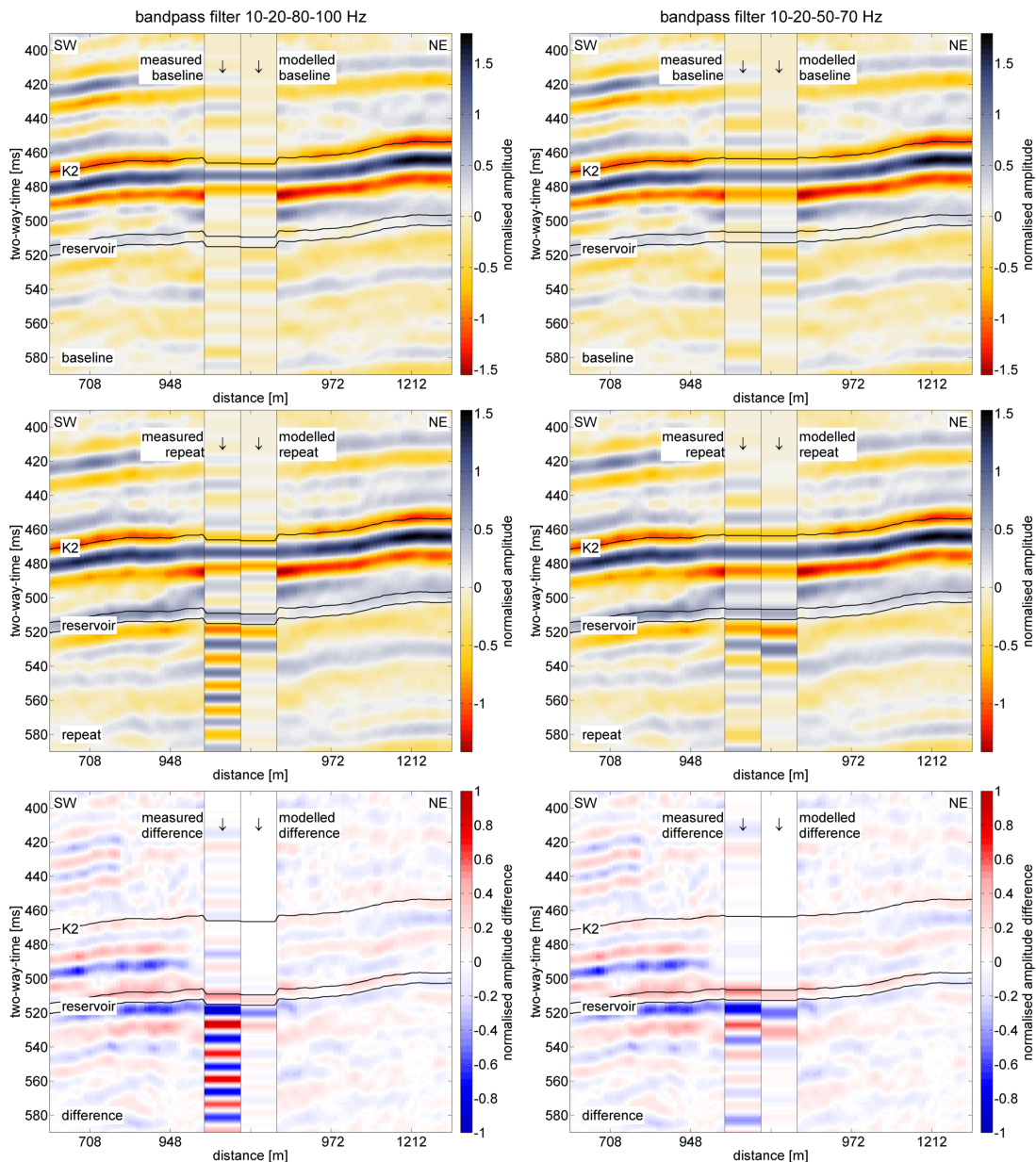


Figure 5.12: CO<sub>2</sub> signature of measured and modelled zero-offset VSP. A detail of the 3D surface seismic baseline of Figure 5.8 (Chap. 5.6) is shown. The traces of the measured and modelled VSP are plotted side by side and inserted at the intersection of inline 1172 with the well. From top to bottom baseline, repeat and difference (repeat minus baseline) of 3D surface seismic and VSP are shown. The VSP data of the left column is bandpass filtered with corner frequencies of 10 - 20 - 80 - 100 Hz, the VSP data of the right column is bandpass filtered with corner frequencies of 10 - 20 - 50 - 70 Hz. The black lines mark the positions of the K2 (upper line), the top and bottom of the reservoir (middle and bottom line).

The dynamic range of modelled amplitudes is comparable to the measured data. Contrary to 3D surface seismic and measured zero-offset VSP, the reservoir is indicated as a reflection (positive amplitude) in the modelled baseline data for both frequency bands (Fig. 5.12, top row). The reflections from the reservoir are not observed in the measured

baseline data, since the receivers have been placed in an uncemented part of the single casing string (Fig. 5.3, Chap. 5.4.2, Chap. 5.6). The reservoir becomes visible in the repeat data, due to the increased velocity contrast (Fig. 5.12, middle row). Phases and amplitudes of measured and modelled repeat are in good agreement besides a slight shift below the reservoir. Within the difference sections (repeat minus baseline, Fig. 5.12, bottom row) a clear signature caused by the injection of CO<sub>2</sub> is visible. Above the reservoir weak amplitude artefacts are still visible in the measured data. The top of the reservoir is characterised by a positive amplitude difference. This is consistent with the 3D surface seismic data. With closer look at the wavefield one can observe a positive amplitude at the top of the reservoir, followed by negative amplitude and again a positive amplitude. Within the high frequency data (left column) the difference is dominated by the ringing of the repeat, but the bandpass filtered zero-offset VSP difference shows good correlation with the modelled VSP difference.

### 5.7.5 Estimation of CO<sub>2</sub> layer thickness from zero-offset VSP data

For the Ketzin site, the sandstone layer of the reservoir close to Ktzi 202 has a thickness of 8 m (Chap. 5.8.1). When modelling the VSP experiment it was assumed, that the thickness of the CO<sub>2</sub> plume equals the reservoir layer thickness. A possible alternative scenario would be, that the CO<sub>2</sub> plume migrates along the top of the reservoir, filling it only partially (Lengler (2012)). Is it possible to derive an estimate of the CO<sub>2</sub> layer thickness based on the zero-offset VSP data? To answer this question, a wedge model study was performed based on the P-wave, S-wave and density model described in Chapter 5.7.1. The thickness of the reservoir layer characterised by a 30% P-wave velocity reduction is reduced stepwise from 16 m to 4 m. The modelled traces are processed and imaged as described in Chapter 5.7.3. Figure 5.13 shows the result of wedge modelling for the 10-20-50-70 Hz bandpass filtered data. The stacked trace of the measured repeat is plotted on the left side. The coloured amplitudes are overlain by the wiggle trace. The top of the reservoir is plotted as green line and the maximum amplitude of the reflection from top of the reservoir is marked by a green dot. On the right the results of the wedge model are shown, from left to right for 16 m, 12 m, 8 m, 6 m and 4 m reservoir thickness. The lower green line, indicates the bottom of the reservoir.

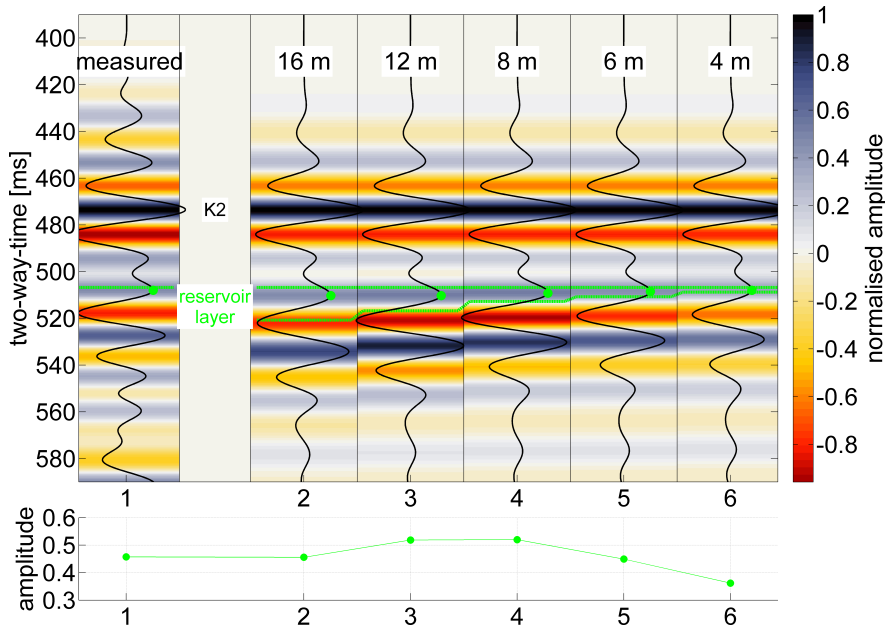


Figure 5.13: Result of wedge modelling for the 10-20-50-70 Hz bandpass filtered data. The stacked trace of the measured repeat is plotted on the left side. The coloured amplitudes are overlain by the wiggle trace. On the right the results of the wedge model are shown, from left to right for 16 m, 12 m, 8 m, 6 m and 4 m reservoir thickness. The top of the reservoir is plotted as green line and the amplitudes of the reflections from top of the reservoir are marked by green dots. The lower green line, indicates the bottom of the reservoir. The values of the picked amplitudes (green dots) are plotted in the graph below the figure.

The reservoir is not resolved as separate reflection events, the wavefield is characterised by the interference of reflections from top and bottom of the reservoir (positive-negative-positive). With reducing the reservoir layer thickness, interference tuning can be observed. The values of the picked amplitudes (green dots) are plotted in the graph below the figure. The amplitude reaches a maximum for a CO<sub>2</sub> layer thickness between 12 m and 8 m, the amplitude of the original trace is recovered for a layer thickness of 6 m. When comparing both, the shape and the amplitude of the measured and modelled zero-offset VSP, the CO<sub>2</sub> layer thickness is estimated with 6 m. It is possible that at the time of the zero-offset VSP repeat, the reservoir layer was not totally influenced by the CO<sub>2</sub> plume, but only the uppermost 6 m.

## 5.8 Band limited impedance inversion of measured and modelled zero-offset VSP

### 5.8.1 Depth-to-time conversion of sonic log Ktzi 202

Since the zero-offset VSP is measured in Ktzi 202 (Chap. 5.3), the conversion is done for the sonic log of Ktzi 202 (Chap. 2.4.3). The results of conversions between time and depth domain will be shown as an example for inline 1172, which intersects the observation well Ktzi 202 (Fig. 1.2).

(1) **Depth-to-time conversion:** First, the transit time  $t_{transit,i}$  between the depth

levels  $z_i$  of the sonic log is calculated

$$t_{transit,i} = \frac{z_{i+1} - z_i}{v_{p,i}} \quad (5.3)$$

where  $v_{p,i}$  is the sonic P-wave velocity of the  $i$ -th depth level. The transit times are summed over the entire length of the sonic log and doubled to derive the two-way-time (TWT) function. The sonic log is tied to the 3D surface seismic, by shifting the TWT function to the upper trough of the strong double reflection (trough-peak-trough) of the K2 (Juhlin et al. (2007), Fig. 5.14).

**(2) Reservoir depth in time domain:** Since the reservoir is not indicated as clear reflection (Juhlin et al. (2007)), its position in time is derived from the depth-to-time converted sonic log (Fig. 5.14), relative to the K2 reflection. Figure 5.14 explains the chosen offsets between reservoir and K2. On the left, the median filtered (10-point filter) sonic log of Ktzi 202 in depth is shown with the lithology of Ktzi 202 (Chap. 2.4.3). A 10-point median filter was found to be a good compromise between smoothing the sonic log, while preserving lithological features, e.g. the K2 reflector or the two thin anhydrite layers above the reservoir. The K2, the top and the bottom of the reservoir are marked with stars. As reservoir the first sandstone layer within the Stuttgart Formation is chosen.

On the right side of Figure 5.14 a detail of the inline 1172 of 3D surface seismic baseline is shown (Juhlin et al. (2007)). At the intersection between inline 1172 and observation well Ktzi 202 (Fig. 1.2), the depth to two-way-time converted sonic log is shown. Identical to the sonic log in the depth domain (left image), the K2, the top and bottom of the reservoir are picked in the time domain (right image, marked as stars). This leads to the K2 at 463 ms, the top of the reservoir at 506 ms (offset to K2 43 ms) and the bottom of the reservoir at 512 ms (offset to K2 49 ms). This is in accordance with the top of the Stuttgart Formation in Lüth et al. (2011), which was picked 42 ms below the K2 horizon (Figure 1.2).

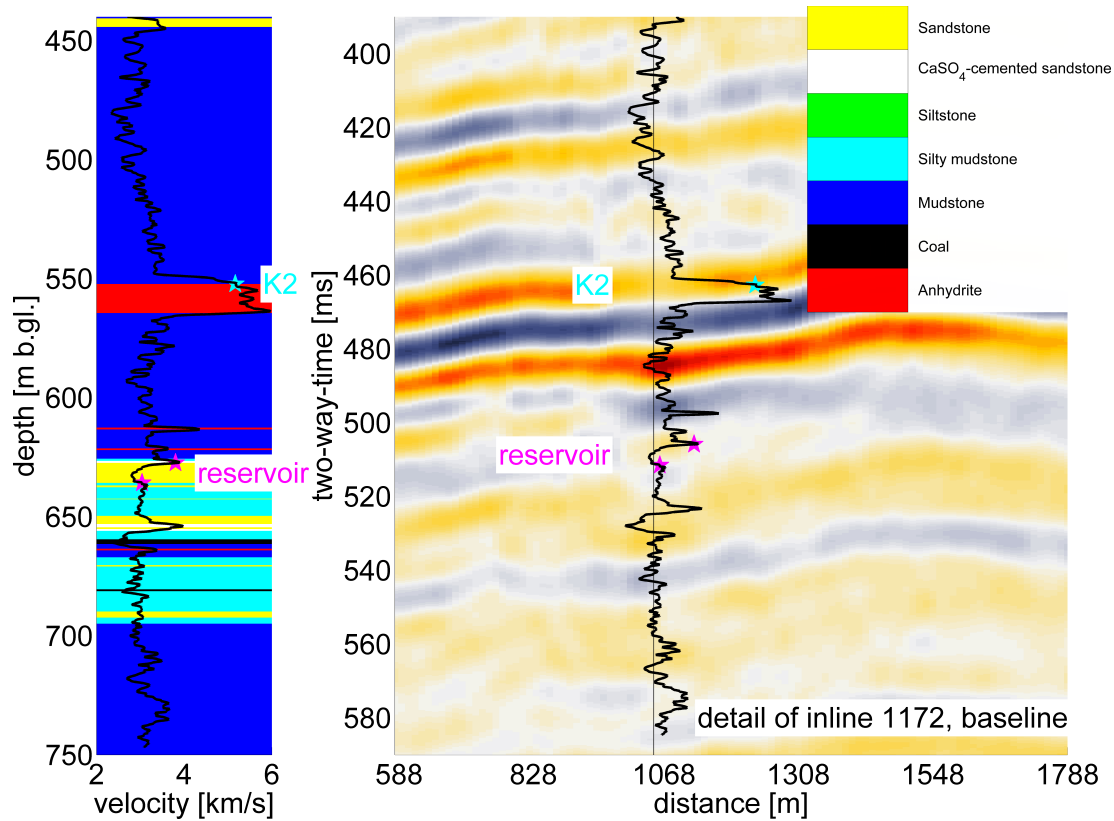


Figure 5.14: Depth-to-time conversion of sonic log Ktzi 202. Left: 10-point median filtered sonic log of Ktzi 202 in depth with the lithology of Ktzi 202 (Chap. 2.4.3). The depth is in meter below ground level [m b.gl.]. Right: Detail of the inline 1172 of 3D surface seismic baseline. At the intersection between inline 1172 and observation well Ktzi 202 (Fig. 1.2), the depth to two-way-time converted sonic log is shown. Left and right: The stars mark the positions of the K2 (cyan), the top and the bottom of the reservoir (magenta).

## 5.8.2 Band limited impedance inversion

Since the zero-offset VSP was measured in Ktzi 202 (Chap. 5.3), the band limited impedance inversion is based on the sonic and density logs of Ktzi 202 (Chap. 2.4.3) and calculated for inline 1172, crossing this observation well.

To derive the velocity change within the reservoir the impedances of the zero-offset VSP data are calculated with the band limited impedance inversion (BLIMP) by Ferguson and Margrave (1996) (Chap. 3.4). MATLAB scripts for this algorithm are part of a seismic MATLAB package by CREWES (2012).

As input for the inversion an acoustic impedance log has to be derived from sonic and density logs. Figure 5.15 shows the P-wave  $v_p$  sonic log (left) and density  $\rho$  log (middle) of Ktzi 202 (Chap. 2.4.3). Both logs are median filtered (10-point filter) and converted from depth to two-way-time (TWT) using the function derived in Chapter 5.8.1 (Fig. 5.14). On the right of Figure 5.15 the acoustic impedance  $z$  log derived from sonic and density log ( $z = \rho \cdot v_p$ ) is shown.

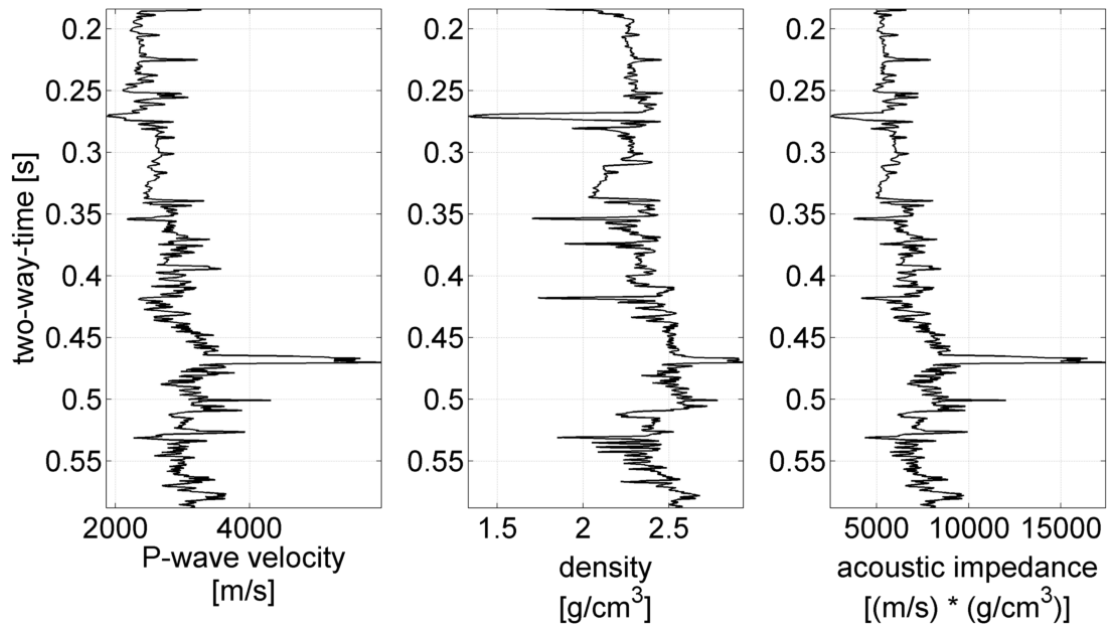


Figure 5.15: Acoustic impedance log  $z$  (right) derived from sonic and density logs (left and middle) of Ktzi 202 (Chap. 2.4.3). The sonic and density logs are median filtered and converted from depth to two-way-time. Right: Acoustic impedance log derived from sonic and density log. Since the location of the K2 of the 3D surface seismic varies in time, the two-way-time function is shifted to the K2 for each trace. Here, as an example, the adjustment to the stacked zero-offset VSP baseline is shown (Figure 5.12, top left image).

As explained in Chap. 2.4.3 the sonic log is tied to the 3D surface seismic by shifting the TWT function to the upper trough of the strong double reflection of the K2 (Juhlin et al. (2007)). Since the location of the K2 varies in time, the TWT function is shifted to the K2 for each trace. This means the relative two-way-time, the velocity and density is kept constant, but their location in time is adjusted to the location of the K2 for every trace.

To run the BLIMP script, the seismic trace, its time coordinate vector and the impedance log in time (Fig. 5.15) is needed. The low and high pass frequencies are set to 20 Hz and 90 Hz, the Gaussian roll-off is set to 10 Hz (Chap. 3.4). Figure 5.16 shows the result of the band limited impedance inversion of the inline 1172 converted to P-wave velocities (Eq. 3.17). The stacked traces of the zero-offset VSP data (measured and modelled) are plotted side by side and inserted at the intersection of inline 1172 with the well. Figure 5.16 shows from top to bottom baseline, repeat and difference (repeat minus baseline) in percent of the baseline velocity of 3D surface seismic and VSP. The VSP data of the left column is bandpass filtered with corner frequencies of 10-20-80-100 Hz. For a better comparison with the 3D surface seismic the VSP data of the right column is bandpass filtered with corner frequencies of 10-20-50-70 Hz. The black lines in Figure 5.16 mark the positions of the K2 (upper line), the top and bottom of the reservoir (middle and bottom line). The seismic sections corresponding to this velocity section are shown in Figure 5.12.

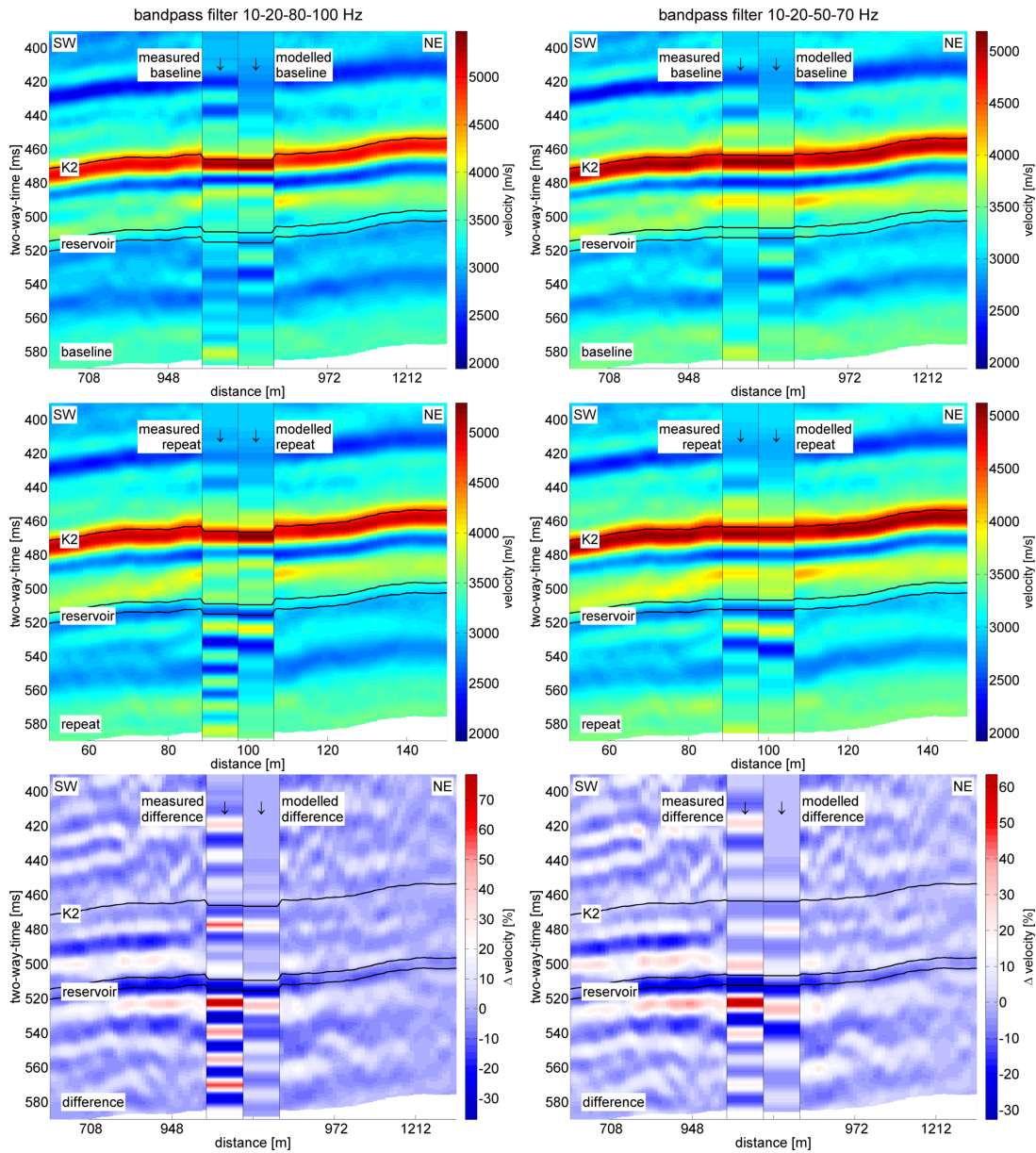


Figure 5.16: Result of the band-limited impedance inversion of the inline 1172 converted to P-wave velocities. The stacked traces of the zero-offset VSP data (measured and modelled) are plotted side by side and inserted at the intersection of inline 1172 with the well. From top to bottom baseline, repeat and difference (repeat minus baseline) in percent of the baseline velocity of 3D surface seismic and VSP. The VSP data of the left column is bandpass filtered with corner frequencies of 10-20-80-100 Hz, the VSP data of the right column is bandpass filtered with corner frequencies of 10-20-50-70 Hz. The black lines mark the positions of the K2 (upper line), the top and bottom of the reservoir (middle and bottom line).

The general velocity structure is correctly inverted, e.g. the P-wave velocity of the K2 is 5500 m/s, the baseline velocity within the reservoir is 3000 m/s (Fig. 5.16, top row). Using the band limited impedance inversion it was not possible to resolve all thin layers evident on the well logs (Fig. 5.14). The K2 reflector is compressed to a single high velocity layer, but still accompanied by a low velocity oscillation. The reservoir

becomes visible in the repeat data, due to the increased velocity contrast. Resolving the reservoir by band limited impedance inversion was not possible, the wavefield character is still dominating (Fig. 5.16, middle row, Chap. 5.7.4). However, it is possible to gain an estimate of the velocity change within the reservoir (Fig. 5.16, bottom row). The modelled data are based on a velocity reduction of 30 %, after processing and inversion a velocity reduction of 26 % and 21 % was found for the high and low frequency data, respectively. The velocity change at the top of the reservoir is 32 % for the measured data (for both bandpass ranges).

## 5.9 Conclusions

A near-well corridor stack of the zero-offset VSP data is compared to a 3D surface seismic inline:

- **Comparison of zero-offset VSP with 3D surface seismic (Fig. 5.8):** It is possible to identify consistent phases within 3D surface seismic data and zero-offset VSP data. The dynamic range of the amplitudes is comparable for both methods. As in 3D surface seismic the reservoir is not indicated as a clear reflection in the baseline zero-offset VSP data. For the VSP data, this is related to an uncemented part of the single casing string (Fig. 5.3, Chap. 5.4.2). CO<sub>2</sub> induced changes in reflectivity can be observed in the zero-offset VSP repeat data. The amplitudes of 10-20-80-100 Hz bandpass filtered VSP data show a strong amplitude signature, with ringing extending almost 70 ms below the reservoir. When applying a 10-20-50-70 Hz bandpass, the enhanced amplitudes are confined to reservoir depth. More details of the structure below the top of the reservoir are resolved in the zero-offset VSP repeat data than in the 3D surface seismic data.
- **CO<sub>2</sub> signature of measured and modelled zero-offset VSP (Fig. 5.12):** The dynamic range of modelled zero-offset VSP amplitudes is comparable to the measured amplitudes. Contrary to 3D surface seismic and measured zero-offset VSP, the reservoir is indicated as a reflection (positive amplitude) in the modelled baseline data. The reservoir becomes visible in the modelled repeat data, due to the increased velocity contrast. Phases and amplitudes of measured and modelled repeat are in good agreement besides a slight shift below the reservoir. Within the difference sections a clear signature caused by the injection of CO<sub>2</sub> is visible. Above the reservoir weak amplitude artefacts are still visible in the measured data. The top of the reservoir is characterised by a positive amplitude difference. This is consistent with the 3D surface seismic data. With closer look at the wavefield one can observe a positive amplitude at the top of the reservoir, followed by negative amplitude and again a positive amplitude. Within the high frequency data the difference is dominated by the ringing of the repeat, but the bandpass filtered zero-offset VSP difference shows good correlation with the modelled VSP difference.

Based on the CO<sub>2</sub> induced changes in normal incidence reflectivity, the thickness of the CO<sub>2</sub> plume and the reduction of P-wave velocity are calculated. The latter can be used to calculate the CO<sub>2</sub> saturation in the reservoir.

- **Estimation of CO<sub>2</sub> layer thickness from zero-offset VSP data (Fig. 5.13):** A wedge modelling study was performed to investigate the wavefield of the reservoir reflection. The reservoir is not resolved as separate reflection events, the wavefield is characterised by the interference of reflections from top and bottom of the reservoir (positive - negative - positive). With reducing the reservoir layer thickness,

interference tuning can be observed. When comparing both, the shape and the amplitude of the measured and modelled zero-offset VSP, the CO<sub>2</sub> layer thickness is estimated with 6 m. It is possible that at the time of the zero-offset VSP repeat, the reservoir layer was not totally influenced by the CO<sub>2</sub> plume, but only the uppermost 6 m.

- **Band limited impedance inversion of zero-offset VSP data (Fig. 5.16):** The general velocity structure is correctly inverted, e.g. the P-wave velocity of the K2 is 5500 m/s, the baseline velocity within the reservoir is 3000 m/s. Using the band limited impedance inversion, it was not possible to resolve all thin layers evident on the well logs. The K2 reflector is compressed to a single high velocity layer, but still accompanied by a low velocity oscillation. The reservoir becomes visible in the repeat data, due to the increased velocity contrast. Resolving the top and bottom of the reservoir by band limited impedance inversion was not possible, the wavefield character is still dominating. It is possible to gain an estimate of the velocity change within the reservoir. The modelled data are based on a velocity reduction of 30 %, after processing and inversion a velocity reduction of 26 % and 21 % was found for the high and low frequency data, respectively. The velocity reduction at the top of the reservoir is 32 % for the measured data (for both bandpass ranges).

# 6 Chapter 6

---

## 6 Offset VSP: baseline and repeat

*This chapter is about the offset VSP baseline and repeat measurements in Ketzin. The main focus of the chapter is imaging with Kirchhoff and Fresnel pre-stack depth migration.*

### 6.1 Motivation and research objectives

The offset VSP baseline and repeat measurements were acquired together with the zero-offset VSP (Chap. 5) in 2007 and 2011 (45770 t CO<sub>2</sub> injected). Both acquisition geometries generate high-resolution seismic images and can monitor CO<sub>2</sub> injection into a water saturated reservoir, by mapping the increased reflectivity from top of the reservoir. While the zero-offset VSP focuses on normal incidence reflectivity near the observation well, offset VSP has the potential to generate a lateral image of the reservoir at the injection site. Two migration algorithms are compared for measured and modelled data to evaluate their influence on the imaging of the data.

### 6.2 Equipment and recording parameters

*The offset VSP was recorded in the observation well Ktzi 202 (Fig. 2.4). Recording and pre-processing (shift-and-stack, Chap. 3.1) was done by Vibrometric Oy, Finland.*

**Lubricator, access to pressurized wells:** Just as for the crosshole (Chap. 4.2) and zero-offset VSP measurements (Chap. 5.2) a lubricator is needed to access the Ktzi 202 well during the repeat measurement after the breakthrough of CO<sub>2</sub>.

Recording and pre-processing (shift-and-stack, Chap. 3.1) was done by Vibrometric Oy, Finland. The sources and receivers used for the offset VSP are the same as used for the zero-offset VSP: the VIBSIST-1000 and VIBSIST-3000 source (for baseline and repeat, respectively) and the 3-component RD-XYZ-cg receiver chain (Chap. 5.2).

**Recording parameters:** For baseline and repeat, 80 traces per component (2 horizontal, 1 vertical) with a sample rate of 0.25 ms and a length of 2499.75 ms (baseline) and 2047.75 ms (repeat) have been recorded. The sample frequency for both measurements is 4000 Hz, what leads to the Nyquist frequency of  $f_{Ny} = \frac{1}{2}f_{sample} = 2000$  Hz.

### 6.3 Measurement geometry

The offset VSP was recorded in the Ktzi 202 well between 325 - 720 m below ground level, at 5 m depth intervals (80 levels). Source point 4 (Fig. 6.1) was recorded with the upper 62 levels only. 2D surface seismic (Bergmann et al. (2010, 2011); Ivandic et al. (2012)) and Moving Source Profiling (Yang et al. (2010); Lüth et al. (2011)) measurements were performed in Ketzin, where seven seismic lines had a star shaped geometry around the injection site. The source points of the offset VSP are located at the far end and in the middle of each of these seven lines. Only source points located in the middle of the line will be considered in the following, since data of the more distant locations is affected by noise and most of the seismic energy is refracted from the seismically fast K2 anhydrite layer (Chap. 2.1, Chap. 2.4.3).

Figure 6.1 shows the layout of the employed offset VSP source points with the normalised amplitude difference (repeat minus baseline) of 3D surface seismic at the reservoir horizon (top of Stuttgart Formation, Ivandic et al. (2012)). The difference is the result of time-lapse processing of the baseline and repeat surveys, which were measured autumn 2005 and autumn 2009, respectively. At the time of the repeat survey 22 - 25 kt have been injected. The CO<sub>2</sub> is visible in the difference map as strong amplitudes at the time interval of the reservoir. The red dots mark the position of the offset VSP source points, the black lines link the source points with the receiver well Ktzi 202 and indicate the imaging planes. Table 6.1 lists the source point coordinates and offsets as horizontal distances from the Ktzi 202 well.

The imaging plane of source point number 7 is crossing through the amplitude difference, therefore this source point is the most likely one to monitor CO<sub>2</sub>. When comparing the offset VSP and the 3D surface seismic difference, one has to bear in mind that the associated repeat measurements were measured at different times. The 3D surface seismic repeat was measured in autumn 2009 with 22 - 25 kt of CO<sub>2</sub> injected, whereas the offset VSP was repeated in February 2011 with ~ 46 kt of CO<sub>2</sub> injected (Figure 1.3).

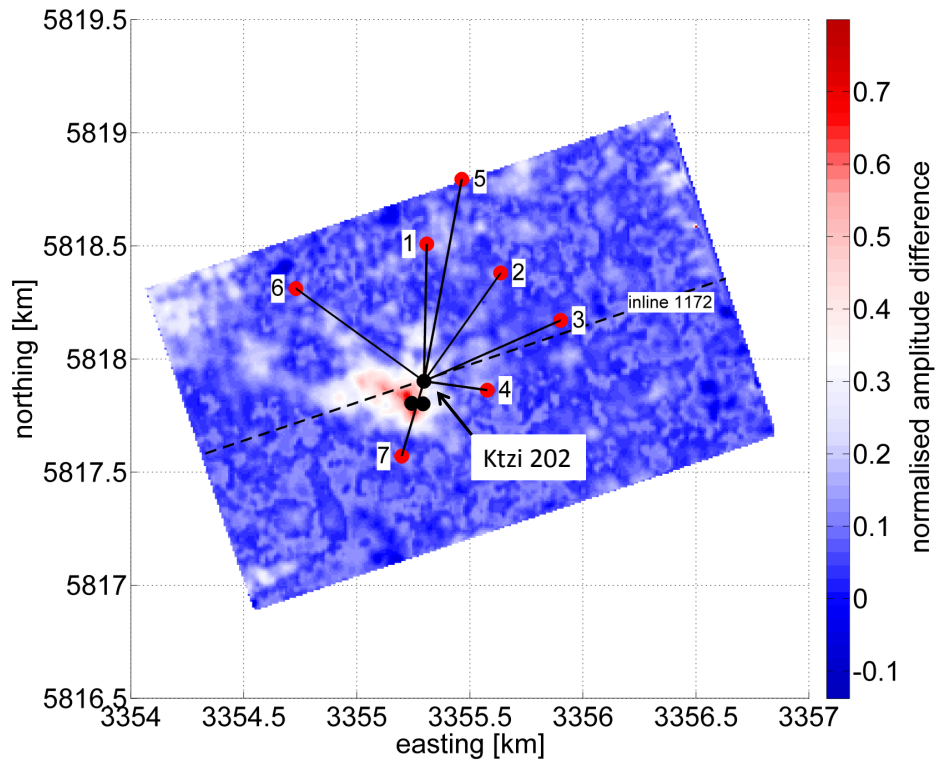


Figure 6.1: Layout of the employed offset VSP source points with the normalised amplitude difference (repeat minus baseline) of 3D surface seismic at the reservoir horizon (top of Stuttgart Formation, Ivandic et al. (2012)). The difference is the result of time-lapse processing of the baseline and repeat surveys, which were measured autumn 2005 and autumn 2009, respectively. The red dots mark the position of the offset VSP source points. The Ketzin wells are marked as black dots. The black lines link the source points with the receiver well Ktzi 202 and indicate the imaging planes. Inline 1172, which is crossing the observation well Ktzi 202 is plotted as dashed line.

Table 6.1: Offset VSP, coordinates and elevations of the employed source points. The elevation is in meter above sea level [m a.sl.], the offsets are the horizontal distances between the Ktzi 202 well and the source points.

source point	UTM easting [m]	UTM northing [m]	elevation [m a.sl.]	offset [m]
1	(33) 355 308.98	5 818 507.88	32.31	606.0
2	(33) 355 636.11	5 818 379.97	34.77	585.5
3	(33) 355 901.04	5 818 170.52	35.99	660.1
4	(33) 355 576.62	5 817 861.98	34.42	281.5
5	(33) 355 464.07	5 818 793.84	33.27	907.1
6	(33) 354 729.96	5 818 310.92	37.66	699.9
7	(33) 355 198.36	5 817 570.40	34.20	346.2

## 6.4 Offset VSP processing

The vertical component of the offset VSP data is processed with CLARITAS (bulk static shift, killing of noisy traces) and RadExPro (all other processing steps). The processing is shown exemplary for source point number seven, whose imaging plane is crossing the CO<sub>2</sub> plume (Fig. 6.1). The processing of the offset VSP data is divided into five steps:

**Step (1):** A bulk static upward shift is applied to compensate for source delays (baseline 25 ms, repeat 50 ms). The polarity of the traces is reversed for baseline and repeat, to set the first break amplitude positive. The trace length of the baseline is cut to 2047.75 ms to make both measurements the same length. Figure 6.2 (top row) shows baseline and repeat data after processing step 1. An upgoing reflection from the K2 anhydrite layer can be observed in the measured baseline and repeat data (Fig. 6.2, red lines).

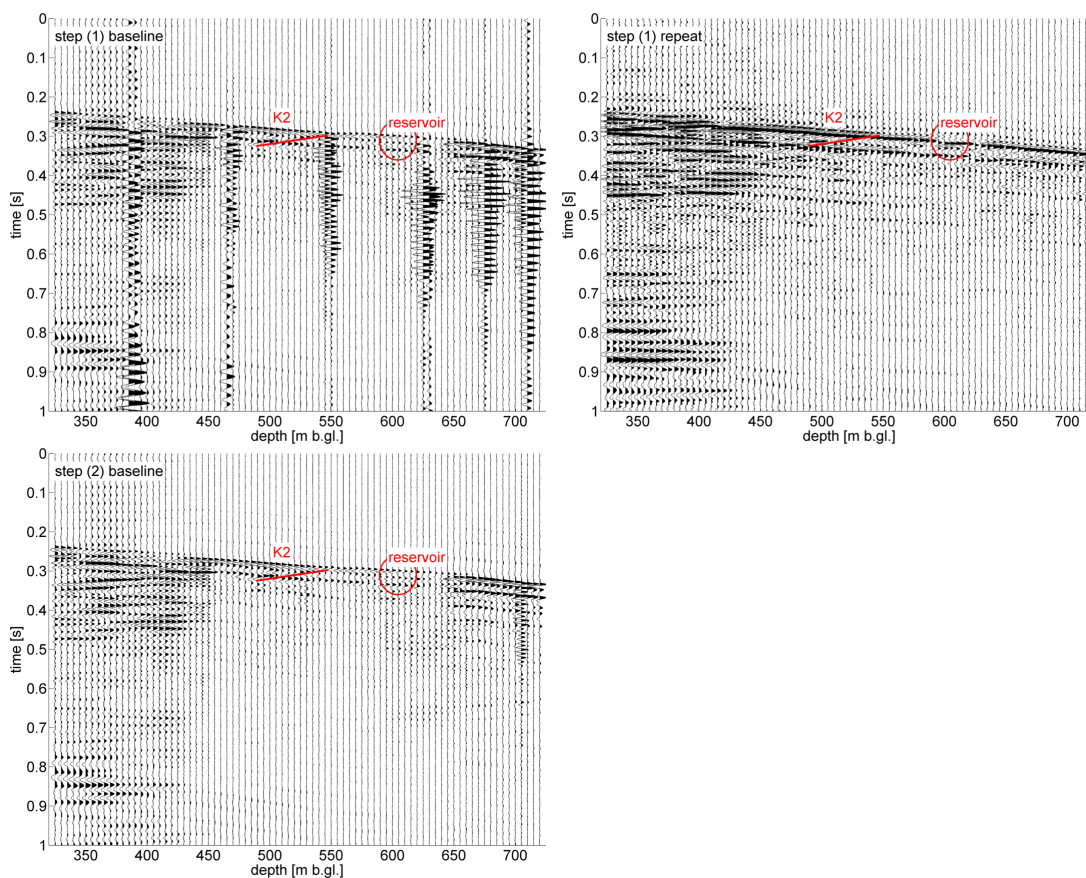


Figure 6.2: Processing of offset VSP, source point 7, vertical component. The left column shows baseline data, the right column repeat data. Top row, step (1): data after trace flip and bulk static shifts. Bottom row, step (2): data of the baseline after trace kill (Tab. 6.2) and interpolation. Upgoing reflections from the K2 anhydrite layer (red lines) and the depth of the reservoir (red circle) are indicated. The depth is in meter below ground level [m b.gl.].

**Step (2):** Noisy traces are totally removed (killed, Table 6.2) and the gaps are filled by trace interpolation. Two live traces are being used to fit the interpolated traces in a least squares polynomial fit. The maximum order of the polynomial fit is set to 1. A

list of the killed traces can be found in Table 6.2. Figure 6.2 (bottom row) shows the baseline data after the removal of noisy traces.

Table 6.2: Offset VSP processing, list of the killed traces.

source point	measurement	trace numbers
1	repeat	40, 75
2	baseline	15, 28
4	baseline	1, 3, 5, 7, 9, 11, 13, 14, 15, 29, 30, 45, 46, 61
7	baseline	13, 14, 29, 30, 45, 46, 61, 62, 71, 78

**Step (3):** The repeat traces are matched to the baseline traces by application of a cross-correlation time-shift (Bergmann et al. (2011)): First, the sampling rate of baseline and repeat data is increased to 0.1 ms to allow a finely resolved cross-correlation time-shift of the repeat data. The trace length is cut to 600 ms and an ensemble equalisation is applied. Then, the cross-correlation of baseline and repeat traces is calculated. Finally, the time-shift between the maximum of the cross-correlation and zero-lag is applied to the repeat data. The cross-correlation between baseline and repeat traces is shown in Figure 6.3 (top row). The green dots mark the zero-lag (300 ms), the red dots mark the picked maximum of the cross-correlation. On the right side, the cross-correlation of baseline and repeat traces after the application of the time-shift to the repeat data is shown. The maximum is now aligned at zero-lag. The bottom row of Figure 6.3 displays the vertical component of the repeat before and after the application of the time-shift (left and right, respectively).

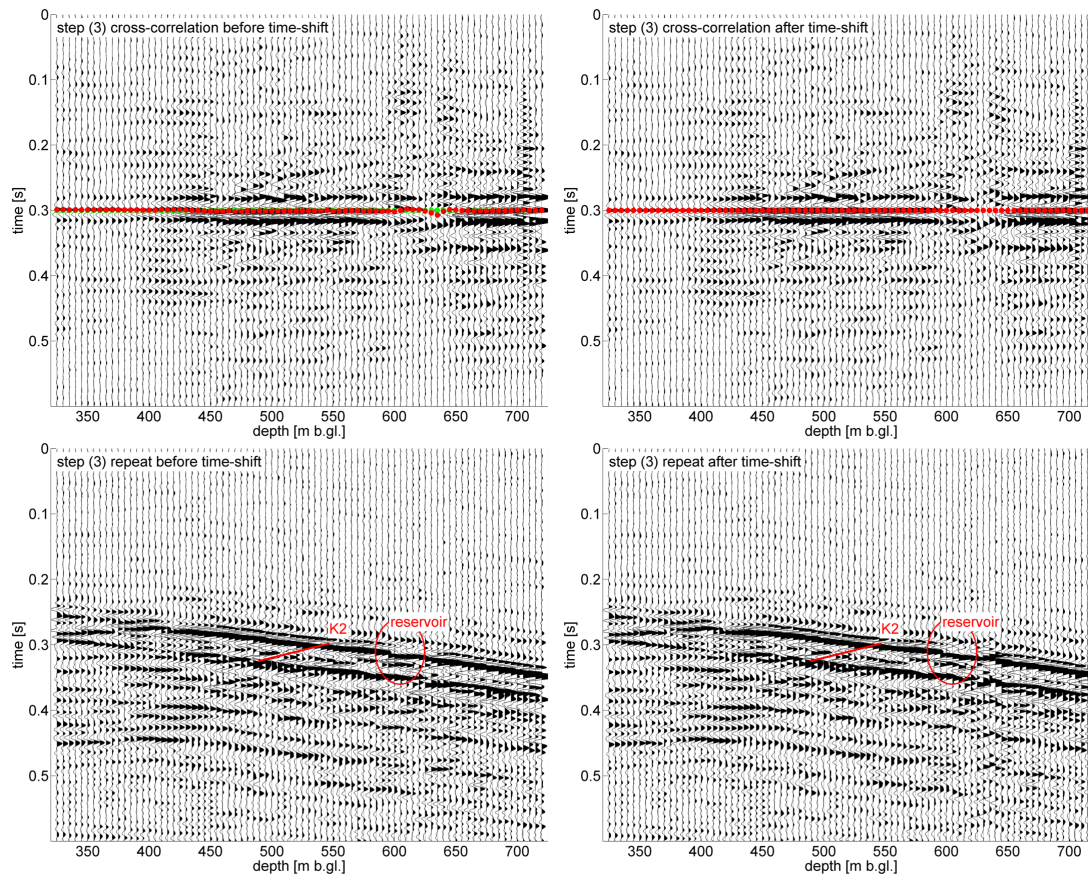


Figure 6.3: Processing of offset VSP, source point 7, vertical component. Top row left: cross-correlation of baseline and repeat traces. The green dots mark the zero-lag (300 ms), the red dots mark the picked maximum of the cross-correlation. Top row right: cross-correlation of baseline and repeat traces after the application of the time-shift to the repeat data. The maximum is now aligned at zero-lag. Bottom row: the vertical component of the repeat is shown before and after the application of the time-shift (left and right). Upgoing reflections from the K2 anhydrite layer (red lines) and the depth of the reservoir (red circle) are indicated. The depth is in meter below ground level [m b.gl.].

**Step (4):** The next step is the application of a fk-filter to extract the upgoing wavefield. Here the fk-filter is chosen to separate the downgoing and upgoing waves, since median filtering is based on the alignment of first breaks, but for some source points the first breaks have upgoing character in the depth range of the K2. So the upgoing (refracted) parts of the K2 would be filtered as well. Figure 6.4 (top) is a screenshot of the RadExPro software, showing the baseline wavefield on the left side and its fk-spectrum on the right side with the right half plane shaded, indicating the area which is cut with a taper window length of 1%.

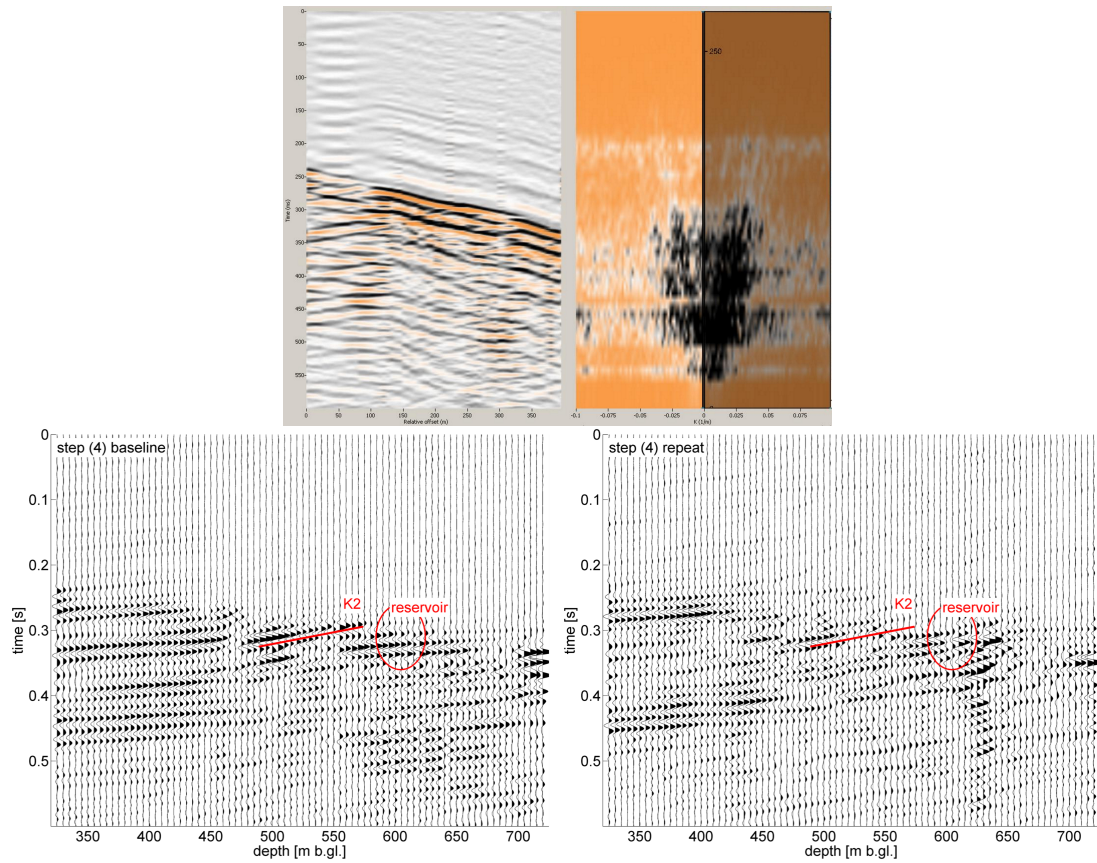


Figure 6.4: Processing of offset VSP, source point 7, vertical component. Top: screenshot showing the baseline wavefield on the left side and its fk-spectrum on the right side with the right half plane shaded, indicating the area which is cut. Bottom: offset VSP, source point 7, vertical component. Upgoing wavefields of baseline (left) and repeat data (right) after fk-filtering and application of a 20-30-80-100 Hz bandpass filter (step (5)). Upgoing reflections from the K2 anhydrite layer (red lines) and the depth of the reservoir (red circles) are indicated. The depth is in meter below ground level [m b.gl.].

**Step (5):** In order to achieve good comparability with the 3D surface seismic data an Ormsby bandpass or spectral whitening together with an AGC was applied to the upgoing wavefield. Table 6.3 gives an overview of the applied filters and their corner frequencies. Figure 6.4 (bottom) shows the upgoing wavefield of source point 7 (baseline and repeat) after fk-filtering and the application of a 20-30-80-100 Hz bandpass filter. The upgoing wavefields after processing step (5) are used for the Kirchhoff and Fresnel depth migrations (Chap. 6.6).

Table 6.3: Offset VSP processing, application of Ormsby bandpass or spectral whitening with AGC.

source point	Ormsby bandpass corner frequencies [Hz]	spectral whitening corner frequencies [Hz]	AGC length [ms]
1	-	20 - 40 - 125 - 150	600
2	-	20 - 40 - 125 - 150	600
3	-	20 - 40 - 125 - 150	600
4	20 - 30 - 80 - 100	-	-
5	30 - 60 - 100 - 150	-	-
6	-	20 - 40 - 125 - 150	600
7	20 - 30 - 80 - 100	-	-

## 6.5 Time-to-depth conversion of 3D surface seismic

The 3D surface seismic in depth is needed for the comparison with depth-migrated offset VSP data (Chap. 6.6.3). For the depth-migration of VSP data (Chap. 6.6) an interval velocity model is derived from 3D surface seismic rms-velocities. Since the time-to-depth conversion of 3D surface seismic is based on the same velocity model it serves as an indication for the quality of the velocity model.

### 6.5.1 3D surface seismic rms-velocities to interval velocities

The velocity models for the depth migration of the seven offset VSP source points are based on 3D surface seismic interval velocities, derived from rms-velocities. The 3D surface seismic cubes (Juhlin et al. (2007), Ivanova et al. (2012)) are converted from time domain to depth domain with the seismic processing software CLARITAS, using rms-velocities derived for the baseline data.

Since smooth velocities are needed for migration, before conversion to interval velocities, the rms-velocities are smoothed by a running average with equal weights over 10 grid points in inline and crossline direction (trace mixing). The interval velocities are calculated with the Dix formula, and converted into depth domain. For the 2D Fresnel migration (Chap. 6.6) the 3D interval velocity cube is sliced along the imaging planes of the seven offset VSP source points (Fig. 6.5). The velocity model does not include the K2 reflector as a high velocity layer (Chap. 2.4.3), but as a smooth zone of increased velocities of 3300 m/s at  $\sim 550$  m depth.

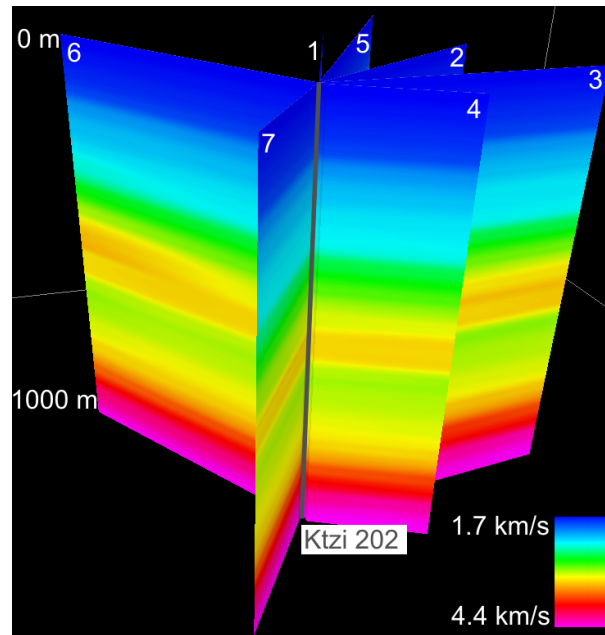


Figure 6.5: 2D interval velocities derived from the 3D surface seismic rms-velocities. The 3D interval velocity cube is sliced along the imaging planes of the seven offset VSP source points located at the outer ends of the planes labelled from 1 to 7.

### 6.5.2 Time-to-depth conversion of 3D surface seismic

The time-to-depth converted 3D surface seismic will be shown as an example for inline 1172, which intersects the observation well Ktzi 202. The left column of Figure 6.6 shows a detail of inline 1172 in depth for baseline (top) and difference (repeat minus baseline, bottom). At the intersection between inline 1172 and observation well Ktzi 202 (Fig. 6.1), the sonic log of Ktzi 202 is shown. The depth of the sonic log and the 3D surface seismic is in meter below datum (30 m above sea level, Juhlin et al. (2007)). For comparison, the same traces in time domain are shown in the right column of Figure 6.6 with the depth to two-way-time converted sonic log (Chap. 5.8.1). The position of the K2 coincides within the depth converted 3D surface seismic and the sonic log (Fig. 6.6, left column, top). This evidence the correct depth conversion of the 3D surface seismic. In the difference section (Fig. 6.6, left column, bottom) the position of the reservoir is shifted compared to the reservoir within the time domain (Fig. 6.6, right column, bottom). This is caused by the applied rms-velocity model, which is coarse, and might lead to this slight mispositioning.

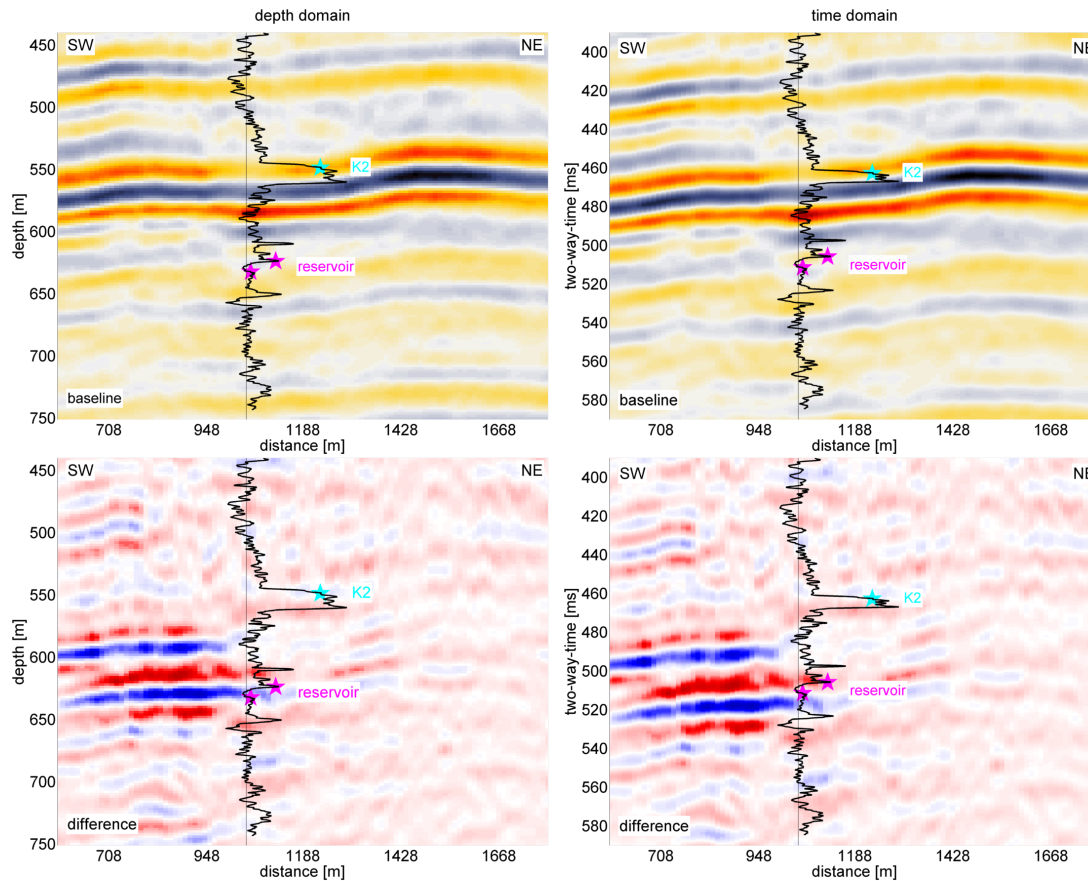


Figure 6.6: Time-to-depth conversion of 3D surface seismic. Left column: time-to-depth converted detail of inline 1172 for baseline (top) and difference (repeat minus baseline bottom). At the intersection between inline 1172 and observation well Ktzi 202, the sonic log of Ktzi 202 is shown. The depth of the sonic log and the 3D surface seismic is in meter below datum (30 m above sea level, Juhlin et al. (2007)). For comparison, the same traces in time domain are shown in the right column with the depth to two-way-time converted sonic log (Chap. 5.8.1). The stars mark the positions of the K2 (cyan), the top and the bottom of the reservoir (magenta) in the sonic log.

## 6.6 Kirchhoff and Fresnel depth migration

*Two migration algorithms are compared: The first algorithm is the "2D-3D VSP Migration" module of RadExPro which performs Kirchhoff migration of VSP seismograms (Dillon (1990)). The second algorithm is an own implementation of a 2D Fresnel migration, where the Fresnel zone is considered when mapping the amplitudes.*

### 6.6.1 Kirchhoff migration

The 2D VSP migration module of RadExPro performs Kirchhoff depth-migration of VSP data (Dillon (1990)). "The input of the module is a VSP seismogram passing through the processing flow with separated non-converted reflected wavefields (Chap. 6.4). The migration method is based on a horizontally layered model and does not take lateral velocity changes into account" (DECO Geophysical Software Company (2013)).

Therefore, the mean of the 2D interval velocities (Fig. 6.5) is calculated. Figure 6.7 shows the employed velocity models for source points 1 to 7 as red lines. For comparison the sonic log of Ktzi 202 is shown in black. The thickness of the layers in the velocity model is set to 50 m. The velocity models for the Kirchhoff migration need to be adjusted, in order to align the position of the K2 within the depth migrated VSP and the depth converted 3D surface seismic. The adjustment is made by subtracting a constant velocity from the 1D interval velocity models (Fig. 6.7). Table 6.4 gives an overview of the employed velocity shifts. One exception is made for source point 5, which has the largest offset (907 m, Table 6.1), where best migration results are obtained when using a constant velocity of 2360 m/s.

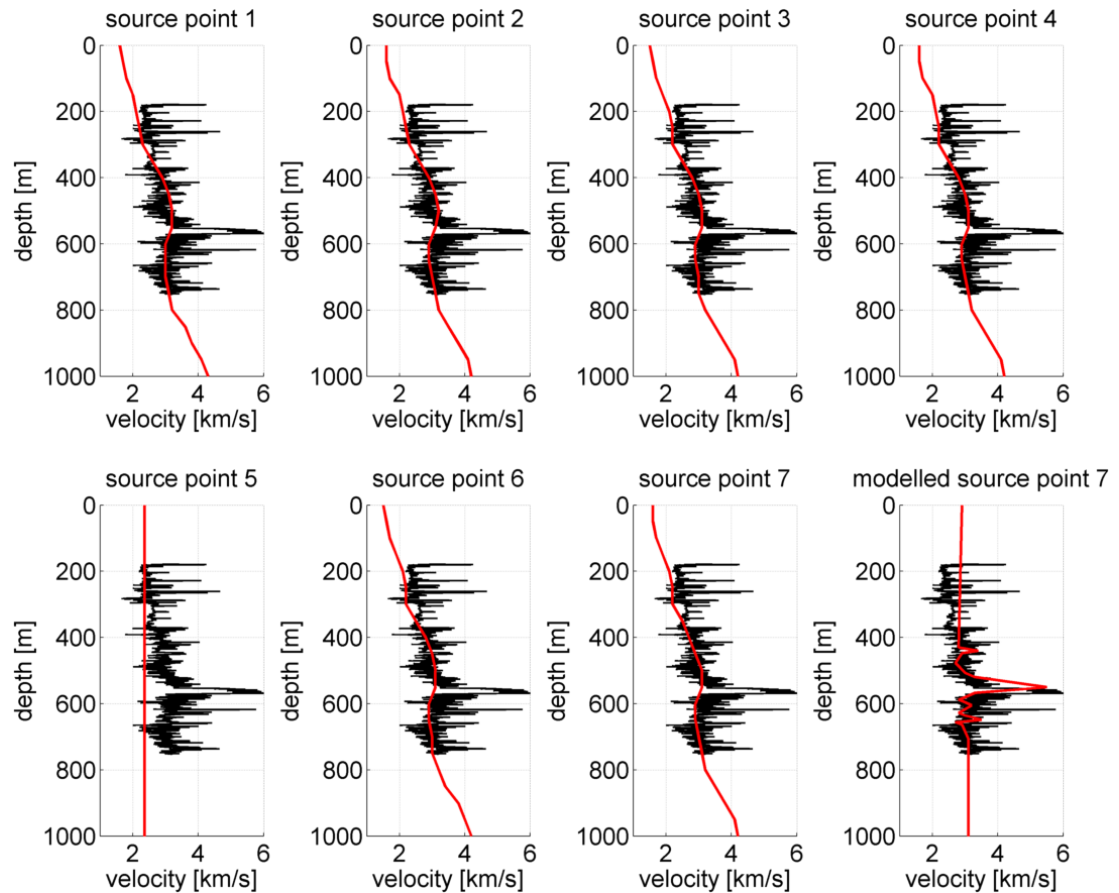


Figure 6.7: 1D interval velocity models for the Kirchhoff depth-migration of source points 1 to 7 and modelled source point 7 (Chap. 6.7) as red lines. The velocity models are adjusted by a constant velocity shift to align the position of the K2 within the depth migrated VSP and the depth converted 3D surface seismic (Tab. 6.4). The migration of the modelled source point, is done with the input velocities used for modelling (with the optimum velocity model). For comparison the sonic log of Ktzi 202 is shown in black.

Table 6.4: Velocity shifts used to align the position of the K2 within the depth migrated VSP and the depth converted 3D surface seismic. One exception is made for source point 5, which has the largest offset (907 m, Table 6.1), where best migration results are obtained, when using a constant velocity of 2360 m/s.

point	Kirchhoff migration shift [m/s]	Fresnel migration shift [m/s]
1	-100	-50
2	-135	-75
3	-175	-125
4	-155	-85
5	$v_{const} = 2360$ m/s	$v_{const} = 2360$ m/s
6	-175	-125
7	-150	-100

The imaging planes are vertically restricted between 0 m and 1000 m depth and horizontally between the source location and the well location (Tables 2.1 and 6.1). The sampling interval is set to 2 m in vertical direction and to 1 m in horizontal direction with a spline interpolation. The wavelet shaping for 2D Kirchhoff migration is set to a 45° constant-phase spectrum and an amplitude spectrum proportional to the square root of the 2D migration frequency (Yilmaz (2000)). The filter for the expected dip moveout is specified by the boundary slope (expected angle) and slope range (angle range). Table 6.5 gives an overview of the values employed for boundary slope and slope range.

Table 6.5: Values for boundary slope (expected angle) and slope range (angle range) for the dip moveout filter of the Kirchhoff migration.

point	boundary slope	slope range
1	15°	15°
2	15°	15°
3	6°	6°
4	6°	6°
5	6°	6°
6	6°	6°
7	6°	6°

### 6.6.2 Fresnel migration

*The Fresnel migration is an own implementation of a modified VSP-CDP mapping algorithm, where the Fresnel zone is considered when mapping the amplitudes.*

The VSP-CDP mapping is a well-known algorithm for imaging offset VSP data. The basic idea of the VSP-CDP mapping is explained according to Lazaratos (1993). "Given a source-receiver pair, a trajectory can be defined that links all the possible reflection points for reflections recorded in this trace (Fig. 6.8). For a horizontal reflector at a depth  $z_A$ , the corresponding reflection point is  $A$ , for a horizontal reflector at a depth  $z_B$ , the corresponding reflection point is  $B$ , for a horizontal reflector at a depth  $z_C$ , the corresponding reflection point is  $C$  and so on. The mapping trajectory is defined by linking the possible reflection points for all depths. Once the trajectory is defined, every

sample of this trace is mapped on the reflection point for which the total reflection travel time is equal to the time this sample is recorded. This procedure is repeated for all traces in the gather” (Lazaratos (1993)).

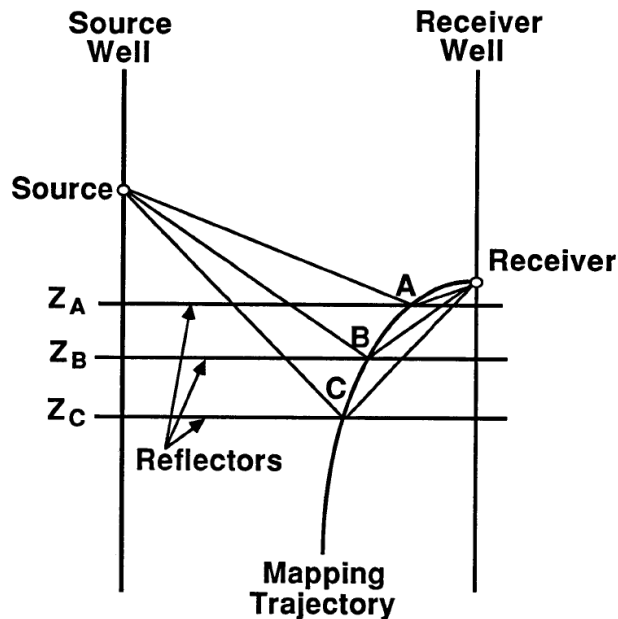


Figure 6.8: Construction of mapping trajectories (Lazaratos (1993)).

The first step of the Fresnel migration is the calculation of VSP-CDP reflection points on 2D interval velocity models without ray tracing. Instead of ray tracing, two-way-time panels are used. "The reflection point on an arbitrarily defined reflection horizon is located where the tangent of the two-way-time isochrone equals the tangent of the reflection horizon" (Schaack (1996)). In the case of a horizontal layer, the position of the reflection point is the deepest point on the isochrone.

As Lazaratos (1993) points out, "VSP-CDP mapping is not a migration algorithm: migration handles correctly all dips while the mapping is accurate only for horizontal layers". Even, if the local dip is known and the algorithm is adjusted to handle the dip, "it can only handle a single dip at a time, while migration can handle a range of dips. The mapping can be considered the limit of migration as the aperture of the migration operator goes to zero. The idea of migration essentially amounts to spreading each data on the appropriate isochrone. It is possible to spread the data over the whole isochrone or on a part of it only. Using only a part of the ellipse means restricting the imaging plane to a range of dips" (Lazaratos (1993)). Within the Fresnel migration a compromise between VSP-CDP mapping and migration is attempted: After the calculation of the reflection points for VSP-CDP mapping, the Fresnel zones of these reflections are calculated. The data is subsequently spread on isochrones  $\pm T/4$  (a quarter of the dominant period  $T$ ) above and below the reflection point, and restricted to the Fresnel zone.

Summarised this means, the main energy is focused on a reflection point based on a horizontal velocity model as in VSP-CDP mapping, but by spreading the energy on isochrones within the Fresnel zone, a certain amount of dip is introduced. In the following the main steps of the Fresnel migration are explained.

**Step (1) Calculation of reflection points:** This is an overview of the main steps for calculating the reflections points:

```

calculate source time panel
loop over receivers
  calculate receiver time panel
  sum source and receiver time panel (= two-way-time panel)
loop over isochrones
  find deepest point on isochrone
  (= depth and offset coordinates of reflection point)
end loop over isochrones
end loop over receivers

```

Based on the 2D interval velocity models (Fig. 6.5), two-way-time panels are calculated for the 80 receivers with the finite-difference eikonal solver of the open source software FAST (First Arrival Seismic Tomography) by Colin Zelt (Zelt and Barton (1998), Chap. 3.3). First, the travel time panels are used to test and adjust the interval velocity model by comparing modelled and measured travel times of direct waves. Figure 6.9 shows the baseline raw data of source point 7, the red dots mark the modelled travel times of the direct waves based on the 2D interval velocity model of source point 7. The interval velocity models are adjusted by subtracting a constant velocity until a good match between modelled and measured travel times is achieved. Table 6.4 gives an overview of the employed velocity shifts. One exception is made for source point 5, which has the largest offset (907 m, Table 6.1), where best migration results are obtained, when using a constant velocity of 2360 m/s.

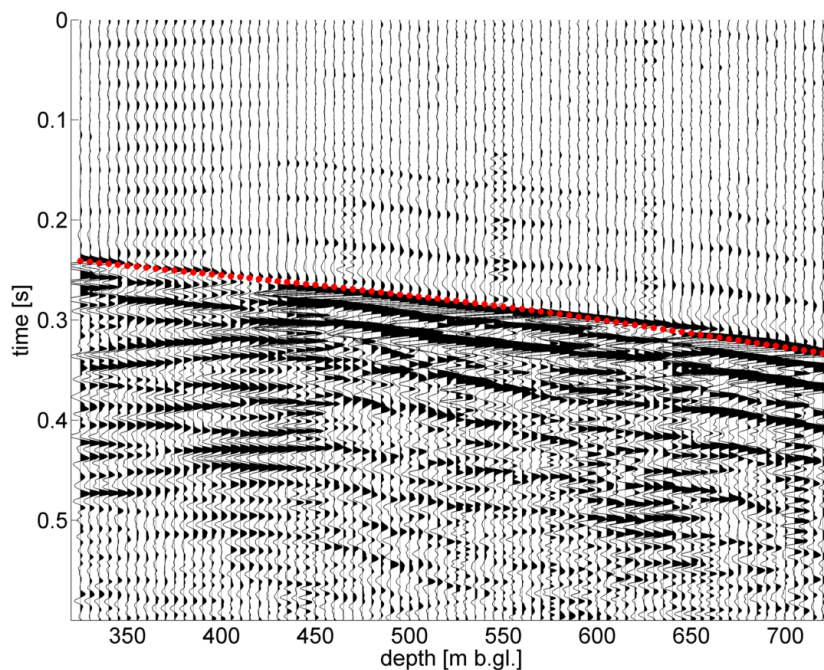


Figure 6.9: Comparison of modelled and measured travel times of direct waves. The baseline raw data of source point 7 is shown. The red dots mark the modelled travel times of the direct waves based on the 2D interval velocity model of source point 7.

After adjusting the velocity models, the two-way-time panels are used to calculate the reflection points. For this purpose, a grid cell size of 1 m for the velocity model is used. According to Schaack (1996) a "reflection point on an arbitrarily defined reflection horizon is located where the tangent of the two-way-time isochrone equals the tangent

of the reflection horizon”. In the case of a horizontal layer, the position of the reflection point is the deepest point on the isochrone. Figure 6.10 shows the interval velocity model of source point 7 on the left side and the corresponding two-way time panel for the 1st receiver on the right side. Only reflection points for every 20th isochrone are calculated, which leads to a depth interval between the reflection points of  $\sim 5$  m. In the case of source point 7, the number of reflection points declines from 170 to 60 between the 1st and 80th receiver. As an example, the reflection points of the 1st receiver are shown as black dots in Figure 6.10.

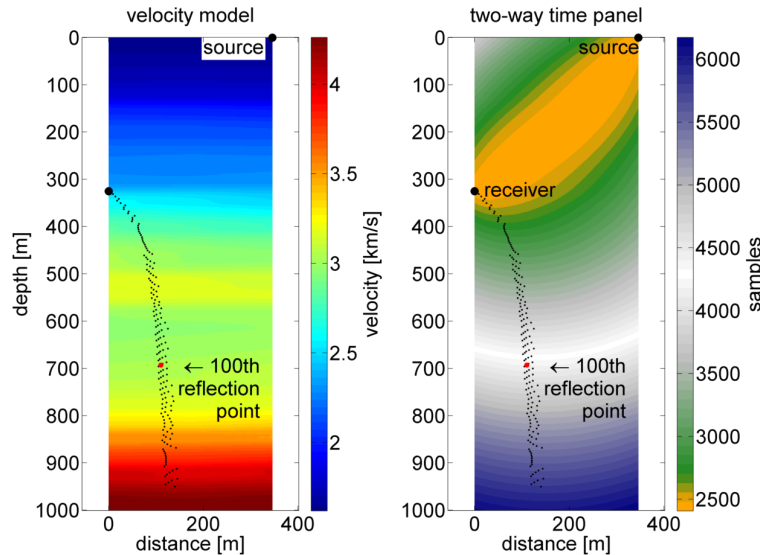


Figure 6.10: Fresnel migration, calculation of reflection points. The interval velocity model (left) and the corresponding two-way time panel for the 1st receiver (right) is shown. The reflection points of the 1st receiver are shown as black dots. The 100th reflection point of the 1st receiver is marked as red dot.

**Step (2) Calculation of Fresnel zones:** The MATLAB script used for the calculation of Fresnel zones is based on the sensitivity kernels of Jensen et al. (2000) (Chap. 3.5) and is part of the mGstat MATLAB package (Hansen (2011)). This is an overview of the main steps for calculating the Fresnel zones:

```

load depth and offset coordinates of reflection points
loop over receivers
  loop over reflection points
    define quadrant between source and reflection point
    mirror velocity model of this quadrant
    calculate source & mirrored source two-way-time panel
    calculate Fresnel zone (source & mirrored source)
    define quadrant between receiver and reflection point
    mirror velocity model of this quadrant
    calculate receiver & mirrored receiver two-way-time panel
    calculate Fresnel zone (receiver & mirrored receiver)
    sum and norm both Fresnel zones
  end loop over reflection points
end loop over receivers

```

Within two loops over the receivers and the reflection points, the Fresnel zone around every reflection point is calculated. The width and shape of the Fresnel zone at the

reflection layer is dependent on the interval velocity model and the propagation of the wave between source, reflection layer and receiver. Here, a grid cell size of 5 m for the velocity model was chosen. First, the quadrant between source and reflection point is defined (Fig. 6.11, left, dashed line). Subsequently, the interval velocity model of this quadrant is mirrored at the reflection point, leading to a mirrored source at the diagonally opposed edge of the model (Fig. 6.11, right).

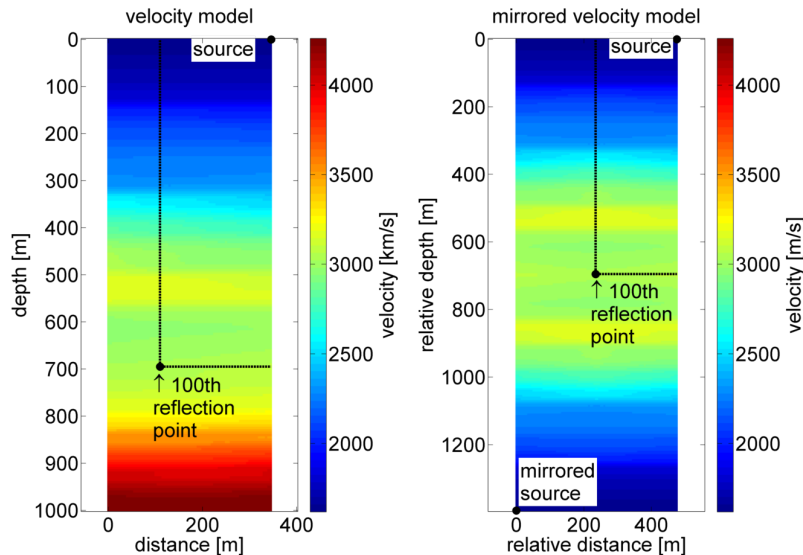


Figure 6.11: Fresnel migration, development of the velocity model for Fresnel zone calculation. Exemplary, the source model for the 100th reflection point of the 1st receiver (Fig. 6.10) is shown. Left: The quadrant between source and reflection point is defined (dashed line). Right: The interval velocity model of this quadrant is mirrored at the reflection point, leading to a mirrored source at the diagonally opposed edge of the model.

A two-way-time panel is calculated for the source and the mirrored source, with the direct wave crossing through the reflection point. Based on this two-way-time panel the delay travel time table is calculated (Eq. 3.18), which is needed before deriving the sensitivity kernel (Eq. 3.20). On the left side of Figure 6.12 the delay travel time panel between source and mirrored source for the 100th reflection point of the 1st receiver (Fig. 6.10) is shown. On the right side of Figure 6.12, the sensitivity kernel for this configuration is displayed. "The region with the highest sensitivity corresponds to the first Fresnel volume, through which the main energy of the wave travels to the receiver around the geometric ray" (Liu et al. (2009)), therefore the sensitivity kernel can be used to monitor the properties of the Fresnel zone (Chap. 3.5, Jensen et al. (2000), Spetzler and Snieder (2004)). When calculating the Fresnel zones, the degree of cancellation in Fresnel zones beyond the first is set to  $\alpha = 1$  (Eq. 3.20). The centre frequency (dominant period  $T$  of the wave, Eq. 3.20) is chosen, according to the employed bandpass or spectral whitening frequencies during processing (Chap. 6.4). Table 6.6 gives an overview over the employed centre frequencies.

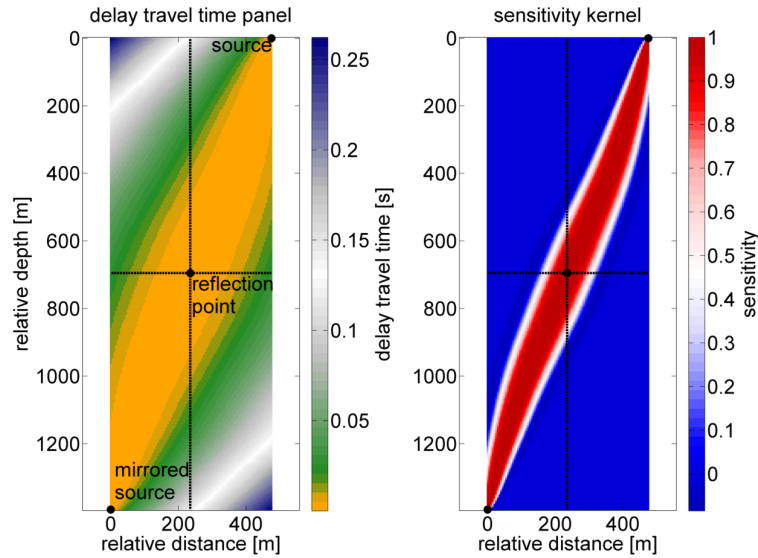


Figure 6.12: Fresnel migration, calculation of Fresnel zones. Left: delay travel time panel (Eq. 3.18) between source and mirrored source for the 100th reflection point of the 1st receiver (Fig. 6.10). Right: sensitivity kernel for this configuration.

Table 6.6: Centre frequencies (dominant period  $T$  of the wave, Eq. 3.20) for the calculation of Fresnel zones.

point	centre frequency [Hz]
1	83
2	83
3	83
4	55
5	80
6	83
7	55

Beginning from the definition of the quadrant, the whole procedure is repeated for the receiver, leading to the Fresnel zone between receiver and reflection point. Both Fresnel zones (from source to reflection point and from receiver to reflection point) are added and normalised leading to the shape of the Fresnel zone at the reflection layer (Fig. 6.13, left).

**Step (3) Migration of the seismic trace:** The migration of the seismic trace is done within the same loop, as the calculation of the Fresnel zones. This is an overview of the main steps for migrating the seismic trace:

```

load depth and offset coordinates of reflection points
loop over receivers
  load two-way-time panel (step 1)
  loop over reflection points
    calculate Fresnel zones
    sum and norm both Fresnel zones
    find isochrones  $\pm T/4$  above & below the reflection point
    spread seismic amplitudes on isochrones
    scale amplitudes according to the values of the Fresnel zone
  end loop over reflection points
end loop over receivers

```

First, within the two-way-time panel (step (1), Fig. 6.10, top row right) isochrones  $\pm T/4$  (a quarter of the dominant period, Table 6.6) above and below the reflection points are determined. Subsequently, the amplitudes of the upgoing wavefield (Chap. 6.4) are spread along the isochrones. Finally, the amplitudes are multiplied by the Fresnel values. Figure 6.13 is an overview of the migration process, exemplary for the 100th reflection point of the 1st receiver of source point 7. On the left the Fresnel zones are shown (step (2)), with the isochrones  $\pm T/4$  above and below the reflection point marked as dots. In the middle, the seismic amplitudes spread along the isochrones and scaled by the Fresnel values are imaged. On the right side a detail of the upgoing baseline wavefield (Fig. 6.4, bottom row left) is plotted. The amplitudes corresponding to the isochrones are marked by a red line.

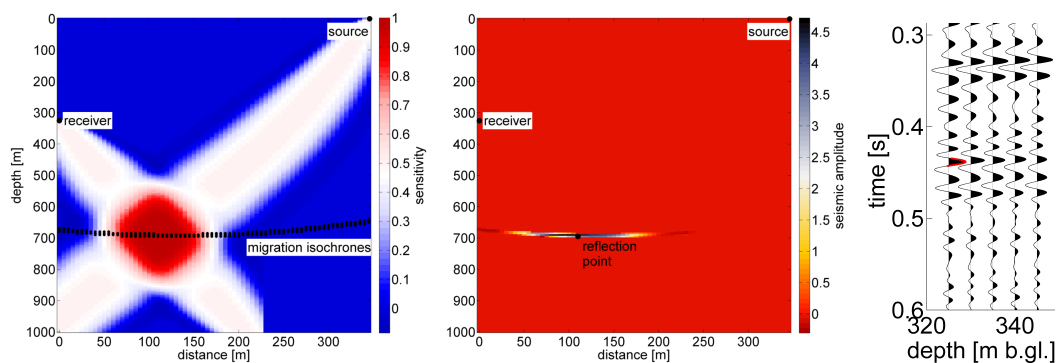


Figure 6.13: Fresnel migration, source point 7, 100th reflection point of the 1st receiver. Left: Fresnel zones of the reflection point (step (2)), with the isochrones  $\pm T/4$  above and below the reflection point marked as dots. Middle: seismic amplitudes spread on the isochrones and multiplied by the Fresnel values. Right: detail of the upgoing baseline wavefield (Fig. 6.4, bottom row left). The amplitudes corresponding to the isochrones are marked by a red line.

Figure 6.14 shows the result of migrating the first receiver of source point 7. As last step, the migration results of single receivers are added to produce the final migrated image of one source point. Before displaying the migration result, the wavelet shaping for 2D Kirchhoff migration is set to a  $45^\circ$  constant-phase spectrum and an amplitude spectrum proportional to the square root of the 2D migration frequency (Yilmaz (2000)). The filter was developed by Bancroft (2008) and is part of a seismic MATLAB package by CREWES (2012).

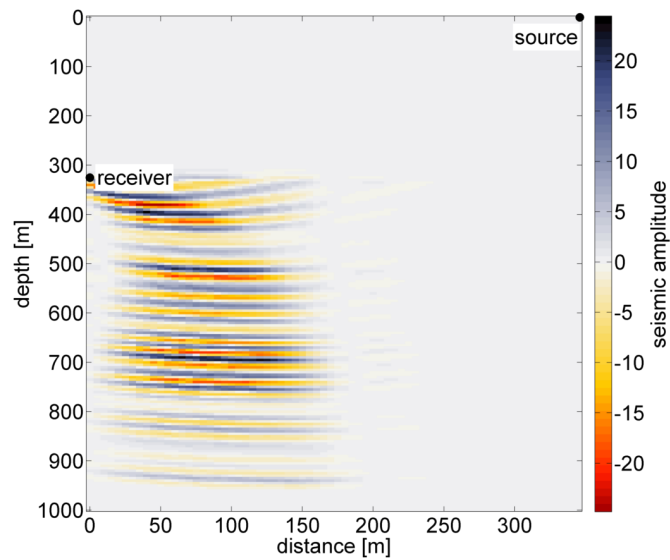


Figure 6.14: Migration result of the first receiver of source point 7.

### 6.6.3 Comparison of Kirchhoff and Fresnel migration results

Figures 6.15 and 6.16 show the results of Kirchhoff and Fresnel migration of source points 7 and 4. Figure 6.15 contains the results of the baseline Kirchhoff migration (top) and Fresnel migration (bottom). The inset explains the geometry of the images: the imaging planes of source point 7 and 4 are unfold at the Ktzi 202 well and the migration results are presented side by side. For comparison the 3D surface seismic baseline, repeat and difference is inserted in the background of Figures 6.15 and 6.16. The locations of source points 7 and 4 are at 0 m depth, 0 m and 650 m distance, respectively. The data sets are normalised to the centre peak of the K2 reflector.

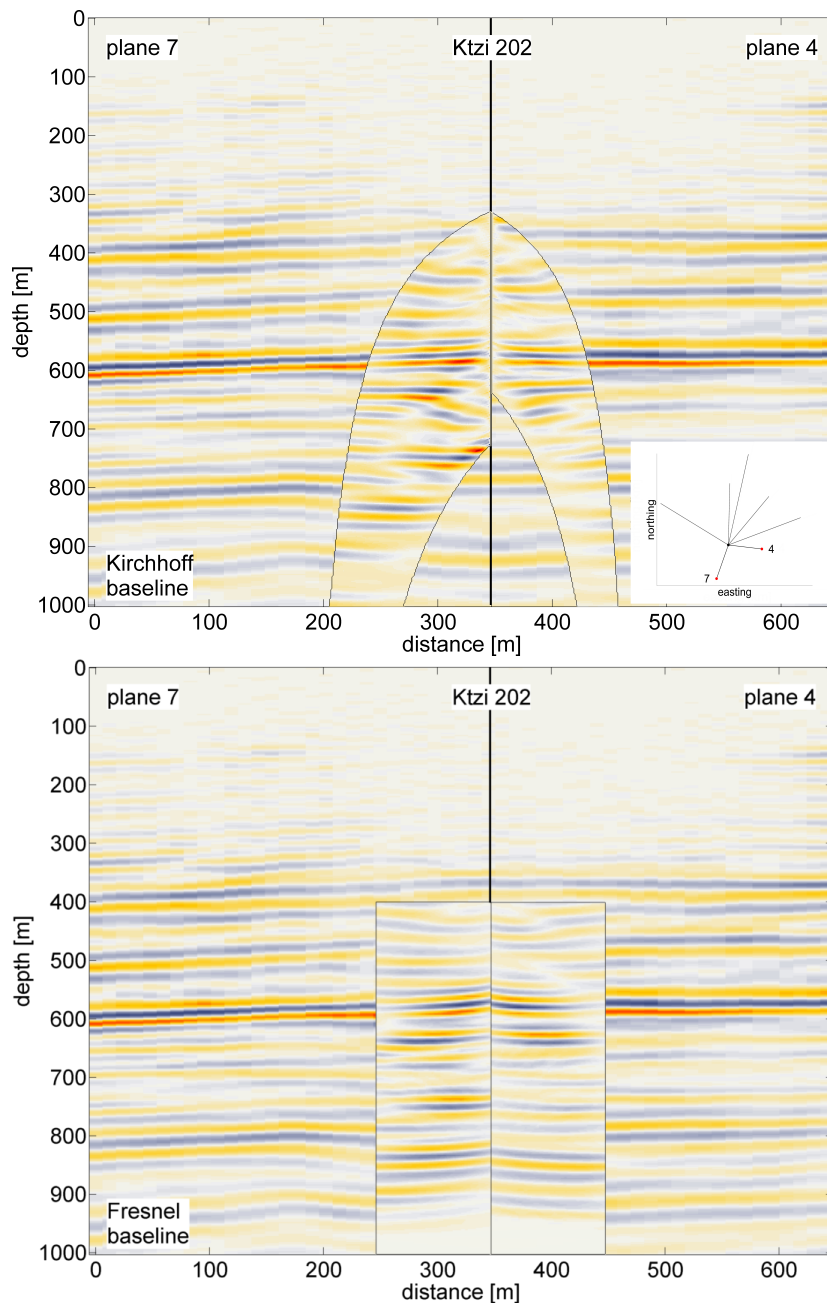


Figure 6.15: Results of Kirchhoff (top) and Fresnel migration (bottom) of source points 7 and 4, baseline measurements. The inset explains the geometry of the images: the imaging planes of source point 7 and 4 are unfold at the Ktzi 202 well and the migration results are presented side by side. For comparison, the 3D surface seismic baseline is inserted in the background. The locations of source points 7 and 4 are at 0 m depth, 0 m and 650 m distance, respectively.

The strong reflection from the 20 m thick anhydrite layer at the top of the Weser Formation can be seen very clearly within both migration methods. Besides the K2, no consistent phases can be found between offset VSP and 3D surface seismic. The offset VSP migration images have higher resolution than corresponding slices from the 3D volume. When comparing different offset VSP source points, which have approximately

the same source - receiver distance (like source point 7 and 4), a good match between the phases is found. Especially for the Fresnel migration (Fig. 6.15, bottom) congruent phases can be traced from one source image, across the Ktzi 202 receiver well into another. Contrary to 3D surface seismic, the top of the reservoir is indicated as a reflection at 630 m depth in the baseline offset VSP data. This can be attributed to the higher vertical resolution of the VSP measurement. A reflection from the reservoir can also be observed in the modelled zero-offset VSP (Chap. 5.7.4) and offset VSP baselines (Chap. 6.7). For the Kirchhoff migration (Fig. 6.15, top), at reservoir depth ( $\sim 630$  m) dipping structures are mapped, which cannot be affirmed by the Fresnel migration (Fig. 6.15, bottom).

Figure 6.16 displays repeat and difference (repeat minus baseline) for offset VSP and 3D surfaces seismic.

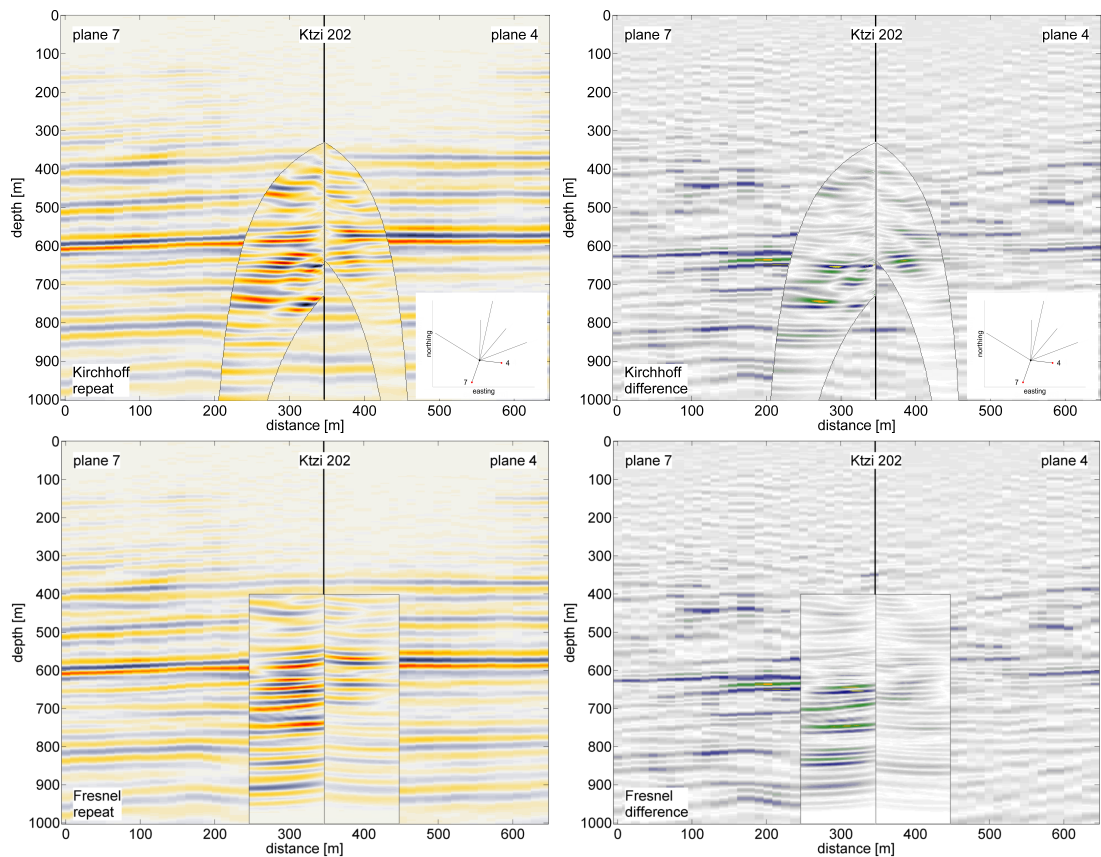


Figure 6.16: Results of Kirchhoff (top) and Fresnel migration (bottom) of source points 7 and 4. The repeat measurements are plotted on the left side, the difference (repeat minus baseline) on the right side. The insets explain the geometry of the images: the imaging planes of source point 7 and 4 are unfold at the Ktzi 202 well and the migration results are presented side by side. For comparison the 3D surface seismic repeat and difference are inserted in the background. The locations of source points 7 and 4 are at 0 m depth, 0 m and 650 m distance, respectively.

As  $\text{CO}_2$  replaces saline water in saturated sandstones, the impedance contrast between the gas filled reservoir and the caprock is increased (Chap. 2.3.3). This effect can be observed in the offset VSP repeat data of source point 7 for both migration algorithms (Fig. 6.16, left column), where increased amplitudes are observed at reservoir depth.

As for the baseline data, the Kirchhoff migration yields a more distorted image of the wavefield than the Fresnel migration. The time-lapse signature is attributed to CO<sub>2</sub> (and not to measurement or other artefacts) because of two reasons: (1) The signature is not recorded above the reservoir level. (2) Since solely the imaging plane of source point number 7 is crossing through the amplitude difference (Fig. 6.1) and no time-lapse signature is found for the other source points (Fig. 6.17, Appendix A), good repeatability can be assumed for areas not influenced by the CO<sub>2</sub>. Within the difference sections (repeat minus baseline, Fig. 6.16, right column) a clear signature caused by the injection of CO<sub>2</sub> can be observed. Above the reservoir (~ 630 m depth) weak amplitude artefacts are still visible. Within the Kirchhoff migration a difference signature is also visible in the imaging plane of source point 4, what cannot be confirmed by the Fresnel migration. Figure 6.17 shows results of Kirchhoff (left column) and Fresnel migration (right column) of source points 6 and 3 (Fig. 6.1). The other source points are presented in Appendix A. The data of baseline, repeat and difference are presented from top to bottom. The insets explain the geometry of the images: the imaging planes of source point 6 and 3 are unfold at the Ktzi 202 well and the migration results are presented side by side. For comparison the 3D surface seismic baseline, repeat and difference is inserted in the background. The locations of source points 6 and 3 are at 0 m depth, 0 m and 1300 m distance, respectively. The data sets are normalised to the centre peak of the K2 reflector.

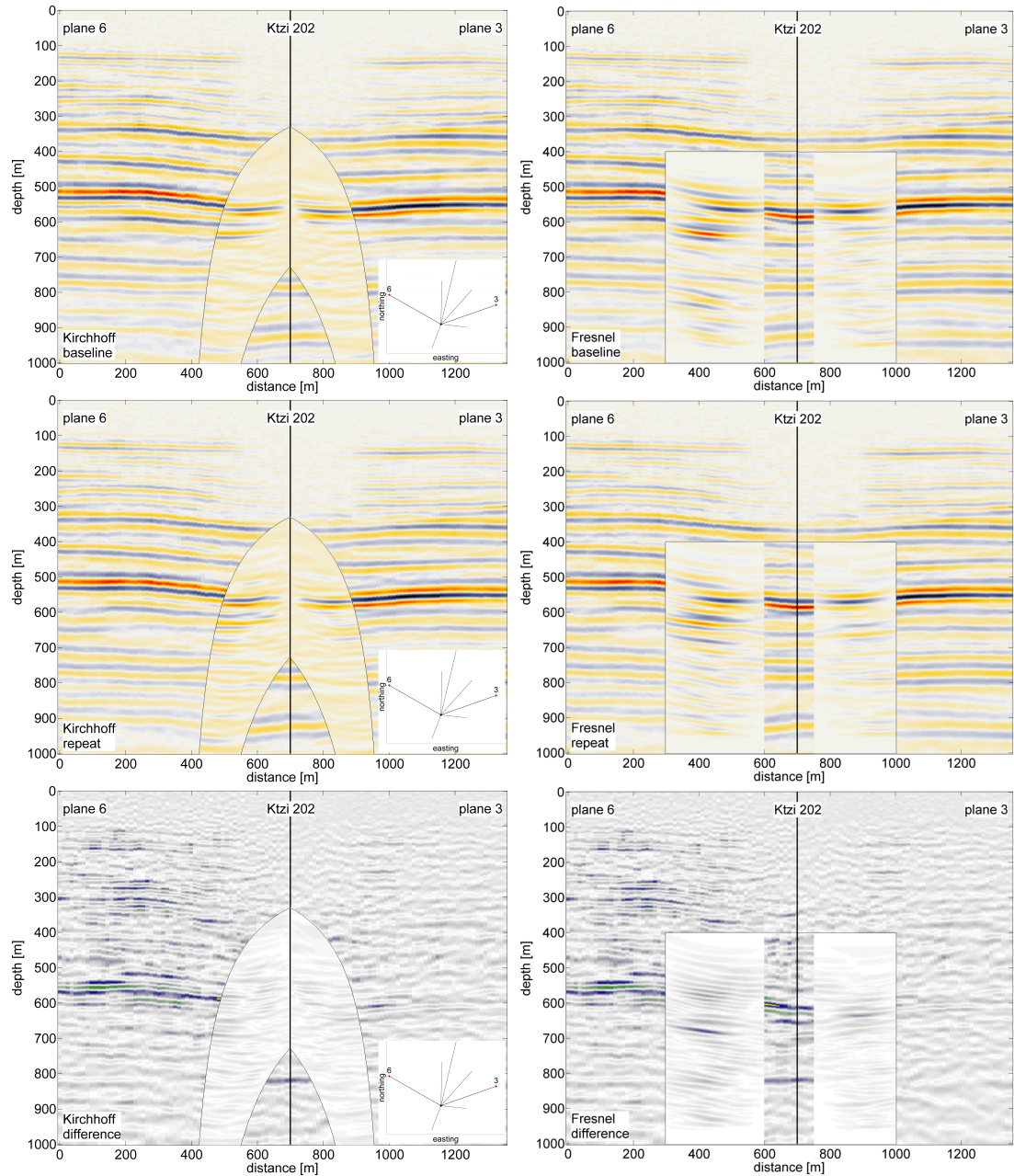


Figure 6.17: Results of Kirchhoff (left column) and Fresnel migration (right column) of source points 6 and 3 (Fig. 6.1). The data of baseline, repeat and difference are presented from top to bottom. The insets explain the geometry of the images: the imaging planes of source point 6 and 3 are unfold at the Ktzi202 well and the migration results are presented side by side. For comparison the 3D surface seismic baseline, repeat and difference is inserted in the background. The locations of source points 6 and 3 are at 0 m depth, 0 m and 1300 m distance, respectively. The data sets are normalised to the centre peak of the K2 reflector.

The dipping anticlinal structure towards source point 6 is better imaged by Fresnel migration than by Kirchhoff migration. Within the 3D surface seismic difference (Fig. 6.17, bottom row), strong amplitude artefacts which are not induced by CO<sub>2</sub> injection are visible. The offset VSP is not affected by the same artefacts, and can serve

as a second proof that no CO<sub>2</sub> has migrated outside the reservoir.

## 6.7 Modelling of offset VSP data

*Modelling of offset VSP data was done to test how a given anomaly will pass the processing and imaging workflow.*

**Petrophysical model parameters and 2D FD modelling:** Modelling of the offset VSP was done for the same seismic elastic model, as the zero-offset VSP (Chap. 5.7.1). The modelling was done again with the Finite Difference (FD) modelling tool of the ReflexW software, which allows the simulation of seismic wave propagation based on the 2D elastic-wave equation (Chap. 5.7.2). Only the dimensions of the model are adapted to the geometry of the offset VSP measurement. Here, the offset of source point 7 to the receiver well is chosen (346 m, Tab. 6.1). The model boundaries (top, sides and bottom) have distances of  $\sim 100$  m to the source and receiver locations to minimize their influence. That leads to model dimensions of 0 - 546 m in horizontal direction and 0 - 1200 m in vertical direction. The whole model was shifted 100 m downward, leading to a thick homogeneous top layer, in which the source is placed at 100 m depth, the receiver depth range is also shifted relative to the source depth to 560 - 800 m (Fig. 5.11). The 2D FD modelling parameters remained unchanged.

**Processing:** The modelled traces are processed in the same way as the measured traces (Chap. 6.4). Figure 6.18 shows the raw data of source point 7 (baseline and repeat, left column) and modelled baseline and repeat (right column). An upgoing reflection from the K2 anhydrite layer (Chap. 2.4.3) can be observed in the measured and modelled data (Fig. 6.18, red lines).

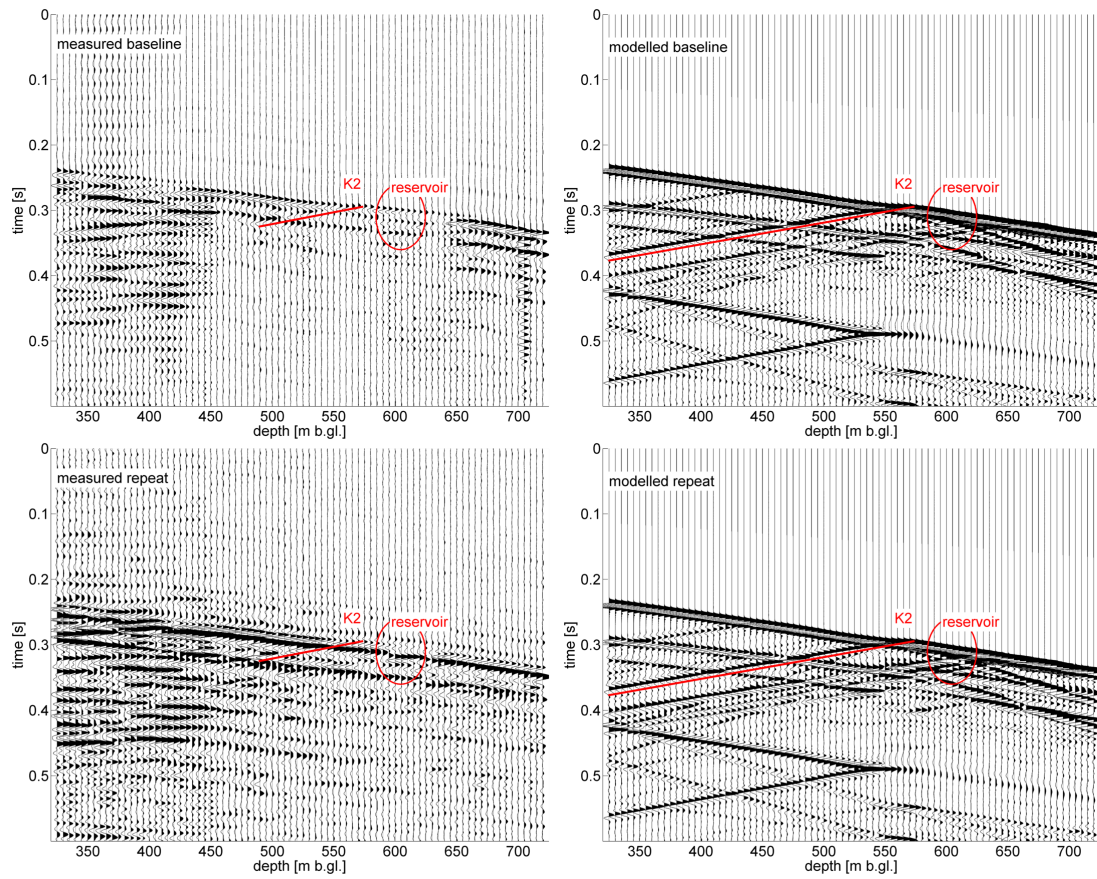


Figure 6.18: Raw data of source point 7 (baseline and repeat, left column) and modelled baseline and repeat (right column). Upgoing reflections from the K2 anhydrite layer (red lines) and the depth of the reservoir (red circle) are indicated. The depth is in meter below ground level [m b.gl.].

The upgoing modelled wavefield used for the Kirchhoff and Fresnel migration is shown in Figure 6.19, after *fk*-filtering and the application of an Ormsby bandpass (Table 6.3). For comparison the upgoing wavefield of source point 7 is shown in the left column for baseline and repeat. The modelled baseline and repeat is shown in the right column. For the modelled repeat, increased amplitudes in the depth range of the reservoir can be clearly observed.

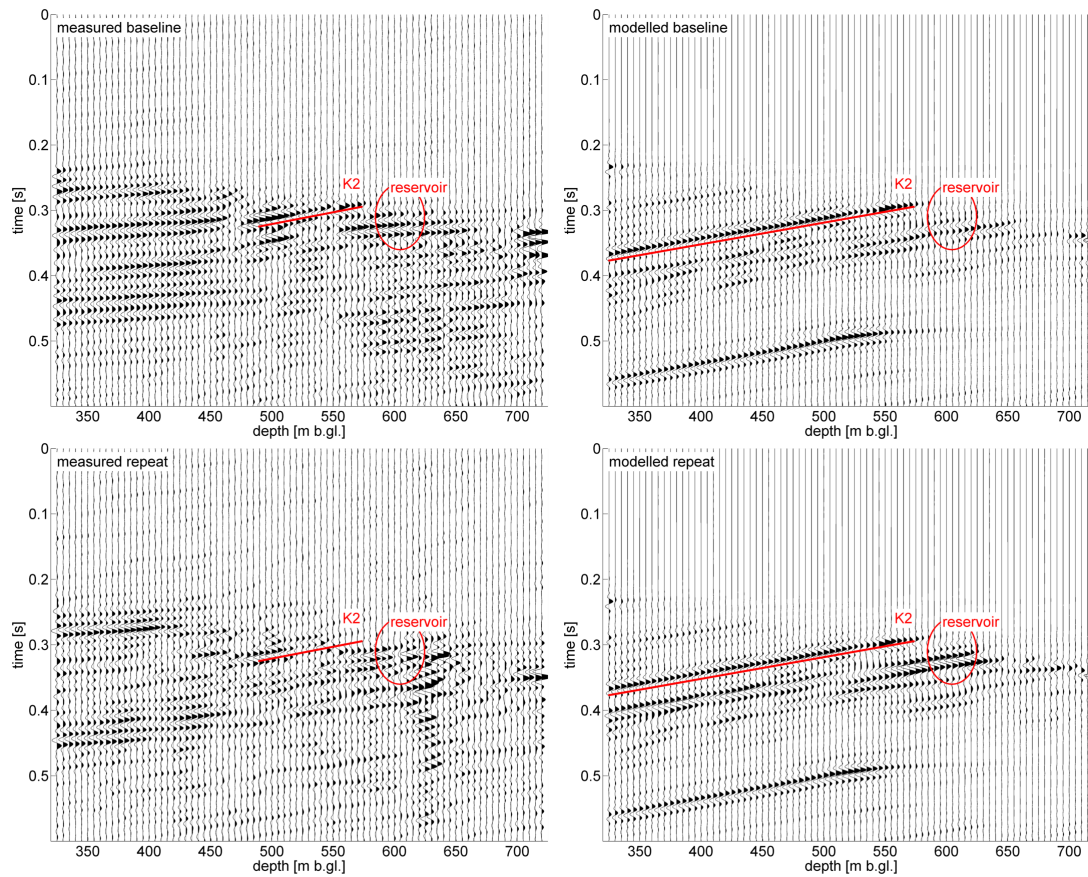


Figure 6.19: Upgoing wavefield of source point 7 (baseline and repeat, left column) and modelled baseline and repeat (right column). Upgoing reflections from the K2 anhydrite layer (red lines) and the depth of the reservoir (red circle) are indicated. The depth is in meter below ground level [m b.gl.].

**Migration:** Kirchhoff and Fresnel migration of modelled data is performed as described in Chapter 6.6. For both algorithms, the migration is done with the input velocities used for modelling (that means with the optimum velocity model, Fig. 6.7). Figure 6.20 shows the Kirchhoff and Fresnel migration results for the modelled baseline, repeat and difference (repeat minus baseline, from top to bottom). The geometry of the images is similar to the comparison between different offset VSP source points (Chap. 6.6.3, Fig. 6.20 inset): the imaging plane of source point 7 (the modelling was based on that offset) is mirrored at the Ktzi 202 well and the Kirchhoff and Fresnel migration results are presented side by side. For comparison, the 3D surface seismic baseline, repeat and difference is inserted in the background. The locations of both source points are at 0 m depth, 0 m and 650 m distance, respectively. The data sets are normalised to the centre peak of the K2 reflector.

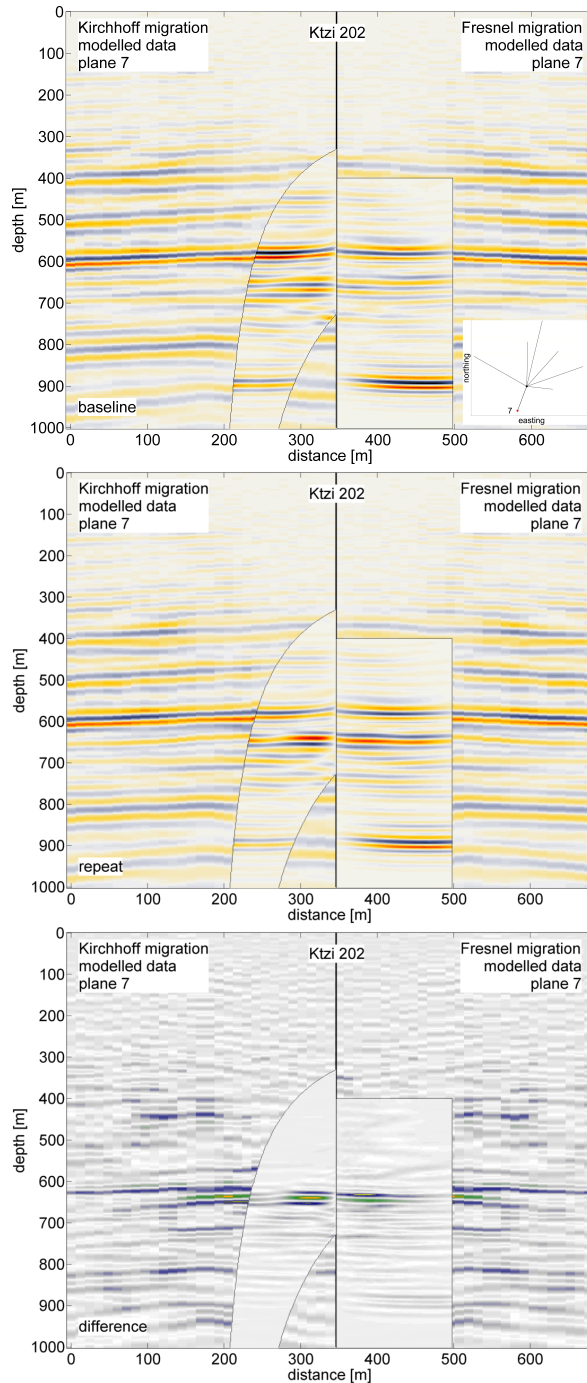


Figure 6.20: Kirchhoff and Fresnel migration results for the modelled baseline, repeat and difference (repeat minus baseline, from top to bottom). The inset explains the geometry of the images: the imaging plane of source point 7 (the modelling was based on that offset) is mirrored at the Ktzi 202 well and the Kirchhoff and Fresnel migration results are presented side by side. For comparison, the 3D surface seismic baseline, repeat and difference is inserted in the background. The locations of both source points are at 0 m depth, 0 m and 650 m distance, respectively. The data sets are normalised to the centre peak of the K2 reflector.

For both imaging methods, the reflection from the K2 is well imaged, the horizontal

layers of the input model are restored and there is a good match between the phases (Fig. 6.20, top). As for the modelled zero-offset VSP (Chap. 5.7.4) and measured offset VSP (Chap. 6.6.3), the top of the reservoir is indicated as a reflection at 630 m depth. The increased amplitudes of the repeat are correctly mapped at reservoir depth (Fig. 6.20, middle). As for the measured data, the Kirchhoff migration yields a slightly more distorted image of the wavefield than the Fresnel migration. After passing through the processing and imaging workflow the amplitude difference is still visible for both imaging methods. Although the velocity of the reservoir layer was reduced over the entire model dimension (0-546 m), the imaging capability is restricted to distances of  $\sim 50$  m (Kirchhoff migration) and  $\sim 100$  m (Fresnel migration) from the well. Outside of this zone, no amplitude changes are mapped. The amplitude difference of the Fresnel migration in depth is confined to the reservoir layer, whereas the signature of the Kirchhoff migration is broader.

## 6.8 Conclusions

It is possible to generate a lateral image of the reservoir at the injection site:

- **Kirchhoff and Fresnel migration of source point 7, 4, 5 and 3 (Figs. 6.15, 6.16 and 6.17):** The strong reflection from the 20 m thick anhydrite layer at the top of the Weser Formation is imaged. Besides the K2, no consistent phases can be found between offset VSP and 3D surface seismic. The offset VSP migration images have higher resolution than corresponding slices from the 3D volume. Comparing different offset VSP source points, which have approximately the same source-receiver distance, there is a good match between the phases. Contrary to 3D surface seismic, the top of the reservoir is indicated as a reflection at 630 m depth in the baseline offset VSP data. This can be attributed to the higher vertical resolution of the VSP measurement. CO<sub>2</sub> induced changes in reflectivity can be observed in the offset VSP repeat data of source point 7 for both migration algorithms. The time-lapse signature is attributed to CO<sub>2</sub> (and not to measurement or other artefacts) because of two reasons: (1) The signature is not recorded above the reservoir level. (2) Since, solely the imaging plane of source point number 7 is crossing through the amplitude difference and no time-lapse signature is found for the other source points, good repeatability can be assumed for areas not influenced by the CO<sub>2</sub>. Within the difference sections a clear signature caused by the injection of CO<sub>2</sub> can be observed. Above the reservoir ( $\sim 630$  m depth) weak amplitude artefacts are still visible. Within the imaging plane of source point 6 strong amplitude artefacts which are not induced by CO<sub>2</sub> injection are visible in the 3D surface seismic difference. The offset VSP is not affected by the same artefacts, and can serve as a second proof that no CO<sub>2</sub> has migrated outside the reservoir.
- **Kirchhoff and Fresnel migration of modelled source point 7 (Fig. 6.20):** For both imaging methods, the reflection from the K2 is well imaged, the horizontal layers of the input model are restored and there is a good match between the phases. As for the modelled zero-offset VSP and measured offset VSP, the top of the reservoir is indicated as a reflection at 630 m depth. The increased amplitudes of the repeat are correctly mapped at reservoir depth. After passing through the processing and imaging workflow the amplitude difference is still visible for both imaging methods.

The application of two migration algorithms can help to differentiate between method-related and true time-lapse effects when interpreting the seismic images. The comparison of Kirchhoff and Fresnel migration reveals some differences when imaging offset VSP data:

- **Differences between migration algorithms for source point 7, 4, 5 and 3 (Figs. 6.15, 6.16 and 6.17):** Especially for the Fresnel migration congruent phases can be traced from one source image into another. For the Kirchhoff migration, at reservoir depth dipping structures are mapped and it yields a more distorted image of the wavefield than the Fresnel migration. A difference signature is also visible in the Kirchhoff migration of source point 4, what cannot be confirmed by the Fresnel migration. The dipping anticlinal structure towards source point 6 is better imaged by Fresnel migration than by Kirchhoff migration.
- **Differences between migration algorithms for modelled source point 7 (Fig. 6.20):** As for the measured data, the Kirchhoff migration yields a slightly more distorted image of the wavefield than the Fresnel migration. Although the velocity of the reservoir layer was reduced over the entire model dimension (0-546 m), the imaging capability is restricted to distances of  $\sim 50$  m (Kirchhoff migration) and  $\sim 100$  m (Fresnel migration) from the well. Outside of this zone, no amplitude changes are mapped. The amplitude difference of the Fresnel migration in depth is confined to the reservoir layer, whereas the signature of the Kirchhoff migration is broader.



# 7 Chapter 7

---

## Summary

Based on geological information and well cores, the reservoir is described as thin and heterogeneous at the research site. "The thickness of the reservoir is generally less than 20 m, and is below the resolution of conventional surface seismic data" (Yang (2012)). Borehole seismic methods are expected to have a higher resolution than surface seismic, therefore three different borehole seismic methods are tested: (1) crosshole seismic, (2) zero-offset VSP and (3) offset VSP.

The crosshole seismic measurement was designed to follow the migration of CO<sub>2</sub> at small scale during the injection. "As CO<sub>2</sub> replaces saline water in saturated reservoir sandstones a P-wave velocity reduction may occur. This velocity change can potentially be used to monitor CO<sub>2</sub> in sandstone aquifers using seismic tomography" (Zhang et al. (2012)).

The main objective of the zero-offset and offset VSP surveys was to generate high-resolution seismic images in the vicinity of the borehole. As CO<sub>2</sub> replaces saline water in saturated sandstones, the impedance contrast between the gas filled sandstones and the caprock is increased, what leads to stronger reflections from top of the reservoir. This increased reflectivity can be used to image the spreading of CO<sub>2</sub> in the reservoir. While the zero-offset VSP focuses on normal incidence reflectivity near the observation well, offset VSP has the potential to generate a lateral image of the reservoir at the injection site.

Two questions should be answered: With these methods, is it possible (1) to map the CO<sub>2</sub> in the reservoir layer, (2) to derive geometrical and petrophysical parameters describing the migration of CO<sub>2</sub> in a water saturated sandstone reservoir?

**Question (1): The CO<sub>2</sub> can be mapped by all methods applied.**

**Crosshole seismic:** Even though, no significant time-lapse effects were observed on the measured crosshole seismic data, travel time tomography is tested on synthetic data having the same geometry as the real data. The modelling study is based on the average velocity model derived from the measured data. The results of the modelling study can be generalised for the interpretation of time-lapse crosshole experiments investigating the migration of CO<sub>2</sub> in a water saturated sandstone. Figure 7.1 shows the key results of this study. The velocity change follows the input anomaly as a rough estimate of the location of the changes in the reservoir caused by the injection of CO<sub>2</sub>. Inherent layering or thinning of the input anomaly is not resolved. The CO<sub>2</sub> anomaly is smeared out beyond the range of the input model.

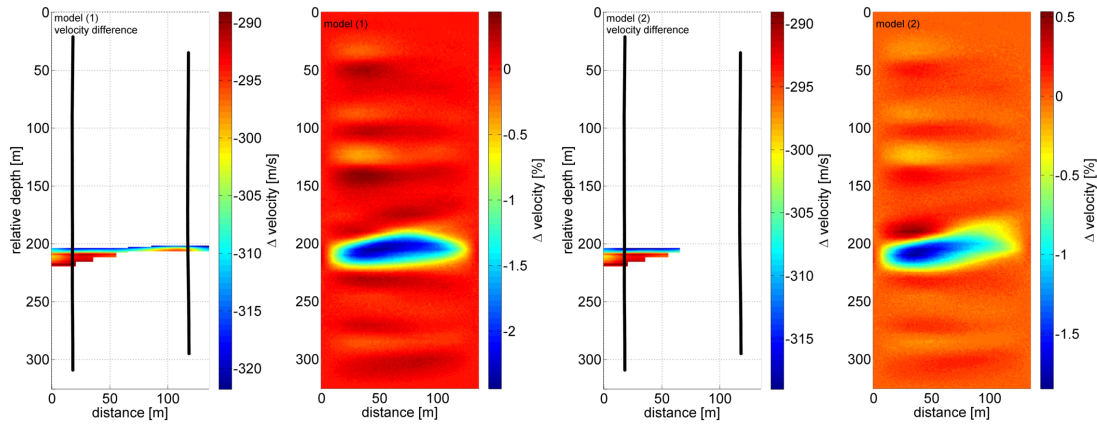


Figure 7.1: Results of the travel time tomography of synthetic data for two different scenarios of CO<sub>2</sub> induced velocity differences.

**Zero-offset VSP:** Figure 7.2 shows the zero-offset VSP time-lapse amplitude difference of measured and modelled data. It is possible to identify consistent phases within 3D surface seismic data and zero-offset VSP data. The dynamic range of the amplitudes is comparable for both methods. More details of the structure below the top of the reservoir are resolved in the zero-offset VSP data than in the 3D surface seismic data.

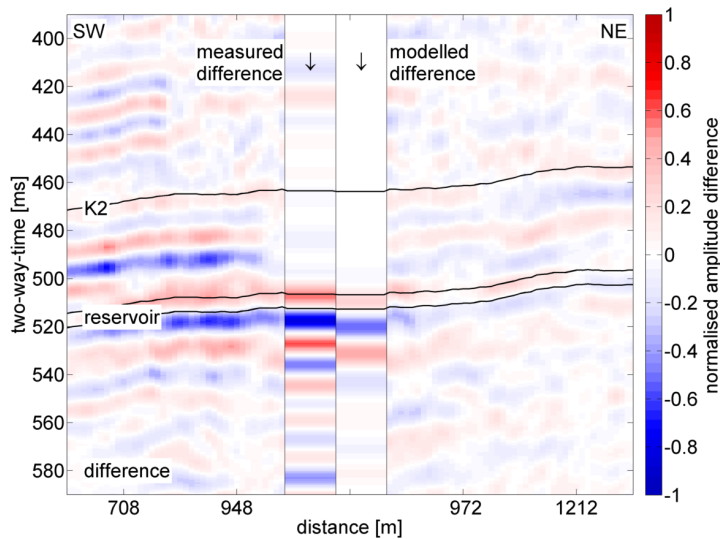


Figure 7.2: Time-lapse amplitude difference of the 3D surface seismic, measured and modelled zero-offset VSP.

**Offset VSP:** Figure 7.3 shows the offset VSP time-lapse amplitude difference of measured and modelled data for Kirchhoff and Fresnel migration. The other offset VSP imaging planes show no CO<sub>2</sub> induced time-lapse differences and can serve as a second proof (besides surface seismic methods) that no CO<sub>2</sub> has migrated outside the reservoir. The application of two migration algorithms can help to differentiate between method-related and true time-lapse effects when interpreting the seismic images. Due to limitations of the imaging methods, the time-lapse effect can be imaged to distances of  $\sim 50$  m (Kirchhoff migration) and  $\sim 100$  m (Fresnel migration) from the well.

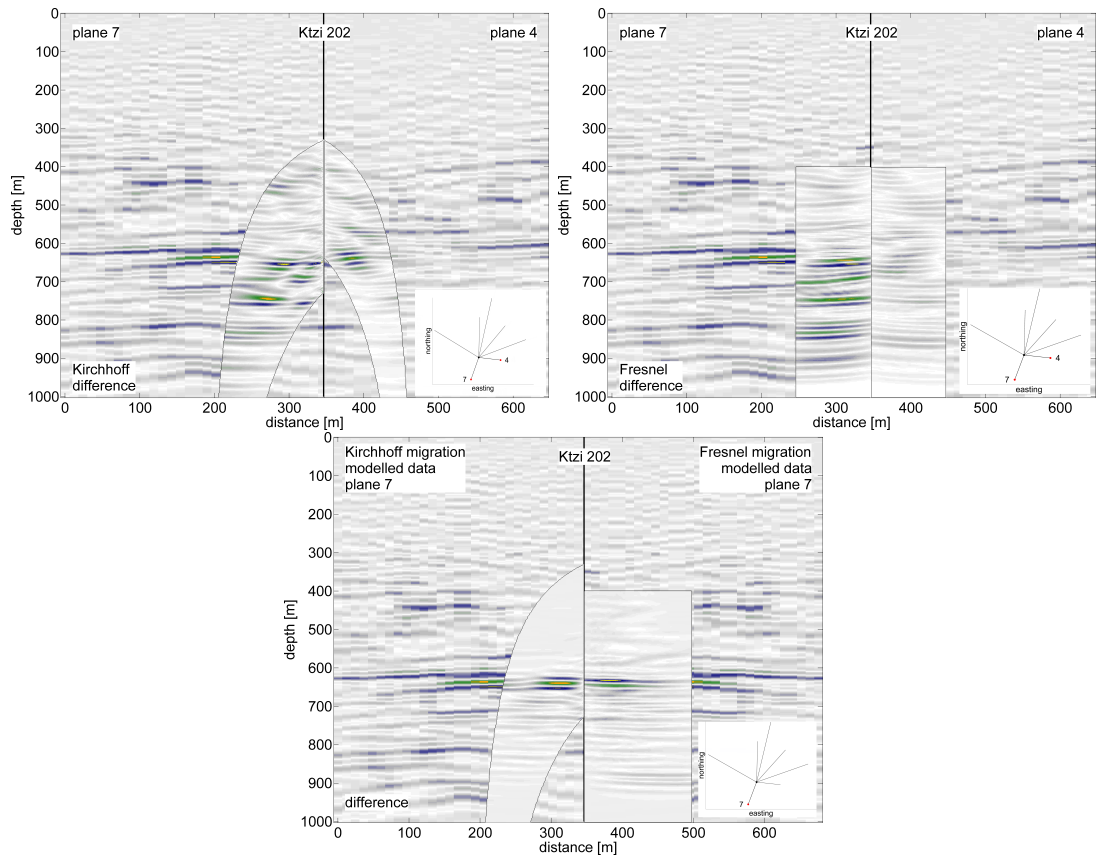


Figure 7.3: Time-lapse amplitude difference of the 3D surface seismic, measured and modelled offset VSP. Top: Kirchhoff migration and Fresnel migration of measured data (left and right). Bottom: Kirchhoff and Fresnel migration of measured and modelled data.

**Question (2): Geometrical and petrophysical parameters describing the migration of CO<sub>2</sub> in a water saturated sandstone reservoir are derived by crosshole seismic and zero-offset VSP.**

**Crosshole seismic:** For the modelling study, the amplitude of the input velocity was reduced by 10% within the reservoir (Fig. 7.1), after forward calculation and inversion the final maximum velocity reduction in the reservoir was about ~ 2%. The underestimation of the anomaly is linked to an overestimation of the observed travel time, since the fastest rays are those that circumvent the low velocity zone. This leads to an overestimation of the velocity and therefore to an underestimation of the amplitude of velocity anomalies in an inversion problem. For media with structures a size smaller than the Fresnel volume, this effect is intensified by the forward calculation of travel times based on the standard ray theory, which is derived using a high-frequency approximation (Musil et al. (2003), Spetzler et al. (2008)).

**Zero-offset VSP:** Based on the CO<sub>2</sub> induced amplitude changes, the thickness of the CO<sub>2</sub> plume and the reduction of P-wave velocity are calculated. Figure 7.4 shows the result of a wedge modelling study. When comparing both, the shape and the amplitude of the measured and modelled zero-offset VSP, the CO<sub>2</sub> layer thickness is estimated with 6 m. It is possible, that at the time of the zero-offset VSP repeat, the reservoir layer was not totally influenced by the CO<sub>2</sub> plume, but only the uppermost 6 m.

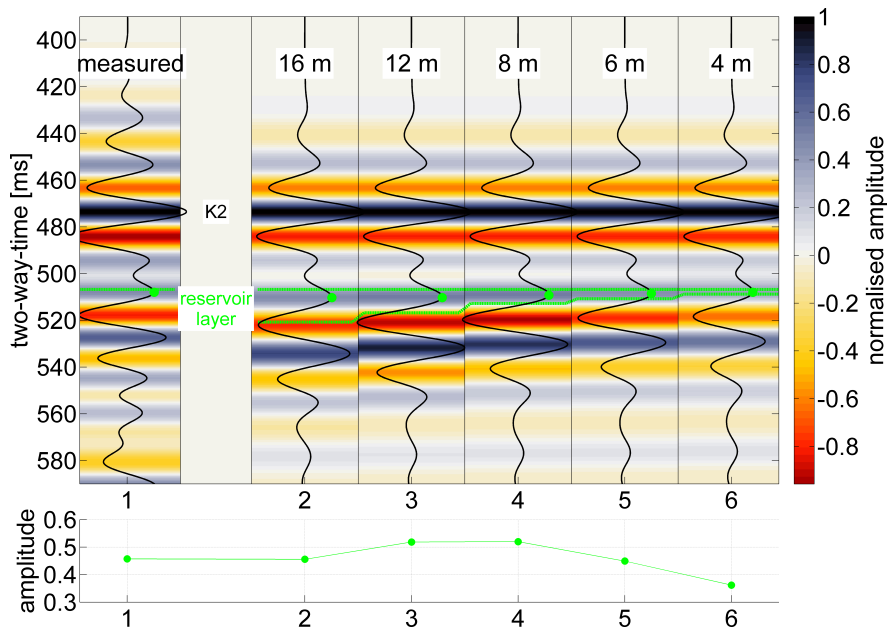


Figure 7.4: Result of a wedge modelling study based on zero-offset VSP data.

By performing a band limited impedance inversion it was possible to gain an estimate of the velocity change within the reservoir (Fig. 7.5). The modelled data are based on a velocity reduction of 30 %, after processing and inversion a velocity reduction of 26 % and 21 % was found for the high and low frequency data, respectively. The velocity reduction at the top of the reservoir is 32 % for the measured data (for both bandpass ranges).

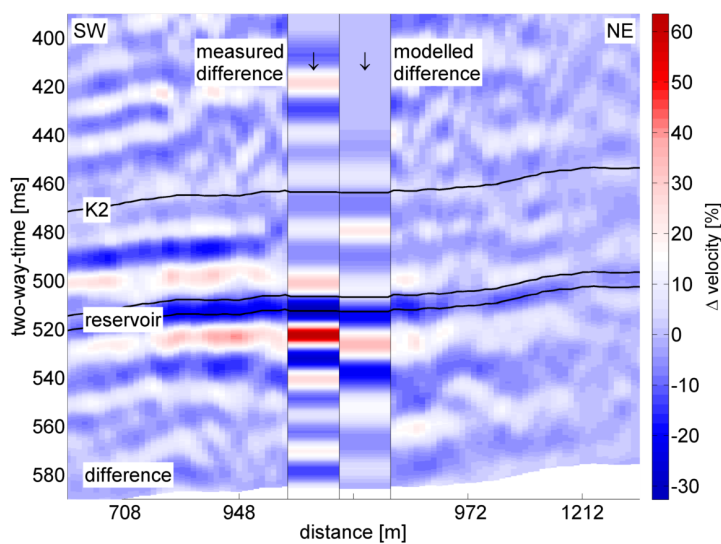


Figure 7.5: Result of the band limited impedance inversion of zero-offset VSP data.

---

## Time-lapse analysis

When monitoring CO<sub>2</sub> injection, special attention should be paid to the repeatability of the time-lapse data and artefacts introduced by processing or imaging.

The synthetic crosshole seismic data showed mean observed travel time changes of 0.263 ms for model (2) (Fig. 7.1), one period of the highest expected frequency (4000 Hz) would be 0.25 ms. A careful distinction between inherent travel time changes and CO<sub>2</sub> induced time-lapse effects must be made. Travel time changes can be attributed to picking errors within zones of high noise level, or may occur if the sources/hydrophones are not located at identical depths during the different surveys (Zhang et al. (2012)). High noise levels can be caused by bad or different hydrophone coupling conditions between surveys or by a lower ray coverage within low velocity zones. In addition, inversion artefacts can be introduced by varying source-receiver pairs used for the inversion. The crosshole seismic in Ketzin was acquired with hydrophones, which are used in fluid filled boreholes only. After the breakthrough of CO<sub>2</sub> in the receiver well, clamped geophones would be necessary for the recording. To minimise time-lapse acquisition artefacts, if recording in perforated wells, the employment of geophones instead of hydrophones for all measurements is recommended.

There are many factors influencing the time-lapse effects in the zero-offset and offset VSP data in Ketzin. Differences between baseline and repeat data can be source related, since for baseline and repeat measurements the VIBSIST-1000 and VIBSIST-3000, with a different impact energy, were used. The age of the receiver well can have an effect on the repeatability: better seismic bonding to the formation has been observed as a well ages, since drilling mud, rock cuttings, and sloughing that fill the annulus between the casing and the formation tend to solidify (Hardage (2000)). Other parameters to keep in mind are source and receiver positions, near surface effects (e.g. different weather conditions) and different noise levels. By time-lapse processing, differences in the data sets are minimised, while the actual time-lapse anomaly should be preserved. In case of the zero-offset and offset VSP, the repeat traces are matched to the baseline traces by application of a cross-correlation time-shift (Bergmann et al. (2011)). The source of the zero-offset VSP was placed on asphalt close to the well for the baseline measurement, whereas for the repeat it was moved a few meters away and activated on gravel, what can lead to a stronger attenuation of the signal at higher frequencies. Therefore, a bandpass filter is applied before the time-lapse imaging. The offset VSP is imaged by two migration algorithms, these can help to differentiate between method-related and true time-lapse effects when interpreting the seismic images.

## Recommendations and outlook

With crosshole seismic travel time tomography, it is possible to map the CO<sub>2</sub> plume and to derive an estimate of the velocity reduction in the reservoir. To observe the migration of CO<sub>2</sub> during the injection, a dense sequence of repeat measurements is necessary. In Ketzin, lubricators are needed to access the pressurised wells after the breakthrough of CO<sub>2</sub>, what makes repeat measurements time-consuming and expensive. This could be avoided by measuring in unperforated wells or by the utilisation of permanently installed downhole sensors. The velocity anomaly is underestimated by travel time tomography, therefore wavefield based tomography methods should be employed, if the exact velocity reduction sought (Spetzler et al. (2008)).

Zero-offset VSP measurements provided near-well corridor stacks and information about normal incidence reflectivity. It was possible to map the CO<sub>2</sub> plume and to derive

its thickness and the reduction of P-wave velocity. The analysis of the upper part of the zero-offset VSP in Ketzin was not possible, since the receivers were placed in uncemented multiple casing. This could be avoided by measuring in properly cemented wells, or by the utilisation of sensors installed behind the casing. Further analysis could include the construction of an interval velocity model and the estimation of attenuation. It was possible to generate a lateral image of the reservoir at the injection site using the vertical component of offset VSP data. The maximum exploitable offset is determined by the source strength and the geological structure of the underground. Seismically fast layers above the reservoir (as the K2 reflector in Ketzin) lead to refracted waves at a certain distance. Further processing steps could incorporate the horizontal components and examine the imaging capabilities of converted waves. Another approach to benefit from the 3-component offset VSP data could be the application of a Fresnel volume migration (Lüth et al. (2005)).

In the framework of monitoring CO<sub>2</sub> injection, borehole seismic methods should be used as an add-on to surface seismic, in case more detailed information is needed about the structure in the vicinity of boreholes. In Ketzin, recording the seismic signal with permanently installed fibre-optical cables (distributed acoustic sensing, iDAS) is tested. This method overcomes the need of a lubricator to enter the well and profits from the installation of cables behind the casing. A dense sequence zero-offset and offset VSP measurements can be acquired and makes it possible, to observe layers above the reservoir, detect leakage paths or inspect the well integrity.

## Acknowledgements

I would like to express my gratitude to the Centre for CO<sub>2</sub>-Storage of the German Research Centre (GFZ): Here I got the possibility to write this thesis in a wonderful research environment with many colleagues whose suggestions and encouragement helped me in all the time. I want to thank them for all their help, support, interest and valuable hints. In particular, I am grateful to:

Dr. Stefan Lüth and Dr. Rüdiger Giese (both GFZ), for giving me the opportunity to join the geophysical CO<sub>2</sub> storage monitoring group. Especially I am grateful to Dr. Stefan Lüth, my supervisor. I deeply appreciate his support, intensive discussions and encouragement throughout my study.

Prof. Dr. C. M. Krawczyk (TU Berlin and LIAG) for accepting to be evaluator. Especially I want to thank her, for the support and help on improving the thesis through discussions and useful comments.

Prof. Dr. Ir. R. J. Arts (TU Delft) for accepting to be evaluator. I thank him for the inspiration and the enthusiasm he expressed at several workshops and meetings.

My understanding of seismic was enhanced through valuable discussions with the Ketzin seismic monitoring group: Dr. Monika Ivandic, Prof. Dr. Christopher Juhlin, Dr. Artem Kashubin and Dr. Fengjiao Zhang from the Uppsala Universitet. Dr. Peter Bergmann, Dr. Alexandra Ivanova and Magdalena Gil from the GFZ, they always supported me in manifold problems concerning programming, particularities of processing or writing this thesis. Magda, I wish you all the best for your PhD thesis.

I would like to especially thank Dr. Can Yang (Uppsala Universitet) for his mentor work on helping me to get started with VSP processing and Marco Groh who helped getting the server running smoothly whenever problems encountered.

Dr. Cornelia Schmidt-Hattenberger (GFZ), for the possibility to work in the CO<sub>2</sub>ReMoVe project. It was enjoyable to experience the friendly atmosphere and get in contact with researchers from all over Europe.

I was lucky to take part in the fieldwork in Ketzin where I was exposed to the real seismic surveying. I thank the many people being engaged in the surveys, please know that I enjoyed to be in the field with you: Dr. Calin Cosma (Vibrometric), Dr. Sverker Olson and Hans (Hasse) Palm (both Uppsala Universitet).

I am thankful for the great company of Gunther Baumann, Tanja Kollersberger, Tim Labitzke, Dr. Marcus Möller, Stefan Schröder, and Florian Wagner (all GFZ).

For granting financial support of this PhD, I thank the CO<sub>2</sub>ReMoVe project (Project Reference: 518350), funded by the European Commission under the 6th Framework Programme and by the industry partners. Further financial support was granted by the CO<sub>2</sub>Man project (grant 03G0760A), a national scientific initiative funded by the Federal Ministry of Education and Research within the GEOTECHNOLOGIEN Program and from industry partners.

Finally, I express my gratitude to members of my family for the greatest source of kindness and patience.

Last, and most importantly, I'm deeply thankful to my beloved Michael for his support and encouragement.



# Bibliography

- Arts, R., Meekes, J., Brouwer, J., van der Werf, M., Noorlandt, R., Paap, B., Visser, W., Vandeweyer, V., Lüth, S., Giese, R., Maas, J., 2011. Results of a monitoring pilot with a permanent buried multicomponent seismic array at Ketzin. *Energy Procedia* 4, 3588–3595.
- Bancroft, J. C., 2008. Differential operators 3: The square-root derivative. CREWES Research Report 20.
- Becquey, M., Lavergne, M., Willm, C., 1979. Acoustic impedance logs computed from seismic traces. *Geophysics* 44 (9), 1485–1501.
- Bergmann, P., Lengler, U., Schmidt-Hattenberger, C., Giese, R., Norden, B., 2010. Modelling the geoelectric and seismic reservoir response caused by carbon dioxide injection based on multiphase flow simulation: Results from the CO<sub>2</sub>SINK project. *Chemie der Erde* 70, S3, 173–183.
- Bergmann, P., Schmidt-Hattenberger, C., Kiessling, D., Rücker, C., Labitzke, T., Henniges, J., Baumann, G., Schütt, H., 2012. Surface-downhole electrical resistivity tomography applied to monitoring of CO<sub>2</sub> storage at Ketzin, Germany. *Geophysics* 77, B253–B267.
- Bergmann, P., Yang, C., Lüth, S., Juhlin, C., Cosma, C., 2011. Time-lapse processing of 2D seismic profiles with testing of static correction methods at the CO<sub>2</sub> injection site Ketzin (Germany). *Journal of Applied Geophysics* 75 (1), 124–139.
- Berteussen, K., Ursin, B., 1983. Approximate computation of the acoustic impedance from seismic data. *Geophysics* 48 (10), 1351–1358.
- Borm, G., Förster, A., 2005. Tiefe salzwasserführende Aquifere - eine Möglichkeit zur geologischen Speicherung von CO<sub>2</sub>. *Energiewirtschaftliche Tagesfragen - Zeitschrift für Energiewirtschaft, Recht, Technik und Umwelt* 8, 15–20.
- Bubshait, S., Lawton, D., 2008. Zero offset VSP processing for coal reflections. CREWES Research Report 20, 1–25.
- Cosma, C., Enescu, N., 2001. Characterization of fractured rock in the vicinity of tunnels by the swept impact seismic technique. *International Journal of Rock Mechanics & Mining Sciences* 38, 815–821.
- CREWES, 2012. Free Seismology Textbook and Software. Accessed 2012. [www.crewes.org/ResearchLinks/FreeSoftware/](http://www.crewes.org/ResearchLinks/FreeSoftware/).
- DECO Geophysical Software Company, 2013. RadExPro Plus - User Manual.
- Dillon, P., 1990. A comparison between Kirchhoff and GRT migration on VSP data. *Geophysical Prospecting* 38, 151–111.
- Ferguson, R., Margrave, G., 1996. A simple algorithm for band-limited impedance inversion. CREWES Research Report 8, 21–1–21–10.
- Fischer, S., Liebscher, A., Wandrey, M., the CO<sub>2</sub>SINK Group, 2010. CO<sub>2</sub>-brine-rock interaction - First results of long-term exposure experiments at in situ P-T conditions of the Ketzin CO<sub>2</sub> reservoir. *Chemie der Erde* 70(S3), 155–164.

- Fischer, S., Zemke, K., Liebscher, A., Wandrey, M., 2011. Petrophysical and petrochemical effects of long-term CO<sub>2</sub>-exposure experiments on brine-saturated reservoir sandstone. *Energy Procedia* 4, 4487–4494.
- Förster, A., Giese, R., Juhlin, C., Norden, B., Springer, N., CO<sub>2</sub>SINK-Group, 2009. The Geology of the CO<sub>2</sub>SINK Site: From Regional Scale to Laboratory Scale. *Energy Procedia* 1, 2911–2918.
- Förster, A., Norden, B., Zinck-Jørgensen, K., Frykman, P., Kulenkampff, J., Spangenberg, E., Erzinger, J., Zimmer, M., Kopp, J., Borm, G., Juhlin, C., Cosma, C., Hurter, S., 2006. Baseline characterization of the CO<sub>2</sub>SINK geological storage site at Ketzin, Germany. *Environmental Geosciences* 13 (3), 145–161.
- Förster, A., Schöner, R., Förster, H.-J., Norden, B., Blaschke, A.-W., Luckert, J., Beutler, G., Gaupp, R., Rhede, D., 2010. Reservoir characterization of a CO<sub>2</sub> storage aquifer: The Upper Triassic Stuttgart Formation in the Northeast German Basin. *Marine and Petroleum Geology* 27, 2156–2172.
- Freifeld, B., Daley, T., Hovorka, S., Henninges, J., Underschultz, J., Sharma, S., 2009. Recent advances in well-based monitoring of CO<sub>2</sub> sequestration. *Energy Procedia* 1, 2277–2284.
- Frykman, P., Nielsen, C., Norden, B., Förster, A., 2009. Modelling and predictions in the Ketzin CO<sub>2</sub> storage experimental site. 13th Annual Conference of the International Association of Mathematical Geosciences (Stanford, CA, USA) IAMG09, CD-ROM.
- Gardner, G., Gardner, L., Gregor, A., 1974. Formation velocity and density - The diagnostic basics for stratigraphic traps. *Geophysics* 39 (6), 770–780.
- Geo Sys - Umwelttechnik und Geogeräte GmbH Leipzig, 2012. Lubrikator. Accessed 2012. <http://www.geosys-germany.com/geophysik/lubrikator/>.
- Giese, R., Henninges, J., Lüth, S., Morozova, D., Schmidt-Hattenberger, C., Würdemann, H., Zimmer, M., Cosma, C., Juhlin, C., CO<sub>2</sub>SINK-Group, 2009. Monitoring at the CO<sub>2</sub>SINK site: A concept integrating geophysics, geochemistry and microbiology. *Energy Procedia* 1, 2251–2259.
- Girard, J.-F., Coppo, N., Rohmer, J., Bourgeois, B., Naudet, V., Schmidt-Hattenberger, C., 2011. Time-lapse CSEM monitoring of the Ketzin (Germany) CO<sub>2</sub> injection using 2xMAM configuration. *Energy Procedia* 4, 3322–3329.
- Götz, J., Giese, R., Lüth, S., Schmidt-Hattenberger, C., Juhlin, C., Cosma, C., 2011. Borehole seismic monitoring of CO<sub>2</sub> storage within a saline aquifer at Ketzin, Germany. EAGE Borehole Geophysics Workshop - Emphasis on 3D VSP, 16-19 January 2011, Istanbul, Turkey, EarthDoc-47183.
- Hampson, D., Mewhort, L., 1983. Using a vertical seismic profile to investigate a multiple problem in western Canada. *Journal of the Canadian Society of Exploration Geophysicists* 19 (1), 16–33.
- Hansen, T. M., 2011. mgstat: A Geostatistical Matlab toolbox. Accessed 2012. <http://mgstat.sourceforge.net>.
- Hardage, B. A., 2000. Vertical Seismic Profiling: Principles. Pergamon. Elsevier Science Ltd.
- Henninges, J., Liebscher, A., Bannach, A., Brandt, W., Hurter, S., Köhler, S., Möller, F., CO<sub>2</sub>SINK-Group, 2011. P-T- $\rho$  and two-phase fluid conditions with inverted density profile in observation wells at the CO<sub>2</sub> storage site at Ketzin (Germany). *Energy Procedia* 4, 6085–6090.
- Hole, J., Zelt, B., 1995. 3-D finite-difference reflection traveltimes. *Geophys. J. Int.* 121, 427–434.

- IPCC, 2005. Special report on carbon dioxide capture and storage: prepared by working group III of the Intergovernmental Panel on Climate Change. Cambridge University Press, Cambridge and New York.
- Ivandic, M., Yang, C., Lüth, S., Cosma, C., Juhlin, C., 2012. Time-lapse analysis of sparse 3D seismic data from the CO<sub>2</sub> storage pilot site at Ketzin, Germany. *Journal of Applied Geophysics* 84, 14–28.
- Ivanova, A., Kashubin, A., Juhojuntti, N., Kummerow, J., Henniges, J., C. Juhlin, C., Lüth, S., Ivandic, M., 2012. Monitoring and volumetric estimation of injected CO<sub>2</sub> using 4D seismic, petrophysical data, core measurements and well logging: a case study at Ketzin, Germany. *Geophysical Prospecting* 2012, online first.
- Jensen, J., Jacobsen, B., Christensen-Dalsgaard, J., 2000. Sensitivity kernels for time-distance inversion. *Solar Physics* 192, 231–239.
- Juhlin, C., Giese, R., Zinck-Jørgensen, K., Cosma, C., Kazemeini, H., Juhojuntti, N., Lüth, S., Norden, B., Förster, A., 2007. Case History: 3D baseline seismics at Ketzin, Germany: The CO<sub>2</sub>SINK project. *Geophysics* 72 (5), B121–B132.
- Kazemeini, S., Juhlin, C., Fomel, S., 2010a. Monitoring CO<sub>2</sub> response on surface seismic data; a rock physics and seismic modeling feasibility study at the CO<sub>2</sub> sequestration site, Ketzin, Germany. *Journal of Applied Geophysics* 71 (4), 109–124.
- Kazemeini, S., Juhlin, C., Zinck-Jørgensen, K., Norden, B., 2009. Application of the continuous wavelet transform on seismic data for mapping of channel deposits and gas detection at the CO<sub>2</sub>SINK site, Ketzin, Germany. *Geophysical Prospecting* 57, 111–123.
- Kazemeini, S., Yang, C., Juhlin, C., Fomel, S., Cosma, C., 2010b. Enhancing seismic data resolution using the prestack blueing technique: An example from the Ketzin CO<sub>2</sub> injection site, Germany. *Geophysics* 75 (6), V101–V110.
- Keary, P., Brooks, M., Hill, I., 2002. *An introduction to Geophysical Exploration*. Blackwell Science Ltd.
- Kempka, T., Kühn, M., Class, H., Frykman, P., Kopp, A., Nielsen, C., Probst, P., 2010. Modelling of CO<sub>2</sub> arrival time at Ketzin - Part I. *International Journal of Greenhouse Gas Control* 4, 1007–1015.
- Kießling, D., Schmidt-Hattenberger, C., Schütt, H., Schilling, F., Krüger, K., Schöbel, B., Danckwardt, E., Kummerow, J., CO<sub>2</sub>SINK-Group, 2010. Geoelectrical methods for monitoring geological CO<sub>2</sub> storage: First results from cross-hole and surface-downhole measurements from the CO<sub>2</sub>SINK test site at Ketzin (Germany). *International Journal of Greenhouse Gas Control* 4, 816–826.
- Kopp, A., Probst, P., Class, H., Hurter, S., Helmig, R., 2009. Estimation of CO<sub>2</sub> storage capacity coefficients in geologic formations. *Energy Procedia* 1 (1), 2863–2870.
- Kühn, M., 2011. CO<sub>2</sub>-Speicherung. Chancen und Risiken. *Chemie in unserer Zeit* 45 (2), 126–138.
- Kummerow, J., Spangenberg, E., 2011. Experimental evaluation of the impact of the interactions of CO<sub>2</sub>-SO<sub>2</sub>, brine, and reservoir rock on petrophysical properties: A case study from the Ketzin test site, Germany. *Geochemistry Geophysics Geosystems* 12 (5).
- Labitzke, T., B. P. K. D. S.-H. C., 2012. 3D surface-downhole electrical resistivity tomography data sets of the Ketzin CO<sub>2</sub> storage pilot from the CO<sub>2</sub>SINK project phase. Scientific Technical Report: Data 12/05, NUR ONLINE ERSCHIENEN.
- Lazaratos, S. K., 1993. Analysis of the VSP-CDP mapping algorithm. *Stanford Wave Physics Lab STP Annual Reports* 4 (1), Paper I.

- Lengler, U., 2012. Einfluss von heterogenen Permeabilitätsfeldern auf die CO<sub>2</sub>-Speicherung in salinen Aquiferen am Beispiel vom Pilotstandort Ketzin. Dissertation. Ph.D. thesis, Technische Universität Hamburg-Harburg.
- Lengler, U., Lucia, M. D., Kühn, M., 2010. The impact of heterogeneity on the distribution of CO<sub>2</sub>: Numerical simulation of CO<sub>2</sub> storage at Ketzin. *International Journal of Greenhouse Gas Control* 4, 1016–1025.
- Liebscher, A., Martens, S., Möller, F., Kühn, M., 2012a. Geoscience of carbon dioxide (CO<sub>2</sub>) storage. J. Gluyas and S. Mathias (eds.) Woodhead Publishing Limited, Ch. On-shore CO<sub>2</sub> storage in Germany - experiences gained from the Ketzin pilot site, Brandenburg, the sole German national CO<sub>2</sub> storage project.
- Liebscher, A., Martens, S., Möller, F., Lüth, S., Schmidt-Hattenberger, C., Kempka, T., Szizybalski, A., Kühn, M., 2012b. Überwachung und Modellierung der geologischen CO<sub>2</sub>-Speicherung - Erfahrungen vom Pilotstandort Ketzin, Brandenburg (Deutschland). *Geotechnik* 35, 177–186.
- Liu, Y., Dong, L., Wang, Y., Zhu, J., Ma, Z., 2009. Sensitivity kernels for seismic Fresnel volume tomography. *Geophysics* 74 (5), U35–U46.
- Lüth, S., Bergmann, P., Cosma, C., Enescu, N., Giese, R., Götz, J., Ivanova, A., Juhlin, C., Kashubin, A., Yang, C., Zhang, F., 2011. Time-lapse seismic surface and down-hole measurements for monitoring CO<sub>2</sub> storage in the CO<sub>2</sub>SINK project (Ketzin, Germany). *Energy Procedia* 4, 3435–3442.
- Lüth, S., Buske, S., Giese, R., Goertz, A., 2005. Fresnel volume migration of multicomponent data. *Geophysics* 70 (6), S121–S129.
- Martens, S., Kempka, T., Liebscher, A., Lüth, S., Möller, F., 2012. Europe's longest-operating on-shore CO<sub>2</sub> storage site at Ketzin, Germany: a progress report after three years of injection. *Environmental Earth Sciences*, Online First<sup>TM</sup>.
- Martens, S., Liebscher, A., Möller, F., Würdemann, H., Schilling, F., Kühn, M., 2011. Progress report on the first European on-shore CO<sub>2</sub> storage site at Ketzin (Germany) – Second year of injection. *Energy Procedia* 4, 3246–3253.
- Möller, F., Liebscher, A., Martens, S., Schmidt-Hattenberger, C., Kühn, M., 2012. Yearly operational datasets of the CO<sub>2</sub> storage pilot site Ketzin, Germany. Scientific Technical Report: Data 12/06, NUR ONLINE ERSCHIENEN.
- Moret, G., Knoll, M., Barrash, W., Clement, W., 2006. Investigating the stratigraphy of an alluvial aquifer using crosswell seismic travelttime tomography. *Geophysics* 71 (3), B63–B73.
- Morozova, D., Wandrey, M., Alawi, M., Zimmer, M., Vieth, A., Zettlitzer, M., Würdemann, H., 2010. Monitoring of the microbial community composition in saline aquifers during CO<sub>2</sub> storage by fluorescence in situ hybridisation. *International Journal of Greenhouse Gas Control* 4 (6), 981–989.
- Morozova, D., Zettlitzer, M., Leta, D., Würdemann, H., CO<sub>2</sub>SINK-Group, 2011. Monitoring of the microbial community composition in deep subsurface saline aquifers during CO<sub>2</sub> storage in Ketzin, Germany. *Energy Procedia* 4, 4362–4370.
- Muller, N., Qi, R., Mackie, E., Pruess, K., Blunt, M., 2009. CO<sub>2</sub> injection impairment due to halite precipitation. *Energy Procedia* 1 (1), 3507–3514.
- Musil, M., Maurer, H., Green, A., 2003. Discrete tomography and joint inversion for loosely connected or unconnected physical properties: application to crosshole seismic and georadar data sets. *Geophys. J. Int.* 153, 389–402.
- Mutschler, T., Triantafyllidis, T., Balthasar, K., 2009. Geotechnical Investigations of Cap Rocks above CO<sub>2</sub>-Reservoirs. *Energy Procedia* 1, 3375–3382.

- Myrntinen, A., Becker, V., van Geldern, R., Würdemann, H., Morozova, D., Zimmer, M., Taubald, H., Blum, P., Barth, J., 2010. Carbon and oxygen isotope indications for CO<sub>2</sub> behaviour after injection: First results from the Ketzin site (Germany). *International Journal of Greenhouse Gas Control* 4, 1000–1006.
- Norden, B., 2007. Geologische Abschlussberichte der Bohrungen CO<sub>2</sub> Ktzi 200/2007, CO<sub>2</sub> Ktzi 201/2007 und CO<sub>2</sub> Ktzi 202/2007. Tech. rep., Helmholtz-Zentrum Potsdam, Deutsches GeoForschungsZentrum GFZ.
- Norden, B., 2011. Modelling of the near-surface groundwater flow system at the CO<sub>2</sub>SINK site Ketzin, Germany. *Z. dt. Ges. Geowiss.* 162/1, 63–77.
- Norden, B., Förster, A., Vu-Hoang, D., Marcelis, F., Springer, N., Nir, I. L., 2010. Lithological and Petrophysical Core-Log Interpretation in CO<sub>2</sub>SINK, the European CO<sub>2</sub> Onshore Research Storage and Verification Project. *SPE Res Eval & Eng* 13 (2), 179–192.
- Ouellet, A., Bérard, T., Desroches, J., Frykman, P., Welsh, P., Minton, J., Pamukcu, Y., Hurter, S., Schmidt-Hattenberger, C., 2011. Reservoir geomechanics for assessing containment in CO<sub>2</sub> storage: a case study at Ketzin, Germany. *Energy Procedia* 4, 3298–3305.
- Paige, C., Saunders, M., 1982. LSQR: An algorithm for sparse linear equations and sparse least squares. *ACM Transactions on Mathematical Software* 8 (1), 43–71.
- Pamukcu, Y., Hurter, S., 2009. Simulations of Breakthrough Time for CO<sub>2</sub> Injection at Ketzin. *Geophysical Research Abstracts*, EGU General Assembly 11, EGU2009–9637.
- Park, C., Miller, R., Steeples, D., Black, R., 1996. Swept impact seismic technique (SIST). *Geophysics* 61 (6), 1789–1803.
- Prevedel, B., Wohlgemuth, L., Henniges, J., Krüger, K., Norden, B., Förster, A., CO<sub>2</sub>SINK-Drilling-Group, 2008. The CO<sub>2</sub>SINK Boreholes for Geological Storage Testing. *Scientific Drilling* 6, 32–37.
- Prevedel, B., Wohlgemuth, L., Legarth, B., Henniges, J., Schütt, H., Schmidt-Hattenberger, C., Norden, B., Förster, A., Hurter, S., 2009. The CO<sub>2</sub>SINK boreholes for geological CO<sub>2</sub>-storage testing. *Energy Procedia* 1, 2087–2094.
- Rempel, K., Liebscher, A., Heinrich, W., Schettler, G., 2011. An experimental investigation of trace element dissolution in carbon dioxide: Applications to the geological storage of CO<sub>2</sub>. *Chemical Geology* 289 (3-4), 224–234.
- Rinke, M., 2007. Bohrtechnische Abschlussberichte zur Erstellung der Bohrungen Ketzin 200 (Ktzi 200), Ketzin 201 (Ktzi 201) und Ketzin 202 (Ktzi 202). Tech. rep., Geothermie Neubrandenburg GmbH.
- Sandmeier, K. J., 2004. *ReflexW Manual*.
- Schaack, M. A., 1996. XSP-CDP mapping in complex media without raytracing. *Stanford Wave Physics Lab STP Annual Reports* 7 (1), Paper O.
- Scherf, A.-K., Zetzl, C., Smirnova, I., Zettlitzer, M., Vieth-Hillebrand, A., 2011. Mobilisation of organic compounds from reservoir rocks through the injection of CO<sub>2</sub> - Comparison of baseline characterization and laboratory experiments. *Energy Procedia* 4, 4524–4531.
- Schilling, F., Borm, G., Würdemann, H., Möller, F., Kühn, M., CO<sub>2</sub>SINK-Group, 2009. Status Report on the First European on-shore CO<sub>2</sub> Storage Site at Ketzin (Germany). *Energy Procedia* 1, 2029–2035.
- Schmidt-Hattenberger, C., Bergmann, P., Kießling, D., Krüger, K., Rücker, C., Schütt, H., Ketzin-Group, 2011. Application of a Vertical Electrical Resistivity Array (VERA)

- for monitoring CO<sub>2</sub> migration at the Ketzin site: First performance evaluation. *Energy Procedia* 4, 3363–3370.
- Smith, L., 2002. A tutorial on Principal Components Analysis. Accessed 2011. [www.cs.otago.ac.nz](http://www.cs.otago.ac.nz).
- Spetzler, J., Snieder, R., 2004. Tutorial - The Fresnel volume and transmitted waves. *Geophysics* 69 (3), 653–663.
- Spetzler, J., Xue, Z., Saito, H., Nishizawa, O., 2008. Case story: time-lapse seismic crosswell monitoring of CO<sub>2</sub> injected in an onshore sandstone aquifer. *Geophys. J. Int.* 172, 21–225.
- Vibrometric, 2012. Borehole Receiver. Accessed 2012. [www.vibrometric.com](http://www.vibrometric.com).
- Vidale, J., May 1990. Finite-difference calculation of traveltimes in three dimensions. *Geophysics* 55 (5), 521–526.
- Wandrey, M., Fischer, S., Zemke, K., Liebscher, A., Scherf, A.-K., Vieth-Hillebrand, A., Zettlitzer, M., Würdemann, H., 2011a. Monitoring petrophysical, mineralogical, geochemical and microbiological effects of CO<sub>2</sub> exposure - Results of long-term experiments under in situ conditions. *Energy Procedia* 4, 3644–3650.
- Wandrey, M., Morozova, D., Zettlitzer, M., Würdemann, H., CO<sub>2</sub>SINK-Group, 2010. Assessing drilling mud and technical fluid contamination in rock core and brine samples intended for microbiological monitoring at the CO<sub>2</sub> storage site in Ketzin using fluorescent dye tracers. *International Journal of Greenhouse Gas Control* 4, 972–980.
- Wandrey, M., Pellizari, L., Zettlitzer, M., Würdemann, H., 2011b. Microbial community and inorganic fluid analysis during CO<sub>2</sub> storage within the frame of CO<sub>2</sub>SINK-Long-term experiments under in situ conditions. *Energy Procedia* 4, 3651–3657.
- Wiese, B., Böhner, J., Enachescu, C., Würdemann, H., Zimmermann, G., 2010a. Hydraulic characterisation of the Stuttgart formation at the pilot test site for CO<sub>2</sub> storage, Ketzin, Germany. *International Journal of Greenhouse Gas Control* 4, 960–971.
- Wiese, B., Nimtz, M., Klatt, M., Kühn, M., 2010b. Sensitivities of injection rates for single well CO<sub>2</sub> injection into saline aquifers. *Chemie der Erde* 70(S3), 165–172.
- Wikipedia, 2012a. Principal component analysis. Accessed 2012. <http://en.wikipedia.org>.
- Wikipedia, 2012b. Root-mean-square deviation. Accessed 2012. <http://en.wikipedia.org>.
- Würdemann, H., Möller, F., Kühn, M., Heidug, W., Christensen, N., Borm, G., Schilling, F., CO<sub>2</sub>SINK-Group, 2010. CO<sub>2</sub>SINK - From site characterisation and risk assessment to monitoring and verification: One year of operational experience with the field laboratory for CO<sub>2</sub> storage at Ketzin, Germany. *International Journal of Greenhouse Gas Control* 4, 938–951.
- Xu, Z., Juhlin, C., Gudmundsson, O., Zhang, F., Yang, C., Kashubin, A., Lüth, S., 2012. Reconstruction of subsurface structure from ambient seismic noise: an example from Ketzin, Germany. *Geophysical Journal International* 189 (2), 1085–1102.
- Yang, C., 2012. Time-lapse analysis of borehole and surface seismic data, and reservoir characterization of the Ketzin CO<sub>2</sub> storage site, Germany. Ph.D. thesis, Uppsala Universitet.
- Yang, C., Juhlin, C., Enescu, N., Cosma, C., Lüth, S., 2010. Moving source profile data processing, modelling and comparison with 3D surface seismic data at the CO<sub>2</sub>SINK project site, Ketzin, Germany. *Near Surface Geophysics* 8, 601–610.
- Yilmaz, O., 2000. *Seismic Data Analysis: Processing, Inversion, and Interpretation of Seismic Data*. Society Exploration Geophysicists.

- Yordkayhun, S., Ivanova, A., Giese, R., Juhlin, C., Cosma, C., 2009a. Comparison of surface seismic sources at the CO<sub>2</sub>SINK site, Ketzin, Germany. *Geophysical Prospecting* 57 (1), 125–139.
- Yordkayhun, S., Juhlin, C., Giese, R., Cosma, C., 2007. Shallow velocity-depth model using first arrival traveltimes inversion at the CO<sub>2</sub>SINK site, Ketzin, Germany. *Journal of Applied Geophysics* 63, 68–79.
- Yordkayhun, S., Juhlin, C., Norden, B., 2009b. 3D seismic reflection surveying at the CO<sub>2</sub>SINK project site, Ketzin, Germany: a study for extracting shallow subsurface information. *Near Surface Geophysics* 7 (2), 75–91.
- Yordkayhun, S., Tryggvason, A., Norden, B., Juhlin, C., Bergman, B., 2009c. 3D seismic traveltimes tomography imaging of the shallow subsurface at the CO<sub>2</sub>SINK project site, Ketzin, Germany. *Geophysics* 74 (1), G1–G15.
- Zelt, C., 1998. FAST – Program package for First Arrival Seismic Tomography. Manual. Rice University, Houston, USA.
- Zelt, C., 2012. FAST. Accessed 2012. <http://terra.rice.edu/departments/faculty/zelt/fast.html>.
- Zelt, C., Azaria, A., Levander, A., 2006. 3D seismic refraction traveltimes tomography at a groundwater contamination site. *Geophysics* 71 (5), H67–H78.
- Zelt, C., Barton, P., 1998. Three-dimensional seismic refraction tomography: A comparison of two methods applied to data from the Faeroe Basin. *Journal of Geophysical Research* 103 (B4), 7187–7210.
- Zemke, K., Liebscher, A., Wandrey, M., CO<sub>2</sub>SINK-Group, 2010. Petrophysical analysis to investigate the effects of carbon dioxide storage in a subsurface saline aquifer at Ketzin, Germany (CO<sub>2</sub>SINK). *International Journal of Greenhouse Gas Control* 4, 990–999.
- Zerbe, U., 2007. Bericht zu den geophysikalischen Bohrlochmessungen. Tech. rep., BLM Gommern.
- Zettlitzer, M., Möller, F., Morozova, D., Lokay, P., Würdemann, H., CO<sub>2</sub>SINK-Group, 2010. Re-establishment of the proper injectivity of the CO<sub>2</sub>-injection well Ktzi 201 in Ketzin, Germany. *International Journal of Greenhouse Gas Control* 4, 952–959.
- Zhang, F., Juhlin, C., Cosma, C., Tryggvason, A., Pratt, R., 2012. Cross-well seismic waveform tomography for monitoring CO<sub>2</sub> injection: a case study from the Ketzin Site, Germany. *Geophysical Journal International* 189 (1), 629–646.
- Zimmer, M., Erzinger, J., Kujawa, C., CO<sub>2</sub>SINK-Group, 2009. In-situ Down Hole Gas Measurements During Geological Storage of CO<sub>2</sub> at Ketzin, Germany. *Geophysical Research Abstracts*, EGU General Assembly 11, EGU2009–5003.
- Zimmer, M., Erzinger, J., Kujawa, C., CO<sub>2</sub>SINK-Group, 2011a. The gas membrane sensor (GMS): A new method for gas measurements in deep boreholes applied at the CO<sub>2</sub>SINK site. *International Journal of Greenhouse Gas Control* 5 (4), 995–1001.
- Zimmer, M., Pilz, P., Erzinger, J., 2011b. Long-term surface carbon dioxide flux monitoring at the Ketzin carbon dioxide storage test site. *Environmental Geosciences* 18 (2), 119–130.



# **A** **Appendix A**

---

## **Offset VSP: comparison of Kirchhoff and Fresnel migration**

The Figures A.1 and A.2 show the results of Kirchhoff (left column) and Fresnel migration (right column) of the source points 1, 2, 5 and 6 (Fig. 6.1). The data of baseline, repeat and difference are presented from top to bottom. The inset explains the geometry of the images. For comparison the 3D surface seismic baseline, repeat and difference is inserted in the background. The data sets are normalised to the centre peak of the K2 reflector.

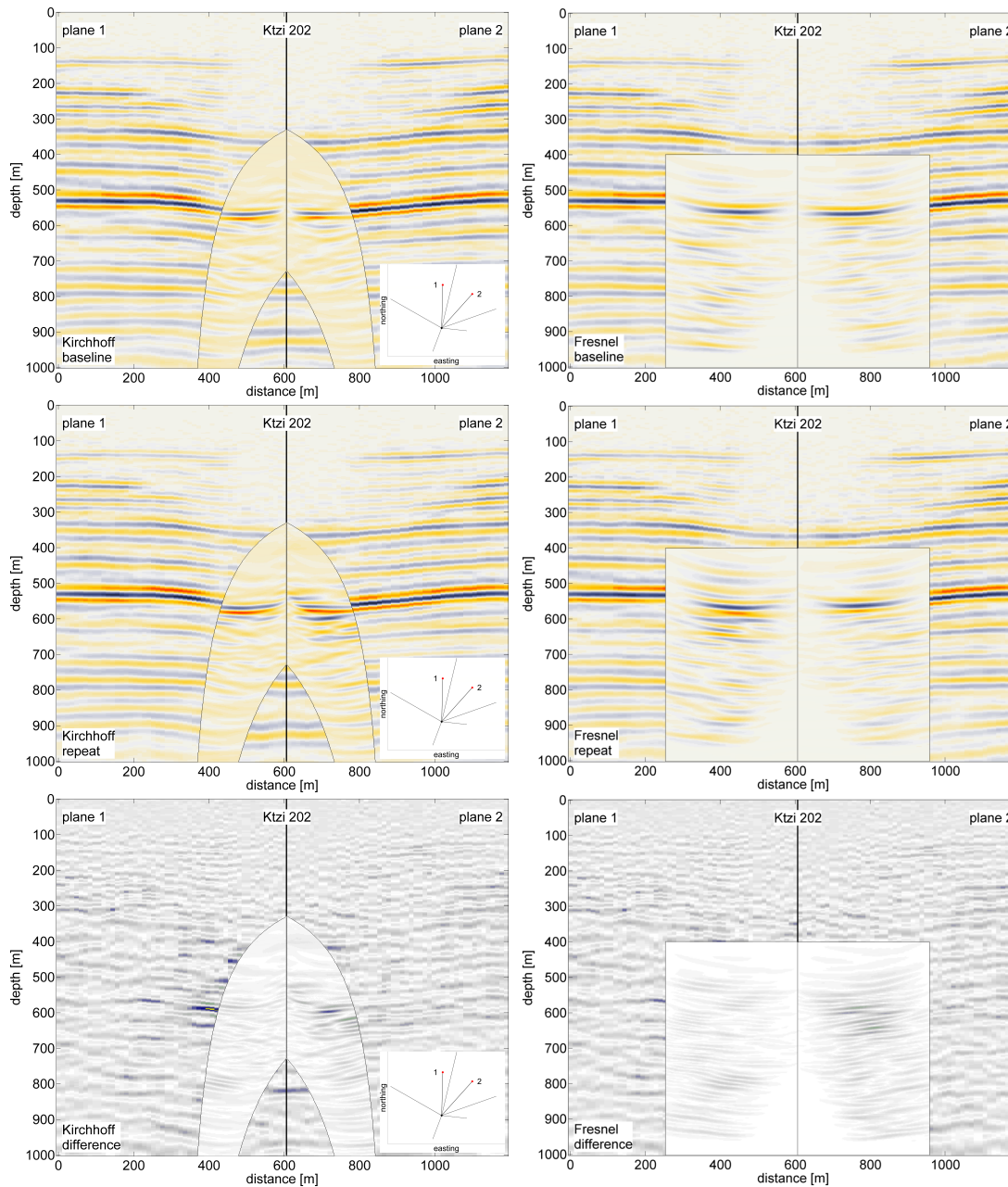


Figure A.1: Results of Kirchhoff (left column) and Fresnel migration (right column) of source points 1 and 2 (Fig. 6.1). The data of baseline, repeat and difference are presented from top to bottom. The inset explains the geometry of the images: the imaging planes of source point 1 and 2 are unfold at the Ktzi 202 well and the migration results are presented side by side. For comparison the 3D surface seismic baseline, repeat and difference is inserted in the background. The locations of source points 1 and 2 are at 0 m depth, 0 m and 1200 m distance, respectively. The data sets are normalised to the centre peak of the K2 reflector.

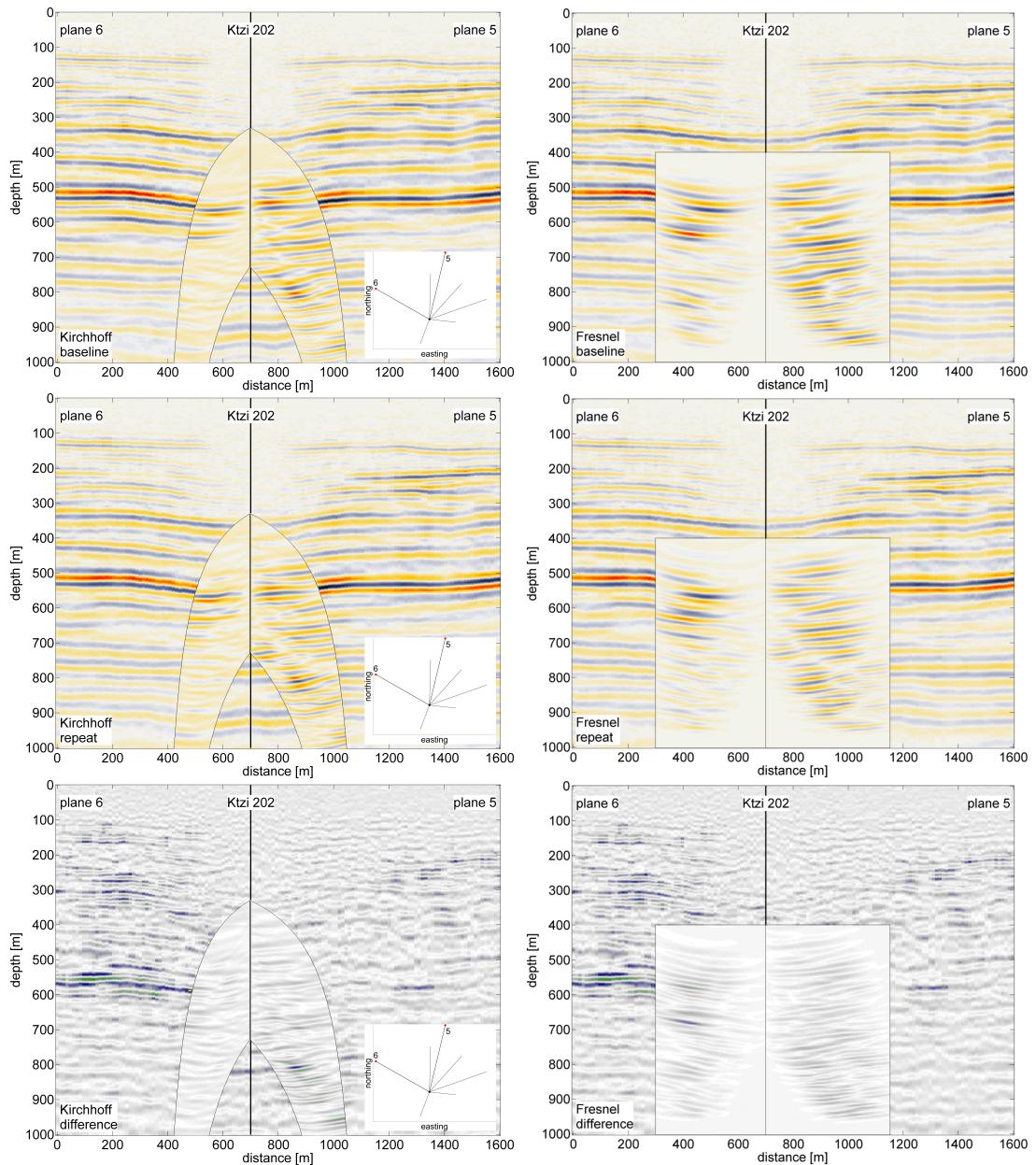


Figure A.2: Results of Kirchhoff (left column) and Fresnel migration (right column) of source points 6 and 5 (Fig. 6.1). The data of baseline, repeat and difference are presented from top to bottom. The inset explains the geometry of the images: the imaging planes of source point 6 and 5 are unfold at the Ktzi 202 well and the migration results are presented side by side. For comparison the 3D surface seismic baseline, repeat and difference is inserted in the background. The locations of source points 6 and 5 are at 0 m depth, 0 m and 1600 m distance, respectively. The data sets are normalised to the centre peak of the K2 reflector.

## **STATEMENT OF ORIGINAL AUTHORSHIP**

I, Julia Götz, hereby declare that the work contained in this thesis has not previously been submitted for assessment, either in whole or in part, by either me or any other person at either the Fakultät VI - Planen, Bauen, Umwelt der Technischen Universität Berlin or at any other institution.

To the best of my knowledge and belief, the thesis contains no material which has been previously published or written by another person except where due reference is made.

Julia Götz

Potsdam, den 08. Juli 2013

Hiermit erkläre ich, Julia Götz, dass diese Arbeit von mir bisher weder an der Fakultät VI - Planen, Bauen, Umwelt der Technischen Universität Berlin noch an einer anderen wissenschaftlichen Einrichtung zum Zwecke der Promotion eingereicht wurde.

Ferner erkläre ich, dass ich diese Arbeit selbstständig verfasst und keine anderen als die darin angegebenen Quellen und Hilfsmittel benutzt habe.

Julia Götz

Potsdam, den 08. Juli 2013